การเตรียม $La_{2-x}Ca_xNi_{1-y}Co_y(Ga, Ti)_zO_4$ สำหรับเซลล์เชื้อเพลิงออกไซด์ของแข็ง

นางสาว ชนินาถ ราชอุ่น

วิทยานิพนธ์นี้เป็นส่วนหนึ่งของการศึกษาตามหลักสูตรปริญญาวิทยาศาสตรมหาบัณฑิต
สาขาวิชาปิโตรเคมี และวิทยาศาสตร์พอลิเมอร์
คณะวิทยาศาสตร์ จุฬาลงกรณ์มหาวิทยาลัย
ปีการศึกษา 2553
ลิขสิทธิ์ของจุฬาลงกรณ์มหาวิทยาลัย

PREPARATION OF $La_{2-x}Ca_xNi_{1-y}Co_y(Ga, Ti)_zO_4$ FOR SOLID OXIDE FUEL CELL

Miss Chaninart Ratchaoun

A Thesis Submitted in Partial Fulfillment of the Requirements
for the Degree of Master of Science Program in Petrochemistry and Polymer Science
Faculty of Science
Chulalongkorn University
Academic Year 2010
Copyright of Chulalongkorn University

Thesis Title	PREPARATION OF $La_{2-x}Ca_xNi_{1-y}Co_y(Ga,Ti)_zO_4$ FOR SOLID OXIDE FUEL CELL
By	Miss Chaninart Ratchaoun
Field of Study	Petrochemistry and Polymer Science
Thesis Advisor	Assistant Professor Soamwadee Chaianansutcharit, Ph.D.

Accepted by the Faculty of Science, Chulalongkorn University in Partial Fulfillment of the Requirements for the Master's Degree

……Dean of the Faculty of Science
(Professor Supot Hannongbua, Dr.rer.nat)

THESIS COMMITTEE

……Chairman
(Professor Pattarapan Prasassarakich, Ph.D.)

……Thesis Advisor
(Assistant Professor Soamwadee Chaianansutcharit, Ph.D.)

……Examiner
(Associate Professor Wimonrat Trakarnpruk, Ph.D.)

……External Examiner
(Siriporn Larpkiattaworn, Ph.D.)

ชนินาถ ราชอุ่น : การเตรียม $La_{2-x}Ca_xNi_{1-y}Co_y(Ga, Ti)_zO_4$ สำหรับเซลล์เชื้อเพลิงออกไซด์ของแข็ง. (PREPARATION OF $La_{2-x}Ca_xNi_{1-y}Co_y(Ga, Ti)_zO_4$ FOR SOLID OXIDE FUEL CELL) อ. ที่ปรึกษาวิทยานิพนธ์หลัก : ผศ.ดร. โสมวดี ไชยอนันต์สุจริต, 96 หน้า.

ศึกษาสมบัติของวัสดุสำหรับใช้เป็นขั้วแคโทดในเซลล์เชื้อเพลิงออกไซด์ของแข็ง $La_{2-x}Ca_xNi_{1-y}Co_y(Ga, Ti)_zO_{4+\delta}$ (x = 0.0-1.0, y = 0.1-0.2, z = 0.00-0.1,0.2) สามารถเตรียมโครงสร้างแบบ K_2NiF_4 จากวิธีซิเตรตประยุกต์ได้ในสารประกอบ $La_2Ni_{1-y}Co_yO_{4+\delta}$, ที่มีสัดส่วน y = 0.1-0.2 โดยทำการเผาและซินเตอร์ที่อุณหภูมิ 1200 และ 1300 องศาเซลเซียส ตามลำดับ เป็นเวลา 6 ชั่วโมง $La_2Ni_{0.9}Co_{0.1}O_{4+\delta}$ ให้อัตราการซึมผ่านของออกซิเจนสูงที่สุด ที่ 0.78 ไมโครโมลต่อวินาทีต่อตารางเซนติเมตร ที่อุณหภูมิ 1000 องศาเซลเซียส โดยค่าการนำไฟฟ้าของ $La_2Ni_{0.9}Co_{0.1}O_{4+\delta}$ จะเพิ่มขึ้นเมื่อแทนที่แคลเซียมไอออน ในตำแหน่งของแลนทานัม ในสารประกอบ $La_{2-x}Ca_xNi_{0.9}Co_{0.1}O_{4+\delta}$ ที่มีสัดส่วน x = 0.0-1.0 อย่างไรก็ตาม พบว่าเฉพาะสัดส่วนที่ x = 0.5 เท่านั้น ที่พบโครงสร้าง K_2NiF_4 บริสุทธิ์ โดยค่าการนำไฟฟ้าสูงสุดของ $La_{1.5}Ca_{0.5}Ni_{0.9}Co_{0.1}O_{4+\delta}$ เท่ากับ 106.3 ซีเมนส์ต่อเซนติเมตร ที่ 800 องศาเซลเซียส และอัตราการซึมผ่านของออกซิเจน 0.48 ไมโครโมลต่อวินาทีต่อตารางเซนติเมตร ที่อุณหภูมิ 1000 องศาเซลเซียส เช่นเดียวกันเมื่อทำการเพิ่มแกลเลียมและไททาเนียมไอออน ในสารประกอบ $La_{1.5}Ca_{0.5}Ni_{0.9}Co_{0.1}(Ga, Ti)_zO_{4+\delta}$ ที่สัดส่วน z = 0.00-0.1,0.2 พบว่า ในสารประกอบที่เพิ่มแกลเลียมไอออน ทุกส่วนประกอบแสดงโครงสร้าง K_2NiF_4 บริสุทธิ์ โดยสารประกอบที่สัดส่วน z = 0.01 ให้อัตราการซึมผ่านของออกซิเจนสูงที่สุด 0.49 ไมโครโมลต่อวินาทีต่อตารางเซนติเมตร ณ อุณหภูมิ 1000 องศาเซลเซียส แต่ค่าการนำไฟฟ้าจะลดลงเป็น 60.12 ซีเมนส์ต่อเซนติเมตร ที่อุณหภูมิ 800 องศาเซลเซียส นอกจากนั้นในสารประกอบที่เพิ่มไททาเนียมไอออนที่สัดส่วน z = 0.01-0.05 แสดงโครงสร้าง K_2NiF_4 บริสุทธิ์ ซึ่งอัตราการซึมผ่านของออกซิเจนและค่าการนำไฟฟ้าของสารประกอบมีแนวโน้มลดลงเมื่อปริมาณของไททาเนียมไอออนเพิ่มขึ้น

สาขาวิชา ปิโตรเคมีและวิทยาศาสตร์พอลิเมอร์ ลายมือชื่อนิสิต .....

ปีการศึกษา 2553 ลายมือชื่อ อ.ที่ปรึกษาวิทยานิพนธ์หลัก .....

5172256723 : MAJOR PETROCHEMISTRY AND POLYMER SCIENCE
KEYWORDS : K_2NiF_4 STRUCTURE/ ELECTRICAL CONDUCTIVITY / THERMAL EXPANTION COEFFICIENT / OXYGEN PERMEATION

CHANINART RATCHAOUN : PREPARATION OF $La_{2-x}Ca_xNi_{1-y}Co_y(Ga, Ti)_zO_4$ FOR SOLID OXIDE FUEL CELL. THESIS ADVISOR : ASST. PROF. SOAMWADEE CHAIANANSUTCHARIT, Ph.D., 96 pp.

The properties of $La_{2-x}Ca_xNi_{1-y}Co_y(Ga, Ti)_zO_{4+\delta}$ (x = 0.0-1.0, y = 0.1-0.2, z = 0.00-0.1, 0.2) cathode materials for solid oxide fuel cell were studied. It was found that the K_2NiF_4-type perovskite structure synthesized by the modified citrate method was obtained from $La_2Ni_{1-y}Co_yO_{4+\delta}$ (y = 0.1-0.2) calcined and sintered at 1200ºC and 1300ºC, respectively, for 6 hrs. The highest oxygen permeation rate was obtained from the $La_2Ni_{0.9}Co_{0.1}O_{4+\delta}$ for 0.78 µmol/s.cm^2 at 1000ºC. The electrical conductivity of $La_2Ni_{0.9}Co_{0.1}O_{4+\delta}$ increased with the doping of Ca^{2+} ion in La^{3+} site for $La_{2-x}Ca_xNi_{0.9}Co_{0.1}O_{4+\delta}$ (x = 0.0-1.0). However, the single phase of K_2NiF_4-type structure was only achieved when x = 0.5. The electrical conductivity of the $La_{1.5}Ca_{0.5}Ni_{0.9}Co_{0.1}O_{4+\delta}$ reached the maximum value of 106.3 S/cm at 800ºC and the oxygen permeation rate was 0.48 µmol/s.cm^2 at 1000ºC. The addition of $Ga^{3+}$and Ti^{4+} ions on $La_{1.5}Ca_{0.5}Ni_{0.9}Co_{0.1}(Ga, Ti)_zO_{4+\delta}$ (z = 0.00-0.1, 0.2) was investigated. For Ga^{3+} ion addition, all of compositions showed the single phase of K_2NiF_4-type structure. The highest oxygen permeation rate was obtained for 0.49 µmol/s.cm^2 at 1000ºC on Ga^{3+} ion doping of z = 0.01, while the electrical conductivity was decreased to 60.12 S/cm at 800ºC. Additionally, the addition of Ti^{4+} ion with z = 0.01-0.05 showed the single phase of K_2NiF_4-type structure. The oxygen permeation rate and the electrical conductivity were tentatively decreased with an increase of Ti^{4+} ion.

Field of Study : Petrochemistry and Polymer Science Student's Signature .....
Academic Year : 2010 Advisor's Signature .....

ACKNOWLEDGEMENTS

The success of this thesis can be attributed to the extensive support and assistance from Assistant Professor Dr. Soamwadee Chaianunsutcharit, author's advisor. The author deeply thanks for her valuable advice and guidance in this research and her kindness throughout this study.

The author would like to gratitude to Professor Dr. Pattarapan Prasassarakich, Associate Professor Dr. Wimorat Trakarnpruk and Dr. Siriporn Larpkiattaworn as the chairman and members of this thesis committee, respectively, for all of their kindness and useful advice in the research. And, also Dr. Thanakorn Wasanapiarnpong in Department of Material Science, Faculty of Science, Chulalongkorn University for his kindness on Thermal expansion coefficient (TEC) analyses.

The author would like to gratefully thank Office National Research Council of Thailand (NRCT) for financial support. Moreover, National Center of Excellence for Petroleum, Petrochemicals, and Advanced Materials, Chulalongkorn University and Program of Petrochemistry and Polymer Science, and Graduate School are also appreciated for the valuable knowledge, experience and their partially financial supports. Furthermore, she would like to thank the members of Materials Chemistry and Catalysis Research Unit for generosity, especially their very good corporation in work, sharing of colorful emotion and friendly working atmosphere.

Finally, she would like to express her deepest gratitude to her beloved family for their entirely care and support. The usefulness of this thesis, she dedicate to her family and all teachers who have taught me since my childhood.

CONTENTS

Page

Page

Page

LIST OF TABLES

Table **Page**

LIST OF FIGURES

Figure **Page**

Figure **Page**

LIST OF ABBREVIATIONS

SOFCs	Solid Oxide Fuel Cell
DMFC	Direct Methanol Fuel Cell
PEMFC	Proton Exchange Membrane Fuel Cell
AFC	Alkaline Fuel Cell
PAFC	Phosphoric Acid Fuel Cell
MCFC	Molten Carbonate Fuel Cell
MIEC	Mixed Ionic Electronic Conductor
TEC	Thermal Expansion Coefficients
XRD	X-ray diffractrometry
SEM	Scanning Electron Microscopy
Jo_2	Oxygen permeation rate
^oC	degree Celsius
K	Kelvin
ml	milliliter
hrs	hour
min	minute
g	gram
mg	milligram
mm	millimeter
cm	centimeter
µm	micrometer
nm	nanometer
a, c	unit lattice parameter
Å	Angstrom
%	percent
r	Ionic radius
t	tolerance factor
σ	Specific conductivity
δ	oxygen non – stoichiometry
L	length

I	current
T	thickness
V	voltage
W	width
ρ	Specific resistance
Ω	Ohm

CHAPTER I

INTRODUCTION

1.1 Background

Fuel cell is developed as an intermediate-term power source for atmospheric applications. A fuel cell is similar to a battery in that it converts the chemical energy of a fuel directly into D.C. electricity. However, unlike a battery, it does not down in energy and have to be recharged. It keeps producing electricity as long as the fuel is supplied. The fuel cell can be called “the gas battery”. A typical fuel gas is hydrogen or a hydrogen mixture and an oxidant.

A fuel cell also finds applications as an auxiliary power source for orbit transfer vehicles in space lasting for a few days to a few weeks. The regenerative fuel cell integrated with an electrolyzer unit presents an attractive mass saving for large energy storage. In the fuel cell, hydrogen and oxygen are combined to produce electricity and water. The energy conversion is direct from chemical to electrical. It skips the usual combustion step of conventional power systems and converts a high percentage of the fuel’s available free chemical energy directly into electricity. The fuel cell efficiency, therefore, can be about twice that of the thermodynamic converter. It is as high as 75-80% in solid metal oxide fuel cells developed for ground base power plants. Its superior reliability is an additional benefit over thermodynamic power generators [1]. Indeed, the advantages of solid oxide fuel cell (SOFC) are as consequence of; (i) the high operating temperature (600–900ºC), allowing the use of non-precious metal electrocatalysts, heat recovery and the superior ionic conductivity of the different components; (ii) the fact that the cell consists of assembled solid ceramic components; (iii) high energy conversion efficiency; (iv) no emission of pollutant by CO; (v) high stability; and (vi) flexibility in fuel [2]. The cathode materials of SOFCs should have high-electronic and ionic conductivity, thermal and chemical compatibilities with the electrolyte. The development of new material in oxygen permeation, thermal compatibilities and long term stability is also important

for applications [3]. Therefore, the interest is currently being expressed in mixed electronic and ionic conductors (MIECs) of oxide materials, such as perovskite (ABO_3) and K_2NiF_4-type structure (A_2BO_4) with high conductivities [4].

1.2 Literature reviews

Perovskite and related oxides have been extensively studied for solid oxide fuel cell (SOFC). The perovskite-type oxides such as perovskite (ABO_3) and K_2NiF_4 (A_2BO_4) are of interest materials for using SOFC cathodes. A_2BO_4 oxide with the K_2NiF_4-type structure, represented by a combination of the ABO_3 perovskite and the AO rock-salt layers which are arranged one upon the other, have better performance in thermochemical stability, oxygen permeation flux and thermal expansion compared with the ABO_3-type structure. In addition, recent studies on mixed conductors [3] indicated that the K_2NiF_4-typed structure have promising properties at intermediate operation temperatures due to their high ionic conduction and their high electricatalytic activity.

In 2000, Ishihara *et al*. [5] studied properties of Fe-, Co-, Ni-doped $LaGaO_3$ oxides by a conventional solid state reaction technique. These $LaGaO_3$ oxides exhibited low electronic conductivity but high oxide ion conductivity. However, the electrical conductivity strongly depended on the type of dopant in the Ga site of $LaGaO_3$. It was evident that the electrical conductivity was increased by the dopant in the following order, Co>Ni>Fe. Co dopant for a $LaGaO_3$-based oxide gave the highest electrical conductivity whereas the Ni-doped sample gave the highest oxygen permeation rate. Therefore, Co- and Ni-doped $LaGaO_3$-based oxides seem to have a mixed electronic hole and be an oxide-ionic conductor.

In 2003, Daroukh *et al.* [6] reported that the thermochemical stability of A_2BO_4 oxides ($A_{2-x}A'_xBO_4$, A = La, A' = Sr, B = Mn, Fe, Co, Ni) was higher than that of the perovskite ABO_3 oxides, and the thermal expansion of A_2BO_4 oxides was generally lower than that of the ABO_3 oxides with comparable cationic compositions. This implies that A_2BO_4 oxides are very likely to be new type of cathode materials for IT-SOFCs [7].

In 2003, Mori *et al*. [8] studied thermal and electrical conductivity of $La_{0.6}AE_{0.4}MnO_3$ perovskite (AE = Ca, Sr). The thermal expansion coefficient (TEC)

of $La_{0.6}Ca_{0.4}MnO_3$ was lower than that of $La_{0.6}Sr_{0.4}MnO_3$ in the temperature range from 50-1000ºC. Electrical conductivity of the dense membranes of $La_{0.6}Ca_{0.4}MnO_3$ was higher than that of $La_{0.6}Sr_{0.4}MnO_3$ at 1000ºC. $La_{0.6}Ca_{0.4}MnO_3$ showed electrochemical compatibility with the YSZ electrolyte greater than the $La_{0.6}Sr_{0.4}MnO_3$ materials.

In 2006, Ding *et al*. [9] studied the effect of cation substitution on the sintering characteristics and thermal expansion properties of $La_{0.85}(AE)_{0.15}CrO_3$ (AE = Mg, Ca, Sr). It was found that the densities of sintered bodies increased with increased sintering temperatures. Ca-doped $LaCrO_3$ sample showed better sintering ability than Sr- and Mg-doped samples. The thermal expansion coefficiency achiever of Ca-doped, the strength of the interatomic bonds increases, which causes less thermal expansion.

In 2007, Burriel *et al*. [10] studied on the $Ln_2NiO_{4+\delta}$ family, where Ln = La, Pr, Nd, Sm and found that $La_2NiO_{4+\delta}$ is the parent of a new important family of mixed conductors for intermediate temperature application. It has relatively large oxygen permeation, low thermal expansion as well as the high chemical stability but low electrical conductivity.

In 2007, Qing Xu *et al.* [11] studied electrical conductivity and thermal expansion properties of $Ln_{0.6}Sr_{0.4}Co_{0.2}Fe_{0.8}O_3$ (Ln = La, Pr, Nd, Sm) perovskite ceramics prepared from a glycine-nitrate process. The electrical conductivity of sample in mixed conducting perovskite originates from the B-O-B electrical transport, highly depending on the overlap of the oxygen 2p orbitals with the transitional metal 3d orbitals. The decrease of average cationic radius of the A-site cations induces a titling and rotation of the BO_6 octahedra to accommodate the extra space around the A-site. This occurrence reduces the B-O-B bond angle, which is unfavorable for the orbital overlap and consequently the B-O-B electrical transport. The thermal expansion coefficient (TEC) can be explained in term of chemically induced lattice expansion due to oxygen loss and formation of oxygen vacancies. The average TEC values in low temperature of $Ln_{0.6}Sr_{0.4}Co_{0.2}Fe_{0.8}O_3$ ceramics tends to reduce with decreasing the size of the lanthanide cation, conversely TEC values in high temperature (600-1000°C) result in an increase in thermal expansion.

In 2007, Riza *et al*. [12] studied the influence of A-site and B-site doping on the properties of the $La_2CoO_{4+\delta}$ system. The $LaSrCo_{0.5}M_{0.5}O_{4+\delta}$ (M = Co, Fe, Mn, Ni) and $La_{1.4}Sr_{0.6}Co_{0.5}M_{0.5}O_{4+\delta}$ (M = Co, Ni) compounds were prepared and characterized in order to elucidate the influence of Sr-doping on A-site as well as the doping of transition metal on B-site of the mixed conductor $La_2CoO_{4+\delta}$. The decreasing content of Sr in A-site made the unit cell volume increased and Ni-doping on B-site metals reduced the volume of unit cell because the size of B-site cation affects the length of the B-O bond. Compounds containing minimal unit cell volume and short length of the B-O bond have low loss of oxygen in the lattice. Therefore, the electrical conductivity increases and thermal expansion coefficient decreases.

In 2007, Lee *et al.* [13] investigated the effect of M^{n+} cation doping on thermal expansion coefficient (TEC) and electrical conductivity of the $Nd_{0.6}Sr_{0.4}Co_{0.8}M_{0.2}O_{3-\delta}$ (M = Ti, Cr, Mn, Fe, Co and Cu). When increasing temperature, the oxygen loss form lattice result to an increase in the thermal stability and bond strength and decrease in the metal-oxygen (M-O) covalency. For Ti^{4+} ions are much stable at high temperatures. The replacement of Ti^{4+} ions leads to a decrease in TEC, because Ti^{4+} was investigate with the prevent of oxygen loss in lattice, implying that the M-O bond strength increases on Ti^{4+} and decreases in the transfer gap between the metal 3d orbital and oxygen 2p orbital bands leading to an increased electrical conductivity.

In 2008, Ishihara *et al*. [14] investigated the oxygen permeation by varying Ga concentrations. It was found that cation excess composition of $Pr_2Ni_{0.75}Cu_{0.25}Ga_{0.05}O_4$ achieved the highest oxygen permeation in air, but doping small amount of excess Ga decreased total conductivity in $Pr_2Ni_{0.75}Cu_{0.25}O_4$. Since the oxygen permeation rate was much improved by doping excess amount of Ga, the oxygen permeation in the material was controlled by oxide ion conductivity and electrical hole conductivity was much higher than that of the oxide ion conduction. In addition, the doping extra Ga may be introduced at the vacancy site of Ni in Pr_2NiO_4 or interstitial site. Doping excess Ga gave the large free volume in the rock-salt block in Pr_2NiO_4, the interstitial oxygen and excess cation may be introduced into the rock-salt block, which could be improved the high oxygen permeation rate in this Ga excess in Pr_2NiO_4.

In 2009, Zhang *et al*. [15] studied electrical conductivity of doped lanthanum manganese chromites based perovskite, $La_{0.7}A_{0.3}Cr_{0.5}Mn_{0.5}O_{3-\delta}$ (LACM, A = Ca, Sr,

Ba). The microstructure of LCM depended strongly on the A-site doping. The Ca-doped LCM (LCCM) gave the dense microstructure with few isolated pores and the bulk density higher than Ba- and Sr-doped in LCM. The highest electrical conductivity was obtained on LCCM. The much lower electrical conductivity of Ba- and Sr-doped LCM were most likely due to the formation of the secondary phase, poor microstructure and the lower density.

1.3 Objective of this study

The objectives of this study are as follows:

1. To synthesize $La_{2-x}Ca_xNi_{1-y}Co_y(Ga, Ti)_zO_{4+\delta}$ (x = 0.0-1.0, y = 0.0-0.9, z = 0.01-0.1, 0.2) with the K_2NiF_4-type structure.

2. To prepare dense membrane and characterize the structure by XRD and surface morphology by SEM.

3. To study properties of synthesized materials such as electrical conductivity, oxygen permeation and thermal expansion coefficient property.

1.4 The scope of this study

Firstly, $La_2Ni_{1-y}Co_yO_{4+\delta}$ (y = 0.1-0.9) were synthesized by modified citrate method. The samples were characterized for the K_2NiF_4-type structure by XRD and for surface morphology by SEM. The property of samples were investigated for electrical conductivity and thermal expansions coefficiency. The sample with the highest oxygen permeation is chosen for further study.

Secondly, Ca^{2+} ions is introduced in to the in A-site to obtain $La_{2-x}Ca_xNi_{1-y}Co_yO_{4+\delta}$ (x = 0.1-1.0, y = 0.1-0.2). The synthesized samples were characterized for the single phase K_2NiF_4-type structure by XRD and for surface morphology by SEM. The property of samples were investigated for oxygen permeation, thermal expansion coefficiency. The sample with the highest electrical conductivity is chosen for further study.

Lastly, Ga^{3+} and Ti^{4+} ion doped non-stoichiometry was introduced to obtain $La_{2-x}Ca_xNi_{1-y}Co_y(Ga, Ti)_zO_{4+\delta}$ (x = 0.5, y = 0.1 and z = 0.01-0.1, 0.2). The synthesized samples were characterized for single phase K_2NiF_4-type structure by XRD and for

surface morphology by SEM. The properties of samples were investigated for electrical conductivity, thermal expansion coefficiency.

CHAPTER II

THEORY

2.1 Fuel cells

A fuel cell is an energy conversion device that coverts the chemical energy of a fuel gas directly to electrical and heat, giving much higher conversion efficiencies than conventional thermomechanical methods. The operating principles of fuel cells are similar to those of batteries, i.e. electrochemical combination of reactants to generate electricity, a combination made of gaseous fuel (hydrogen) and an oxidant gas (oxygen from air) through electrodes and via an ion conducting electrolyte. A fuel cell operates as long as both fuel and oxidant are supplied to the electrodes and it also exerts on the surrounding environment.

2.1.1 Types of fuel cells

Fuel cells are generally classified by the chemical characteristics of the electrolyte used as the ionic conductor in the cell, as summarized in Table 2.1. The five types are catagorized by their operating temperature, their electrical generating efficiencies, and their abilities to utilize methane [16].

There are also other types of fuel cell which are less employed, but may later find a specific application. Examples are the air cells, sodium amalgam cells, biochemical fuel cells, inorganic cells, regenerative cells, alkali metal-halogen cells, etc.

Table 2.1. Types of fuel cells [17].

Type	Alkaline fuel cell (AFC)	Photon exchange membrane fuel cell (PEMFC)	Phosphoric acid fuel cell (PAFC)	Molten carbonate fuel cell (MCFC)	Solid oxide fuel cell (SOFC)
Electrolyte	potassium hydroxide	polymer	phosphoric acid	molten carbonate	oxide
Charge carrier	OH^-	H^+	H^+	CO_3^-	O^{2-}
Operating temp.(°C)	50-200	50-80	160 – 210	630 - 750	600-1000
Fuel	H_2	H_2, alcohol	H_2, alcohol	H_2, methanol	hydrocarbon, H_2, CO
Efficiency (%)	50-55	40-50	40-50	50- 60	50 - 60
Application	mobile space ship	mobile vehicle	stationary	stationary	stationary mobile

Present materials science has made the fuel cells a reality in some specialized applications. By far the greatest research interest throughout has focused on proton exchange membrane (PEM) and solid oxide fuel cell (SOFC) stacks. PEMs are well advanced type of fuel cell that are appropriated for cars and mass transportation. SOFC technology is the most interesting and is developed to high power generating station. The efficiency of SOFC is resulted from the flexibility of fuel such as carbon-based fuels, natural gas. The high operating temperature of SOFCs produces high quality heat by product which can be used for co-generation, or for use in combined cycle applications. Additionally SOFCs do not have problems with electrolyte management.

2.1.2 Solid oxide fuel cell

Solid oxide fuel cells (SOFC) have recently emerged as a serious high temperature fuel cell technology. They promise to be extremely useful in large, high-power applications such as full-scale industrial stations and large-scale electricity-generating stations. Some SOFCs are being used in motor vehicles. A SOFC system usually comprises of a solid ceramic as the electrolyte and operates at high temperatures (600-1000°C). This operating temperature allows internal reforming, promotes rapid electrocatalysis with non-precious metals, and produces high quality by product heat for co-generation. Efficiency of the cell can be increase up to 70% and providing 20% as heat recovery. SOFCs are best suited for provision of power in utility applications due to the significant time required to increase the operating temperatures.

During operating, hydrogen fuel is fed onto the anode of the fuel cell and oxygen from the air, enters the cell through the cathode. By burning fuel containing hydrogen on one side of the electrolyte, the concentration of oxygen is dramatically reduced. The electrode on this side will allow oxygen ions to leave the electrolyte and react with the fuel which is oxidised, thereby releasing electrons (e^-). On the other side of the plate exposed to air, an oxygen concentration gradient is created across the electrolyte, which attracts oxygen ions from the air side, or cathode, to the fuel side, or anode. If there is an electrical connection between the cathode and the anode, this allows electrons to flow from the anode to the cathode. Whereas a continuous supply of oxygen ions (O^{2-}) for the electrolyte is maintained, oxygen ions from the cathode to the anode maintain the overall electrical charge balance, thereby generating useful electrical power from the combustion of the fuel. The only byproduct of this process is a pure water (H_2O) and heat, as shown in Figure 2.1.

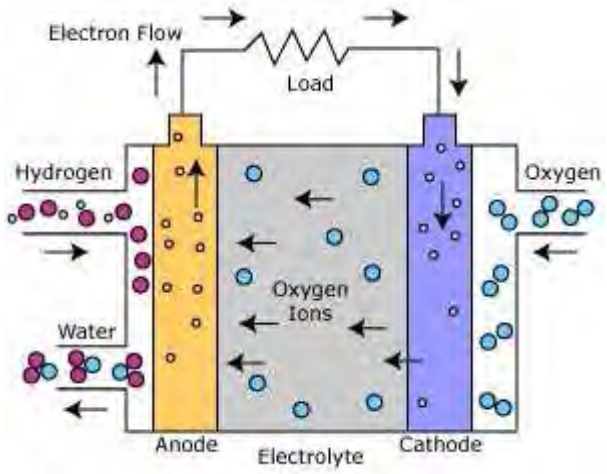

Figure 2.1 Schematic diagram showing the mechanism of a solid oxide fuel cell [18].

The SOFC reactions at each electrode are described as follows:

Anode reaction:	$2H_2 + 2O^{2-}$	=>	$2H_2O + 4e^-$	(2.1)
Cathode reaction:	$O_2 + 4e^-$	=>	$2O^{2-}$	(2.2)
Overall cell reaction:	$2H_2 + O_2$	=>	$2H_2O$	(2.3)

The efficiency in generating electricity is among the highest of the fuel cells at about 60%. Furthermore, the high operating temperature allows cogeneration applications to create high-pressure steam that can be used in many applications. Combining a high–temperature fuel cell with a turbine into a hybrid fuel cell further increases the overall efficiency of generating electricity with a potential of an efficiency of more than 70%.

2.1.3 Materials for SOFC

Once the molecular oxygen has been converted to oxygen ions, it must migrate through the electrolyte to the fuel side of the cell. For such migration, the electrolyte possesses high ionic conductivity and no electrical conductivity. The electrolyte must be fully dense to prevent short circuiting of gases through it. It should also be as thin as possible to minimize resistive loss in the cell. As with the other materials, it must be chemically, thermally and structurally stable across a wide

temperature range. For oxygen ion conductors, current flow occurs by the movement of oxide ions through the crystal lattice. This movement is owing to thermally activated hopping of the oxygen ion moving from crystal lattice site to crystal lattice site, with a superimposed drift in the direction of the electric field.

- **Cathode (Air Electrode) and Anode (H_2/CO Electrode)**

The cathode shows oxidation atmosphere where oxygen molecules are reduced to oxygen ions. At high temperature, it is particularly strong oxidizing environment, which made it not possible to use lower coat metal but favor the use of noble metal, semi-conducting oxides, or conducting oxides. The anode shows the reducing environment of the fuel gas and it allows for the use of a range of metals. Porous nickel has been the most widely employed anode materials. SOFC electrodes must meet the following requirements [2,19,20].

1. High electronic conductivity
2. Minimal inter-diffusion with adjacent materials
3. Chemical and mechanical stability (at 600-1000°C in oxidizing condition for the cathode and in highly reacting conditions for the anode)
4. Thermal expansion coefficient that matches that of electrolyte
5. Sufficient porosity to facilitate transport of O_2 from the gas phase to the electrolyte

- **Electrolyte**

The current transfer in solid electrolyte involves the movement of oxygen ions (O^{2-}) vacancies. A criteria to select an electrolyte is its ionic conductivity, which is temperature dependent. Ceramic ion conducting electrolytes are available for operating over a wide rang of temperature from 450-1000°C. Basic dependent for a solid oxide electrolyte is [2,19,21]:

1. Free of porosity
2. High oxygen ion conductivity
3. Very low electronic conductivity
4. Phase stability
5. Chemically stable at high temperatures

6. Chemically stable in reducing and oxidizing environments
7. Thermal expansion that matches electrodes
8. Compatibility with electrode and interconnect materials

- **Interconnect (between Cathode and Anode)**

The interconnect material is used to electrically connect the anodes and cathode of stacked cell in series. Interconnect materials range from high cost ceramic materials to low coat stainless steel depending mainly on the SOFC operating temperature [22]. The requirements of interconnect materials are [19,20]:

1. High density with no open porosity
2. High electronic conductivity and negligible ionic conductivity
3. Stable in both oxidizing and reducing atmospheres
4. Chemical and thermal expansion compatibility with other component
5. Stable under multiple chemical gas streams
6. Absence of mass transport effects in the presence of chemical gradients that may lead the formation of voids or contact resistances
7. No time-dependent phase changes or re-crystallization between 25-1000°C

2.2 Operating regimes and typical SOFC components

Based on the behavior of ceramic electrolyte material and properties of the interconnect materials, three operating temperature regimes can be achieved as high temperature (>800°C), intermediate temperature (600-800°C) and low temperature (400-600°C). The operating temperature will also be classified by features such as possibility of internal fuel reforming, the possibility in operating in conjunction with gas and steam turbines and the type of balance of plant equipment required. Table 2.2 shows some typical materials used in SOFC at different operating temperature.

Table 2.2. Potential SOFC components at operating temperatures [23].

SOFC component	Operating temperature		
	>800ºC	600-800ºC	400-600ºC
Electrolyte	Y doped ZrO_2	-Y or Sm doped ZrO_2 - Ceria-based	Gd or Y or Sm doped CeO_2 - Sr or Mg doped $LaGaO_3$: Composite electrolytes (ceria- and zirconia-based layers)
Cathode	$La_{1-x}Sr_xMnO_3$ (LSM)	$La_{1-x}Sr_xMn_{1-y}Co_yO_3$ (LSMC) (diffusion barrier required between cathode and YSZ electrolyte)	-$La_{1-x}Sr_xCo_{1-y}Fe_yO_3$ (LSCF) used with CeO_2: -$La_{1-x}Ca_xCo_{1-y}Fe_yO_3$ (LCCF) used with CeO_2: - $Sm_{1-x}Sr_xCoO_3$ (SSC) used with $LaGaO_3$
Anode	Ni-ZrO_2(-Y_2O_3)	Ni-ZrO_2(-Y_2O_3)	Ni-ZrO_2(-Y_2O_3) Oxide materials
Interconnect	Ca or Mg doped $LaCrO_3$	Special metallic or cermet bipolar plate: stainless steel (700°C) bipolar plate	Stainless steel bipolar plate

2.2.1 High temperature operating regime (>800°C)

Most research efforts up to date have investigated the high temperature SOFCs and a number of stack systems have developed at different stages of testing and demonstration. An advantage of the high temperature operating regimes is that internal reforming can occur spontaneously. Operating temperature above 800°C requires costly materials. Common problems are voltage degradation due to electrode sintering and interfacial reaction and mechanical stress due to differential shrinkage and internal expansion. Also, high temperature sealing is a challenging problem in

planar SOFCs. Typically, suitable materials for high temperature operation are YSZ electrolyte, strontium doped lanthanum maganate (LSM) cathodes and Ni-cermet anode [20,24].

2.2.2 Intermediate-temperature operating regime (600-800°C)

SOFCs operating at intermediate and low temperature regimes are at less developed stage than the high temperature one, however much interests in lower operating temperatures have gained importance more recently mainly as a means to reduce costs. Cell and system costs at these operating temperature can be greatly reduced compared to high temperature operation because of the use of low cost materials (e.g. stainless steel bipolar plate instead of ceramic interconnects) [25,26]. Lower temperatures may possibly lead to longer lifetimes and less complicated and costly designs. In addition, the temperature range considered is suitable for operation in combination with steam turbines.

In term of material selection for operating temperatures between 600-800°C, the conventional 8 mol% Y_2O_3-ZrO_2 electrolytes is replaced by either $Ce_{0.9}Gd_{0.1}O_{1.95}$ (GDC 10 mol%) or $La_{0.9}Sr_{0.1}Ga_{0.8}Mg_{0.2}O_2$ (LSGM) [25]. Ceria-based solid solution have been regarded as the most promising electrolytes in the intermediate temperature fuel cell system [26] due to the ionic conductivity of ceria-based is higher than of yttria-stabiliized zirconia at this temperature range. The ceria-based materials have ionic conductivity at 0.1-1.0 S/cm [27]. Strontium and manganese doped lanthanum-cobaltate (LSMC) showed a thermal expansion compatible with that of YSZ electrolyte and Ni-cermet appears as the most likely choice for the anode as it offers suitable electrochemical and thermo-mechanical properties and has a moderate cost.

One of the major problems encountered today to develop intermediate temperature solid fuel cells (IT-SOFC) is the large cathode overpotential caused by the reduced operation temperature. Mixed ionic and electronic conductors (MIECs) have been widely studied as cathodes for IT-SOFC. The electrical overpotential on the MIEC oxide cathode presents a combined activation barrier of many underlying transport processes that contributes significantly to the total energy loss, particularly at low operating temperature. Therefore, it is very important to understand the

knowledge on the mechanism and kinetics of the oxygen exchange with MIEC to improve the development of cathode materials for this technology. The elementary steps in the cathodic oxygen reduction reaction on a mixed conducting electrode material can be resumed as follows [29].

1. Diffusion of O_2 molecules in the gas phase to the electrode
2. Adsorption of O_2 on the surface of the electrode
3. Dissociation of molecular into atomic oxygen species
4. Charge transfer from the electrode to oxygen species before or after dissociation
5. Incorporation of oxide ions in the crystal lattice of the electrode
6. Bulk transportation of O^{2-} ions through the electrode to the electrode/electrolyte interface
7. Transportation of O^{2-} ions across the electrode/electrolyte interface

2.2.3 Low-temperature operating regime (400-600°C)

Operation further reductions at lower temperature (400-600°C) give rise to further reductions in materials and design costs and creates opportunities for markets other than stationary power generation (e.g. transport). Low cost metals and metal fabrication techniques can be employed and gas sealing problems are easier to overcome [27]. Also, cheaper materials can be used for the balance of plant equipment including heat exchangers, pumps etc. Longer lifetime are likely to result from lower operating temperatures and contributing to the economic viability of fuel cell stack. The upper temperature range of 600-700°C is also suitable for indirect internal reforming of methane although direct internal reforming will take place at 600°C. Candidate materials suitable for electrolyte at lower operating temperature include CeO_2 and $LaGaO_3$-based materials. Previous investigation showed CeO_2-based electrolyte had power densities comparable to those of zirconia-based systems [25] towards the upper end of the temperature range (700°C) and a good thermal expansion match with ferritic stainless steels. For electrode materials, strontium and cobalt doped lanthanum ferrate (LSCF) is a suitable cathode material for used with ceria-based electrolyte for operation at high temperature close to 700°C. Other interesting candidate for cathode is strontium doped samarium-cobaltate (SSC)

[28,30]. Ni-cermet has been the most commonly used as anode material so far, however its use in the this temperature range may cause problems such as the formation of carbon deposits and NiO formation which may reduce the cell performance [27].

2.3 Perovskite and K_2NiF_4 – type structure

Oxide groups consisting of two more different cations are called complex or mixed oxides and many types of structures are different from those of the simple oxides. In some special cases, oxide consisting of a single cation in different oxidation states are also classified as mixed oxides. For example, Eu_3O_4 mixed oxide consists of Eu(III) and Eu(II) in 6- or 8- coordination, respectively. However, the most typical structure of a mixed oxide consists simply of two or more different cations with different oxidation states, ionic radii, and coordination numbers. This diversity which comes from the complexity of these structures, results in a larger number of different properties as compared to those of simple oxide. One of the most well known and important complex oxide structures is the perovskite structure (ABO_3). The structure of such oxides displays the most interesting complexity. Because the A and B ions in this structure are close in size, oxide of this type are typical examples of the versatility of mixed oxides. In the ideal case, one six fold-coordinated ion occupies the A site and another six fold-coordinated cation occupies the B site; however in some cases mixing of cations on A and B site ion occurs [31]. Therefore a unique feature of mixed oxide compounds is the display of a variety of properties that are partially the result of the variety of the structures. In particular among mixed oxides the perovskite oxides are well known for displaying a multitude of structures and properties.

2.3.1 Crystal structure

- ABO_3-type

Perovskite oxides comprise large families among the structures of oxide compounds and several perovskite-related structures are currently recognized. Typical structures consist of large sized 12 coordinated cations at the A site and small sized 6 coordinated cations at the B site. Several complex halides, sulfides and oxides have a perovskite structure. In particular $(Mg,Fe)SiO_3$ or $CaSiO_3$ is thought to be the predominant compound in the geosphere [32,33]. Perovskite compounds with different combinations of charged cations in the A and B sites, e.g. 1+5, 2+4 and 3+3, have been discovered. In addition many ABO_3 compounds crystallize in polymorphic structures which show only a small distortion from the most symmetrical form of the perovskite structure. The ideal structure of perovskite is illustrated in Figure 2.2.

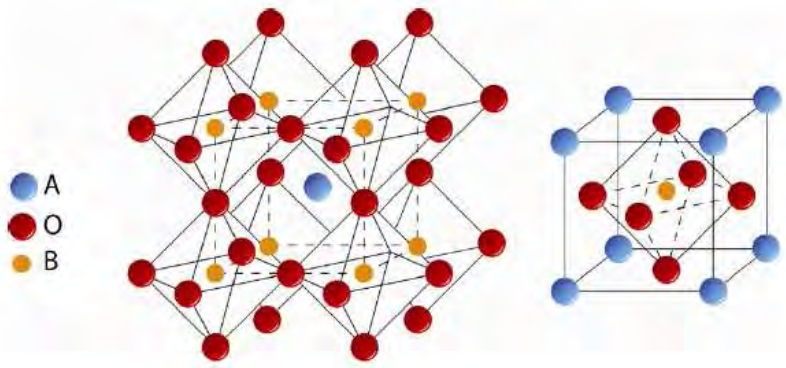

Figure 2.2 ABO_3 perovskite structure [34].

The partial substitution of cations in the ABO_3 perovskite structure by cations with a lower valence either leads to formation of oxygen vacancies or to charge compensation by electronic charge carriers. The ratio of the ionic to electronic conductivity may vary markedly and in a complex manner with temperature, oxygen activity and dopants. The nature and extent of oxygen non-stoichiometry greatly affects the level of ionic conductivity, requiring judicious choice of the substituting ions. Large numbers of disordered oxygen vacancies at elevated temperatures may lead to the onset of high ionic conductivity. There are many investigations on the composition–property relationship of ABO_3-type oxides with A = Ln (Lanthanides),

Ca, Sr, Ba; B= Cr, Mn, Fe, Co, Ni, Ga, In, with mixed occupation of the A- and B-sublattices.

- **A_2BO_4-type**

The structure of the Ruddlesden–Popper-type phase A_2MO_4 is shown in Figure 2.3.

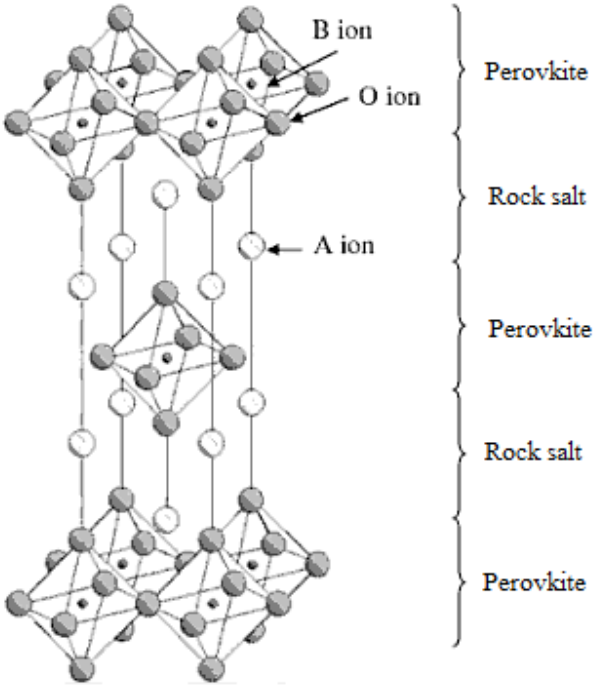

Figure 2.3 A_2BO_4 – type structure [35].

A_2BO_4 oxides with the perovskite-related K_2NiF_4- type structure are less intensively investigated. Recent results on lanthanum cobaltites and nickelates indicated enhanced chemical stability and moderate thermal expansion. Compounds with formula A_2BO_4 generally have the tetragonal K_2NiF_4 structure when the radius of the A cation is $1.0 < r_A < 1.9$ A°, the radius of the B cation is $0.5 < r_B < 1.2$ A°. The larger A cation has nine-fold coordination and the smaller B cation has octahedral coordination. This structure can be described as containing alternate layering of perovskite (ABO_3) and rock salt (AO) units [36]. It contains δ excess interstitial oxygen defects (O_i'' ions) per formula unit located between the paired AO rock salt bilayers that alternate with the ABO_3 layers [35]. These oxides (A_2BO_4), as well as

perovskite (ABO_3), have a well-defined bulk structure and the composition of cations at both A and B sites can be variously changed without destroying the matrix structure, they therefore can be very useful as model systems to investigate the relationships between solid-state properties and catalytic performance of catalyst.

2.3.2 Tolerance factors in ABO_3 and A_2BO_4

In the ideal structure of ABO_3 and A_2BO_4, the larger A site cations locate at the corners of the cube, the B site ions at the body center, and the oxygen ions at the centers of the faces. The A-site ion of structure is coordinated by twelve oxygen ions whereas the ion located at the B site has sixfold coordination. The structure can withstand wide variations of the elements at the A and B sites.

The stability of the structures is frequently defined by Goldschmidt in terms of the tolerance factor , *t*, in Equation 2.4. Where, r_A , r_B , and r_O are the ionic radii of A, B and O ions, respectively [37]. The relationship between ionic radii in the ABO_3 and A_2BO_4 structure can be illustrated in Figure 2.4.

$$t = \frac{(r_A + r_O)}{\sqrt{2}(r_B + r_O)} \qquad (2.4)$$

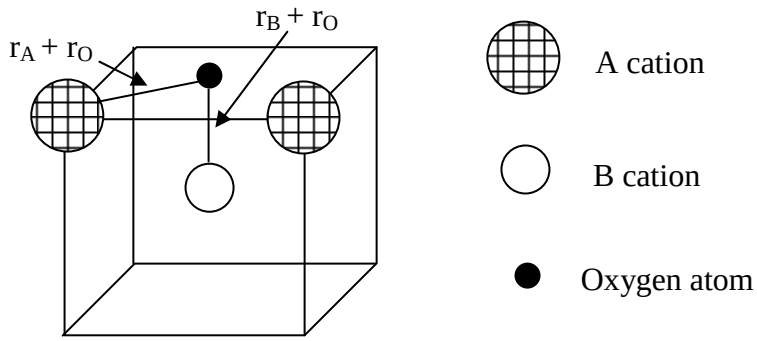

Figure 2.4 The relationship between symmetry and ionic radii in the perovskite.

For the stability of ABO_3-type structure, the *t* values are defined for $0.77 < t < 1.00$ [35]. Designing *t* close to unity leads to higher symmetry and smaller unity cell volumes [36]. The perfect cubic close packing structure ($t = 1$) is achieved when the A-site cation has the same size as the oxygen ion (1.40A°) and the B-site cations are located in the octahedral holes formed only by oxygen [37]. In a perfect cubic perovskite structure, the B-O-B chains are linear, i.e. the bond angle of 180°. Deviation from cubic symmetry results in tilting of the BO_6 octahedra, therefore, reducing B-O-B bond angles. For $t > 1$ the hexagonal structures tend to be stable whereas for $t < 1$ the lattice structure changes from cubic to rhombohedral and then to orthorhombic [38].

Stable A_2BO_4-type structures, an ideal matching between the A cation and one layer of linked BO_6 octahedra, occur for $t = 1$ and the structural form is tetragonal with the space group I4/mmm. In the range of $t = 0.8$-0.9, the distorted structure may show orthorhombic, rhombohedral, tetragonal, monoclinic and triclinic asymmetry at room temperature but it transforms to the cubic structure at ambient temperature. Ganguly and Rao *et al.* [32] proposed that A_2BO_4 compounds with the *t*-value near the lower limit e.g. $t = 0.85$, exhibit superlattice reflection lines in their diffraction patterns associated with a rotation of BO_6 octahedra around the *c*-axis or a tilting of BO_6 octahedra [39].

2.3.3 Properties of structure

- **Mixed ionic-electronic conductors**

The perovkite oxides exhibit high oxygen ion conductivity due to the high oxygen vacancy concentration in the structure and a high electronic conductivity due to the mixed-valence state. For example $La_{1-x}Sr_xBO_{3-\delta}$ [40], when the B ions can take a mixed-valence state, charge neutrality is maintained by both the formation of oxygen vacancies and a change in the valence state of the B ions. The concentration of oxygen vacancies can also be increased by mild B-site ion substitution, such as Cu and Ni ions which naturally take the divalent oxidation state [41]. If valence state of the B ions is fixed, neutrality is maintained only by the formation of oxygen vacancies. The oxides may be predominantly ionic conductors.

- **Electrical properties**

The electrical conductivity of perovskites also shows wide variations. Several compounds have been used for their dielectric properties, while others show metallic conductivity, although most are semiconductors. As other compounds, the electrical behavior in perovskites depends on the outermost electrons, which may be localized at specific atomic sites or may be collective. Since localized electrons may carry a spontaneous moment, there is a strong correlation between the electrical and magnetic properties of perovskites. Rare-earth perovskites containing transition ions show widely differing electrical properties. The electrical properties of perovskites have aroused special interest since the discovery in 1986 of superconductivity at 40 K in cuprates. These cuprates are whole superconductors, exhibiting a mixed valence of copper Cu^{2+}–Cu^{3+}. Among these, the exception is Ce–doped Nd_2CuO_4, with Tc close to 25 K, which belongs to a different structural type and is an electron superconductor. All these compounds have a common feature, the two-dimensional character of the structure, which has been shown to be an important factor for the existence of superconductivity at high temperature [42].

The electrical conductivity of perovskite was measured using DC 4-probe or “Kelvin” measurement as illustrated in Figure 2.5.

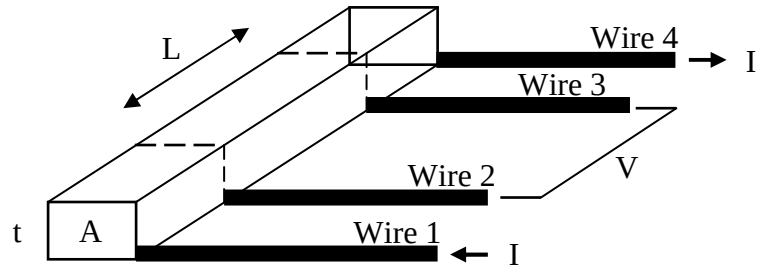

Figure 2.5 DC 4-probe method.

The measurement method includes a forced current, I, through the outer wires 1 and 4 and a measurement of the voltage drop over wire 2 and 3, using a very high ohmic measurement device, so that the current flowing through wire 2 and 3 nearly zero. In that case the individual, additional contact resistance does not play a role as it cancels out of the equation. To study the behavior of the structure an I/V curve is generated, typically in the μA to the mA range. If the graph shows a straight

line, the structure behaves as an Ohmic resistor. If assume that the resistance of a structure to be R, the following Equation 2.5.

$$R = \frac{\rho L}{A} \qquad (2.5)$$

Where L is the length of the structure (m)

A is the area (width x thickness) of the cross section (m^2)

ρ is the specific resistivity (Ω.m of the practical unit μΩ.cm)

- Oxygen permeation

The mixed conductive perovskite membrane can be an intrinsically mixed conductor or a mixture of an oxide ion conductor and an electronic phase. Because of their properties, these materials could be developed as membranes for oxygen separation. There are two concepts of oxygen separators using a mixed ionic-electronic conducting membrane: current driven membranes and pressure driven membranes. In the first case, under an electrical field, molecular oxygen is dissociated at the cathode into oxide ions which migrate through the membrane and recombine as O_2 at the anode. This allows the production of given amounts of oxygen under pressure. In the second case, a difference of oxygen partial pressure between an oxygen rich compartment and an oxygen poor compartment is the driving force for the migration of O_2 from the rich to the oxygen poor compartment, as illustrated in Figure 2.6.

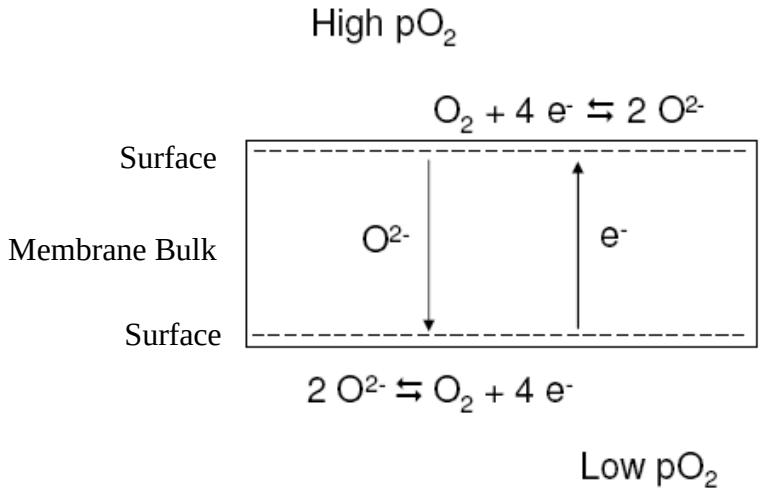

Figure 2.6 Oxygen transport during oxygen permeation [44].

The oxygen anions permeate from the high to the low partial pressure side, while overall charge neutrality was maintained by a counter balancing flux of electrons (and/or electron holes). Mechanism for oxygen permeation through a mixed ionic-electronic conducting membrane can be described as follows [43]:

1. Mass transfer of gaseous oxygen from the gas phase with high oxygen partial pressure to the membrane surface
2. Reaction between the molecular oxygen and oxygen vacancies at the membrane surface
3. Dissociation and electron transfer, giving chemisorbed oxygen species
4. Incorporation in membrane surface layer
5. Diffusion of lattice defects to interior
6. Diffusion of bulk oxygen vacancy across the membrane
7. Association and electron transfer, forming chemisorbed oxygen species
8. Desorption from the surface
9. Mass transfer of oxygen from the membrane surface to the gas phase with low oxygen partial pressure

When the oxygen transport in a membrane is at the steady state, the oxygen permeation flux can be calculated by the Wagner Equation 2.6 [3].

$$Jo_2 = \frac{RT}{(4F)^2}\frac{\sigma_{amb}}{L}\ln\frac{P'o_2}{P''o_2} \qquad (2.6)$$

Where $P''o_2$ and $P'o_2$ stand for the oxygen partial pressure in the higher and lower oxygen partial pressure compartment, respectively, L is the sample thickness, T is the temperature, R is the universal gas constant and F is the Faraday constant. The ambipolar conductivity is defined as:

$$\sigma_{amb} = \frac{\sigma_e \sigma_i}{(\sigma_e + \sigma_i)} \qquad (2.7)$$

Where σ_e is the electronic contribution and σ_i is the ionic contribution to the total conductivity.

There is no need for an external current but the membrane must be a mixed conductor to allow the reverse flow of the electrons needed for the oxygen dissociation. The expected oxygen permeation flux in such membranes depends on the difference of oxygen partial pressure between the two compartments, on the membrane thickness and on the ionic and electronic conductivity of the membrane.

- Thermal expansion

To minimize stresses during cell fabrication and cell operation, thermal expansion of the cathode should be matched with other SOFC component materials, especially electrolyte and interconnect.

Over small temperature ranges, the linear nature of thermal expansion leads to expansion relationships for length in terms of the linear expansion coefficient. The fractional thermal expansion of uniform linear objects is proportional to the temperature change. The calculation is set up in the form of Equation 2.8 [46].

Figure 2.7 The relationship for length in terms of the linear expansion [47].

$$L/L_o = \alpha\, L_o/\Delta T \qquad (2.8)$$

Where L_o is original length (mm)

L is length change (mm)

ΔT is original temperature – final temperature

α is thermal expansion coefficients

The thermal expansion coefficients of K_2NiF_4-type oxides are generally lower than the thermal expansion coefficients of the perovskite-typed oxides of comparable cationic compositions. The differences in thermal expansion between measurements in air and in argon environment are also smaller for K_2NiF_4-type oxides compared with the differences for the ABO_3 oxides [48]. It is because the K_2NiF_4-type structure has interstitial oxygen in rock-salt layer and there oxygen can migrate and replace the oxygen loss in the lattice, but in perovskite structure when oxygens loss from the lattice at high temperature, M-O bond energy decreases.

2.3.4 Synthesis

2.3.4.1 Powder synthesis

The procedure for preparing K_2NiF_4- type membranes consists of three steps: powder synthesis, calcining and sintering. Powder synthesis plays a critical role in determining the particle size of K_2NiF_4 powder, and consequently has an influence on the microstructure of K_2NiF_4 membrane. There are many routes to synthesize K_2NiF_4, such as a conventional solid–state reaction method and a wet chemical process that includes hydrothermal synthesis, metal–EDTA, chemical co-precipitation and the sol-gel process, etc.

- Solid-state reaction

The most common procedure for K_2NiF_4 oxides synthesis via solid state reactions is the calcination of a homogenous mixture of the corresponding metal–carbonates, hydroxides, and oxides. This is also known as ball milling and calcination method. This method is very convenient but the impurities are introduced from raw materials, milling media, and the calcination container. Because of the high temperature required for the complete reaction, the problems such as multiphase can

be minimized in order to generate homogeneous high performance K_2NiF_4. For example, LSCF represents a typical case. Raw materials La_2O_3, $SrCO_3$, CoO_3, and Fe_2O_3 were mixed and ball–milled. After drying, the mixed powders were calcined at 1,000^oC to remove impurities and to achieve single–phase K_2NiF_4 powder.

- Hydrothermal synthesis

This synthesis method is applied to produce advanced mixed oxides or compounds with specific characteristics in their composition such as pigment for electronics. This process generally uses temperature between the boiling point of water and the material's critical temperature, while the pressure can be as high as 15MPa [45,49]. Consequently, the calcinations step required by other steps discussed can be eliminated in this case. Hydrothermal synthesis can be used to assist the sol-gel technique in controlling the particle size. The materials used are generally inexpensive, easy to control in terms of its size, shape and stoichiometry. Elimination of impurities associated with milling and other advantage mentioned will result in very fine and highly reactive ceramic powders [50].

- Co-precipitation

One of the oldest techniques comprises of an aqueous solution containing the desired cations and another solution acting as a precipitation agent. Filtration, drying and thermal decomposition are followed to acquire desired products. The desired products and their physical properties are adjusted using pH, mixing rates, temperature and concentration. Although different precipitation rates sometimes result in inhomogeneities, the morphology, purity and composition are well achieved. A doping agent may be sometimes added to assist homogeneity of composition. The resultant compound requires a lower sintering temperature than those employed in the conventional method [50] due to the high dispersion of different metals in the precipitate. The particle size is typically in the range of few nanometers, which is achieved by careful precipitation of suitable surfactants and capping agents [51]. A careful control of pH and precipitation temperature also produce materials with an exact stoichiometric condition.

- **Sol-gel technique**

The sol-gel technique involves the production of an amorphous like gel, followed by dehydration at low temperature [52]. This technique delivers high purity and excellent composition control.

EDTA, citrate and modified citrate route

This route is very popular and has been utilized extensively due to its advantages such as carbonate-free and chemically homogeneous final oxide compounds with a high relative density. Citric acid, ethylenediaminetetraacetic acid (EDTA) or glycine can be used as chelating agent. This route involves complexation of metal ions in EDTA/citric acid, evaporation of water solvent, and thermal decomposition of the complex with subsequent formation of perovskite phase. A chelating agent is used to prevent partial segregation of metal components, which could occur in the case of different stabilities with the metal ions in solution. In some cases [53] a polyol (e.g. ethylene glycol) is added with chelating agent to promote the polymerization and to produce an organometallic polymer, which results in a perovskite precursor after drying and pyrolysis.

Sol-gel process involves producing precursor from citric acid and metal nitrate or acetate before thermal decomposition. For example, the production of Sr-substituted $LaMnO_3$ perovskite powder by the citrate amorphous process produced the manganese citrate-nitrate precursor as shown in Equation 2.9.

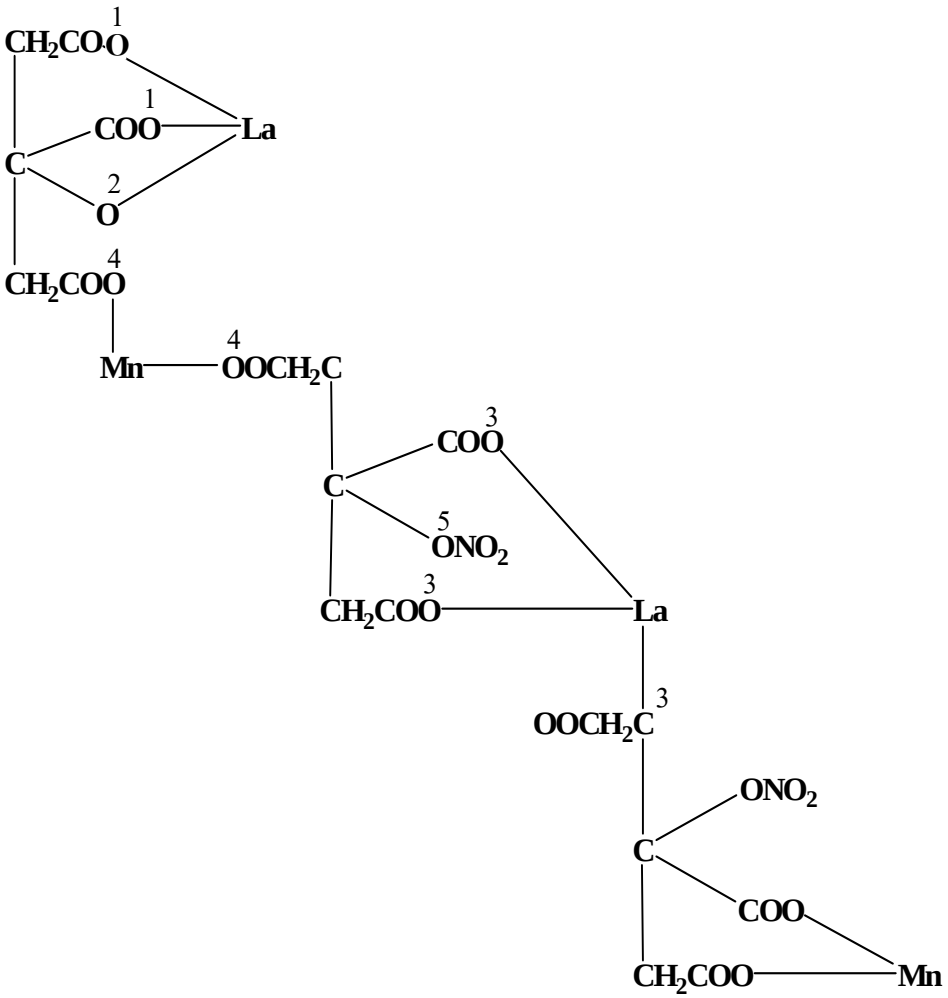

(2.9)

In the complex, lanthanum is triply charged and replaces normal citrate formation in the hydrogen of two -COOH groups (shown in position number 1) and it replaces in the hydrogen of one -OH group (shown in position number 2) and it replaces in the hydrogen of three -COOH groups (shown in position number 3). As manganese is divalent state replaces in the hydrogen of two -COOH groups (shown in position number 4) while NO_2 replaces the hydrogen of one -OH group (shown in position number 5), respectively [47].

In all cases the minimum amount of citric acid used was necessary to bond the metals if all the NO_3^- ions were replaced. The amounts of metal and citric acid should not be less than equimolar. If the high amount of citric acid was used, Mn_2O_3 was presented from the complex as in Equation 2.10.

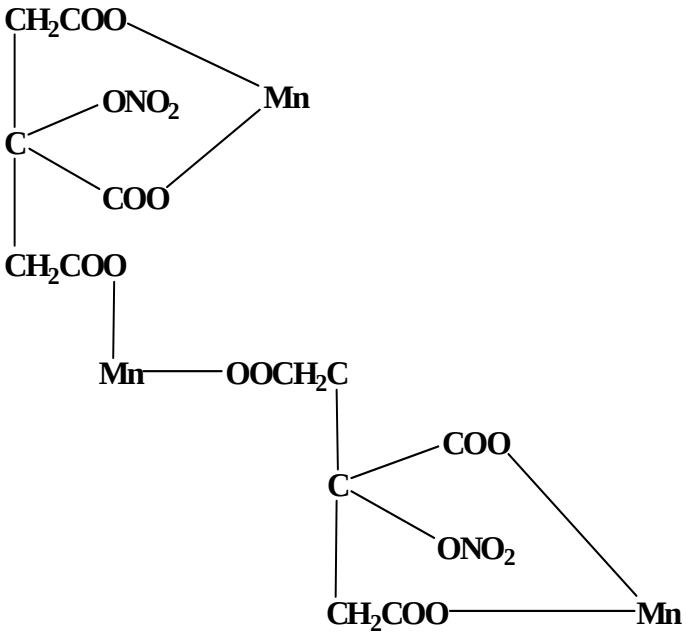

(2.10)

The formation of this complex would also liberate NO_3^- groups for each two molecules of $Mn(NO_3)_2$ originally present in solution. The formation of above structure would allow some citric acid, water and nitrate ions to be lost during the preparation of gel. Every three molecules of citric originally present one remains uncombined and may be removed from the mixture by either evaporation or decomposition to yield acetone, carbon dioxide and water during the precursor preparation in the vacuum oven [47].

2.3.4.2 Calcination [54]

The calcination (also referred to as calcining) is a thermal treatment process applied to ores and other solid materials in order to bring about a thermal decomposition, phase transition, or removal of a volatile fraction. The calcination process normally takes place at temperatures below the melting point of the product materials. The objects of calcination are usually: (1) to drive off water presenting as absorbed moisture, as water of crystallization or as water of constitution; (2) to drive off carbon dioxide, sulfur dioxide or other volatile constituents; (3) to oxidize a part or the whole of the substance. There are a few other purposes for which calcination is employed in special cases and these will be mentioned as roasting, firing or burning.

2.3.4.3 Sintering [55]

Sintering is the process whereby powder compacts are heated so that adjacent particles fuse together. The fusing of particles results in an increase in the density of the part or materials and hence the process is sometimes called densification. The density of the component can change during sintering, depending on type of materials and sintering temperature.

When a powder aggregate is sintered, three stages of process can be distinguished, as shown in Figure 2.8. In first stage, the necks form between the particles, at points of particle contact. In second stage the individual particles are still distinguishable and the aggregate may increase in density. During this period, the necks become larger, resulting in the formation of an interconnected pore structure. During the third stage, the pores become isolated. Elimination of the interconnectivity of pores eliminates surface and vapor transport.

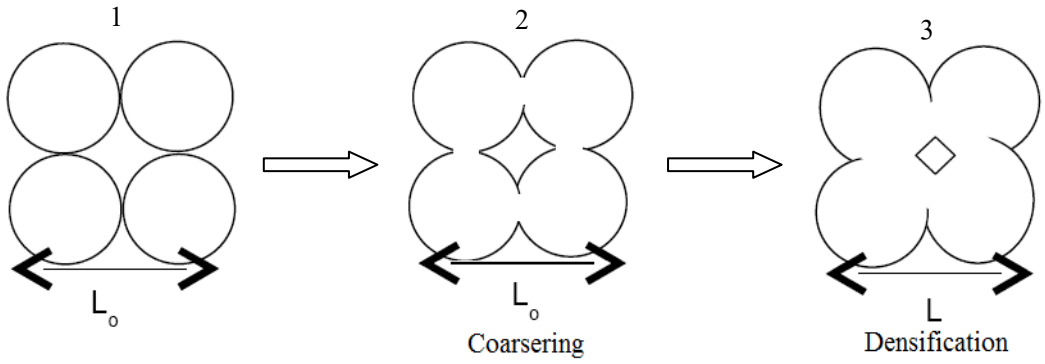

Figure 2.8 Mechanism of sintering.

Closed pores isolated from grain boundaries shrink very slowly because grain boundary diffusion is far away from the pores. The growth of grains hinders the theoretical density because the pore's growth is also enhanced. It is essential, therefore, to retard grain growth by using ultrafine particles as starting materials so that densification can continue to approach theoretical limit. Thus, surface diffusion becomes important in the case of very fine particles. During the sintering of two spheres with a grain boundary, the most important diffusion paths are surface diffusion, grain boundary diffusion, volume diffusion from the grain boundary to the neck surface, and volume diffusion from the sphere surface to the neck surface. Grain boundary diffusion and volume diffusion are the main mechanisms causing

shrinkage of the neck, whereas surface diffusion does not contribute to any shrinkage. The sintering rate also affected crystallization and growth processes, which occur concurrently.

CHAPTER III

EXPERIMENTAL

3.1 Chemicals

The chemicals listed in Table 3.1, were used without further purification.

Table 3.1 Reagents for synthesis of $La_{2-x}Ca_xNi_{1-y}Co_y(Ga, Ti)_zO_{4+\delta}$ materials.

Reagents	Formula Weight	Purity%	Company
$La(NO_3)_3 \cdot 6H_2O$	433.02	99.9	Himedia
$Ca(NO_3)_2.4H_2O$	236.15	99.0	Analytical
$Ni(NO_3)_2.6H_2O$	290.81	97.0	Ajax
$Co(CH_3OO)_2$	249.09	99.0	Wako
$Ga(NO_3)_2 \cdot xH_2O$	255.74	99.99	Aldrich
TiO_2	79.87	99.00	Fluka
$C_6H_8O_7$	192.43	99.5	Aldrich
HNO_3	63.01	65	Merck
liq.NH_3	35.05	25	Merck
C_2H_5OH	46.07	-	Merck

3.2 Synthesis of $La_{2-x}Ca_xNi_{1-y}Co_y(Ga, Ti)_zO_{4+\delta}$ powder by modified citrate method

The powders of $La_{2-x}Ca_xNi_{1-y}Co_y(Ga, Ti)_zO_{4+\delta}$, (x = 0.1-1.0, y = 0.1-0.9 and z = 0.01-0.1, 0.2) were synthesized in solution. Stoichiometric amounts of corresponding high purity metal nitrates and acetates (based on 3 g. of powder) were mixed and dissolved in 10 ml deionized water and followed by 15 ml nitric acid (65 wt%) under stirring at room temperature. Then citric acid with a ratio of citric acid to metal ions (2:1) was added into the solution. The homogeneous solution was stirred and slowly titrated with $NH_3.H_2O$ (25 wt%) until the pH value of the solution was adjusted to ~9 [56]. After that the combustion of the solution was taken place by slowly heating the solution on a hot plate to 200-300ºC. During combustion, the water was evaporated until a sticky gel was obtained and became the sponge-like solids expanded to occupy almost 2/3 of the beaker volume at the end. The resulting powder was ground by mortar and pestle, subsequently the synthesized powder was calcined in a air-muffle furnace at 1000-1350ºC for 6 hrs.

3.3 Preparation of disc

A round disc (20 mm in diameter and 1 mm in thickness) was prepared by loading 1.8 g groundly calcined $La_{2-x}Ca_xNi_{1-y}Co_y(Ga, Ti)_zO_{4+\delta}$ powder into the cavity of a KBr die. The die having the $La_{2-x}Ca_xNi_{1-y}Co_y(Ga, Ti)_zO_{4+\delta}$ powder inside was knocked against table for 2-3 times to evaporate air inside the powder. After the die was completely assembled, the plunger was brought to the surface of the powders gently for final leveling and smoothing surface as shown in Figure 3.1. Then, the powder was pressed by slowly applying pressure to 1.5 ton for 10 minutes. After the die was removed from the press, all the components were stripped away. Then the black discs were generally sintered in air at 1300-1400°C for 6 hrs to form dense membranes.

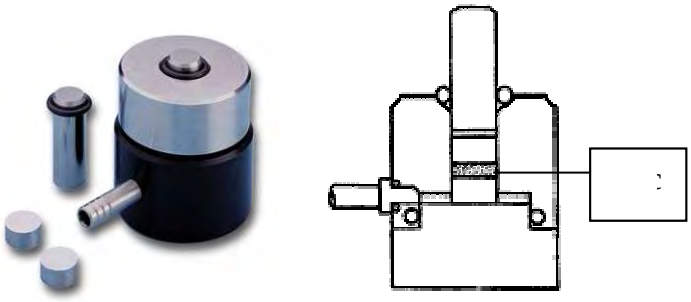

Figure 3.1 KBr die assembly.

3.4 Characterization of the $La_{2-x}Ca_xNi_{1-y}Co_y(Ga, Ti)_zO_{4+\delta}$ oxides

3.4.1 X-ray diffractrometry (XRD)

The X-ray diffraction patterns, for either powder or disc, were taken by using Rigaku, Ultima Plus X-Ray powder diffractometer equipped with a monochromator and a Cu-target X-ray tube (40 kV, 30 mA) and angles of 2θ from 20-70 degree at Department of Chemistry, Faculty of Science, Chulalongkorn University. The phase formations of perovskite powders were characterized after calcination and sintering by XRD.

3.4.2 Scanning electron microscopy (SEM)

The morphology of the membrane discs was carried out using a JEOL JSM-5800LV scanning electron microscopy, Oxford Instrument (model Link ISIS series 300) at Chulalongkorn University. This instrument uses X-rays or electrons scattered back from the surface illuminated by a restored electron beam to generate an image with remarkable three-dimensional qualities.

3.4.3 Density

Density of $La_{2-x}Ca_xNi_{1-y}Co_y(Ga, Ti)_zO_{4+\delta}$ disc were determined by the Archimedes immersion method using deionized water as a medium. Prior to the measurement, the membrane discs were boiled in deionized water for 5 hrs. Precisa Gravimetrics AG (model R 2055M–DR), at Department of Chemistry, Faculty of Science, Chulalongkorn University.

3.5 Properties measurement

3.5.1 Electrical conductivity

The electrical conductivity of the $La_{2-x}Ca_xNi_{1-y}Co_y(Ga, Ti)_zO_{4+\delta}$ materials was measured by the conventional DC 4-probes method using Pt electrode. Specimens of $La_{2-x}Ca_xNi_{1-y}Co_y(Ga, Ti)_zO_{4+\delta}$ were sintered at 1300°C for 6 hrs in air. The sintered disc was cut into a rectangular shape with approximate dimensions of 0.12 cm × 0.52 cm × 1.12 cm. Four platinum (Pt) wires were attached to the rod with Pt paste. Two current contacts were made at the rod edges, and two voltage contacts in between at a distance ***L***, as shown in Figure 3.2-3.3. The sample was then fired at 950°C for 10 min with a heating rate of 5°C/min to allow complete adhesion of the electrodes and to obtain a firm bonding and good electrical contact between the Pt wires and the sample. Measurements were performed from room temperature to 800°C with a heating rate of 5°C/min. The voltage (V) between the two inner electrodes and the current intensity (I) were recorded after the sample was left at each temperature at which measurement was taken, for 40 min. The electrical conductivity was calculated using Equation 3.1 [57].

$$\sigma = (I/V)*(L/(W*T)) \quad (3.1)$$

Where
- σ is electrical conductivity
- I is applied current (A)
- V is resulting potential (V)
- L is length between Pt (cm)
- T is thickness of membrane (cm)
- W is width of membrane (cm)

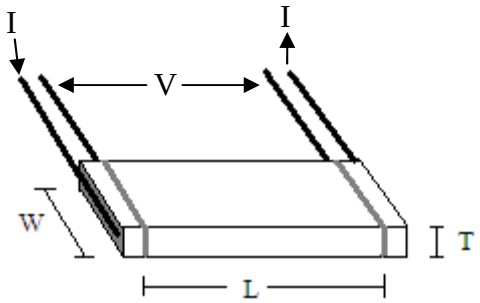

Figure 3.2 A rectangular specimen of $La_{2-x}Ca_xNi_{1-y}Co_y(Ga, Ti)_zO_{4+\delta}$ with four platinum (Pt) wire contacts W = width L = length T = thickness

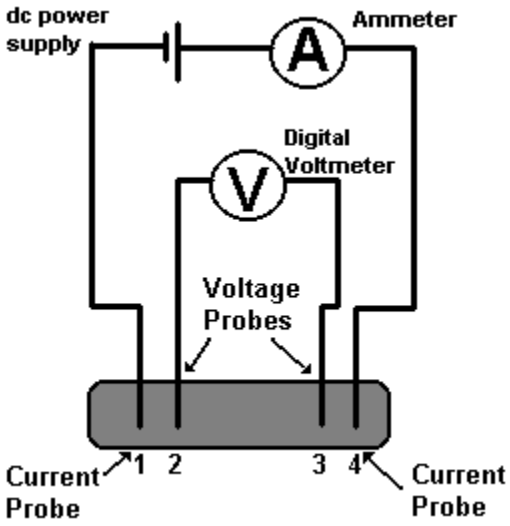

Figure 3.3 Scheme of DC 4-probes method [58].

3.5.2 Thermal expansion measurement

A dilatometer, NETZSCH DIL 4020C (from Department of Materials Science, Faculty of science, Chulalongkorn University) was used to determine thermal expansion coefficients (TEC) of the sintered specimens. The sintered disc was cut to a specimen (about 12 mm in length, 5 mm in width and 1.5 mm in thickness). The principle of dilatometer is to measure the changing of specimen length compared to the changing of temperature. In this evaluation, the heating rate of 10°C/min was applied to the specimen from room temperature to 800°C in air. The thermal expansion was calculated by Equation 3.2 [59].

$$\alpha = (1/L_1)*(L_2-L_1)/\Delta T \quad (3.2)$$

Where α is the thermal expansion coefficient (TEC)

L_1 is initial gauge lengths

L_2 is final gauge length

ΔT is the starting – terminal temperature of the experiment

3.5.3 Oxygen permeation measurement

Oxygen permeation measurement from air to He was performed on the high temperature oxygen permeation apparatus as shown in Figure 3.4. The details of this technique was described elsewhere [60]. The $La_{2-x}Ca_xNi_{1-y}Co_y(Ga, Ti)_zO_{4+\delta}$ oxide disc were polished into 20 mm in diameter and 0.7 mm in thickness. Then, porous catalyst was applied on the surface of the oxide disc by coating the disc surface with its own powder and then fired at 800°C for 10 min. Place the catalyst disc between the alumina tubes connected to gases. Dry air and He gas was supplied to each side of the specimen at a flow rate of 50 ml/min. Oxygen permeation flux from air to He was measured in temperature range of 600-1000ºC and analyzed by a gas chromatograph (VARIAN, CP-3800) equipped with Molecular sieve 13X column [60].

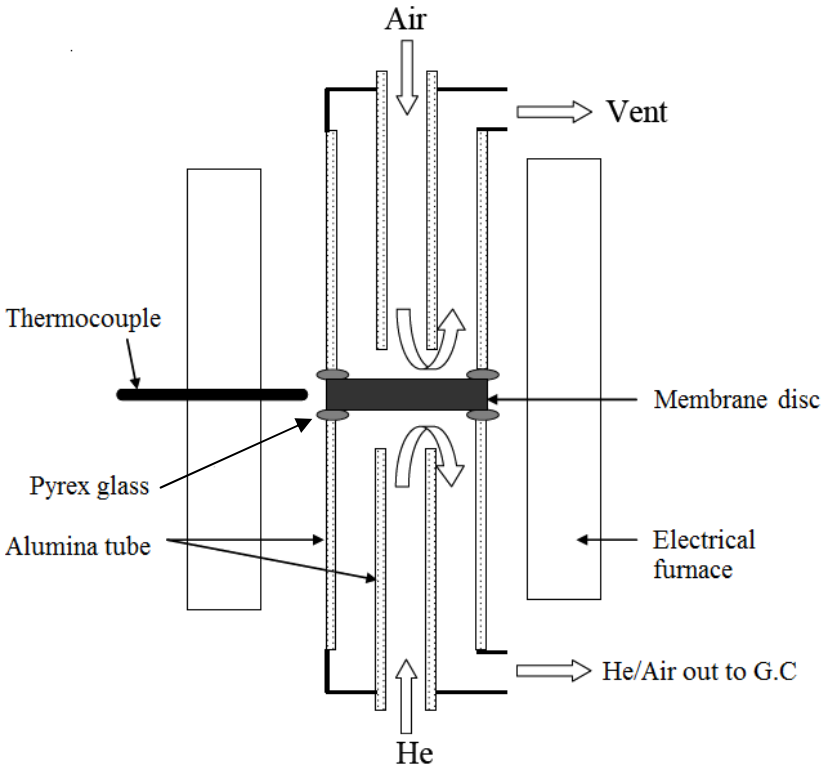

Figure 3.4 The diagram of the high temperature for the oxygen permeation measurement.

CHAPTER IV

RESULTS AND DISCUSSIONS

In this research, $La_2NiO_{4+\delta}$ were synthesized by modified citrate method and substituted by different contents of metal ions in A-site and B-site. The obtained samples were characterized for K_2NiF_4 type structure by XRD and for surface morphology by SEM. The properties of samples were investigated for electrical conductivity, oxygen permeation and thermal expansion coefficients.

4.1 Preparation and properties of $La_2Ni_{1-y}Co_yO_{4+\delta}$ (y = 0.0-0.9)

4.1.1 Synthesis of $La_2Ni_{1-y}Co_yO_{4+\delta}$ (y = 0.0-0.9)

$La_2Ni_{1-y}Co_yO_{4+\delta}$ (y = 0.0-0.9) powders were prepared and calcined at 1200ºC for 6 hrs. The XRD patterns are illustrated in Figure 4.1. $La_2Ni_{1-y}Co_yO_{4+\delta}$ with the composition of y equals to 0.0, 0.1, 0.2 shows the characteristic diffraction pattern of tetragonal K_2NiF_4-type structure (PDF No. 11-0557), with the main (103) peak at 2θ of 32°. The small diffraction peaks of 100, 002, 101, 102 and 110 planes of La_2O_3 impurity phase (PDF No. 05-0602) are also observed. Other compositions of $La_2Ni_{1-y}Co_yO_{4+\delta}$ ($y \geq 0.3$) exhibit a deformed structure of tetragonal perovskite to orthorhombic structure [61,62] and La_2O_3 impurities. This result is consistent with the data reported by *Ho-Chieh et al.* indicating that the transformation of tetragonal to orthorhombic structure could be observed when the samples were calcined at 1200°C in air [63].

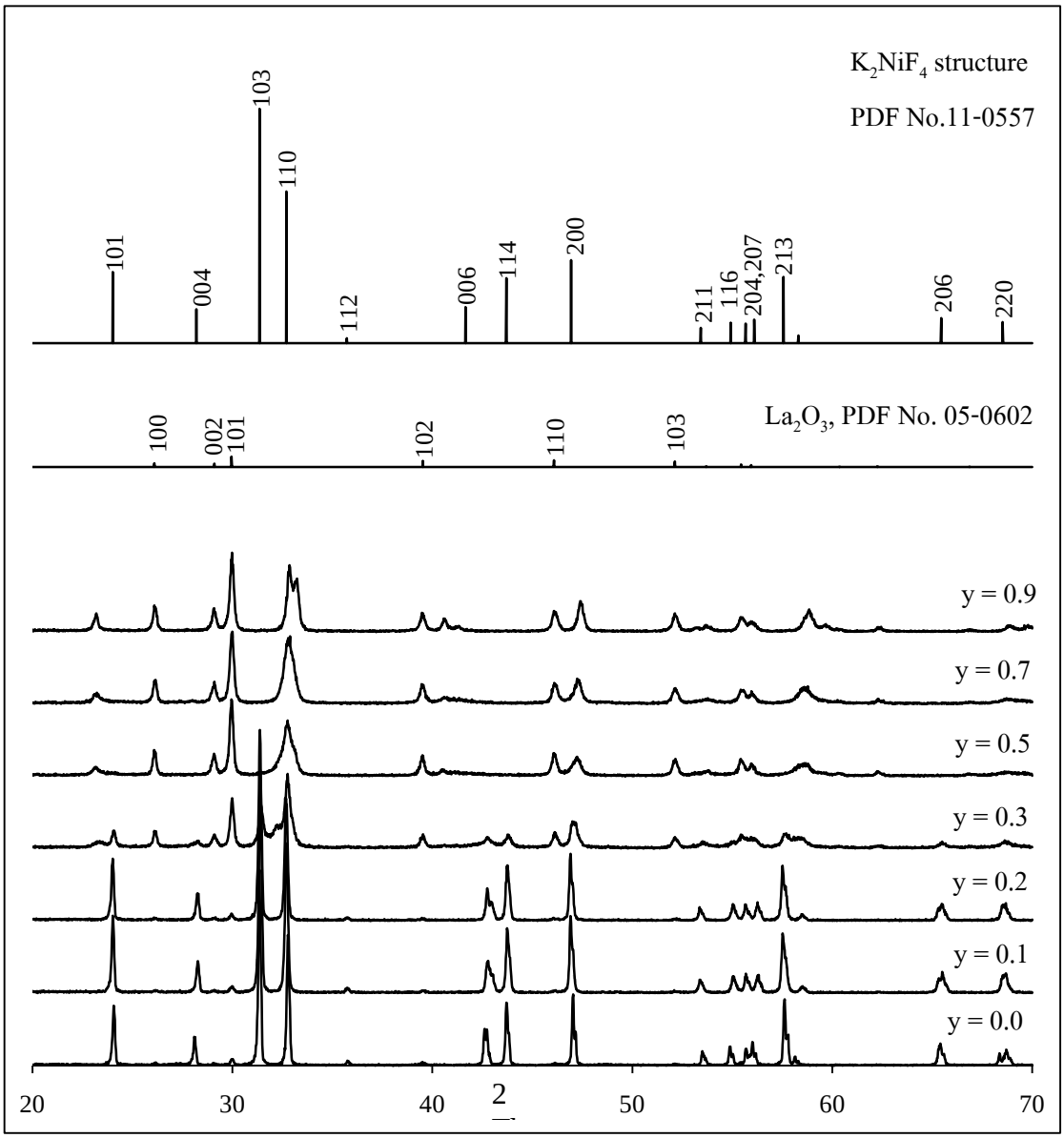

Figure 4.1 XRD patterns of $La_2Ni_{1-y}Co_yO_{4+\delta}$ (y = 0.0-0.9) after calcination at 1200°C.

4.1.2 Effect of calcination temperature

Since the La_2O_3 impurity was minimal observed on $La_2Ni_{1-y}Co_yO_{4+\delta}$ (y = 0.1-0.2) materials, the effect of calcined temperature was studied in order to get rid off the impurity. The $La_2Ni_{0.9}Co_{0.1}O_{4+\delta}$ and $La_2Ni_{0.8}Co_{0.2}O_{4+\delta}$ were prepared and calcined at 1000ºC-1350ºC for 6 hrs. The XRD analyses for phase identification were performed and the spectra are displayed in Figure 4.2.

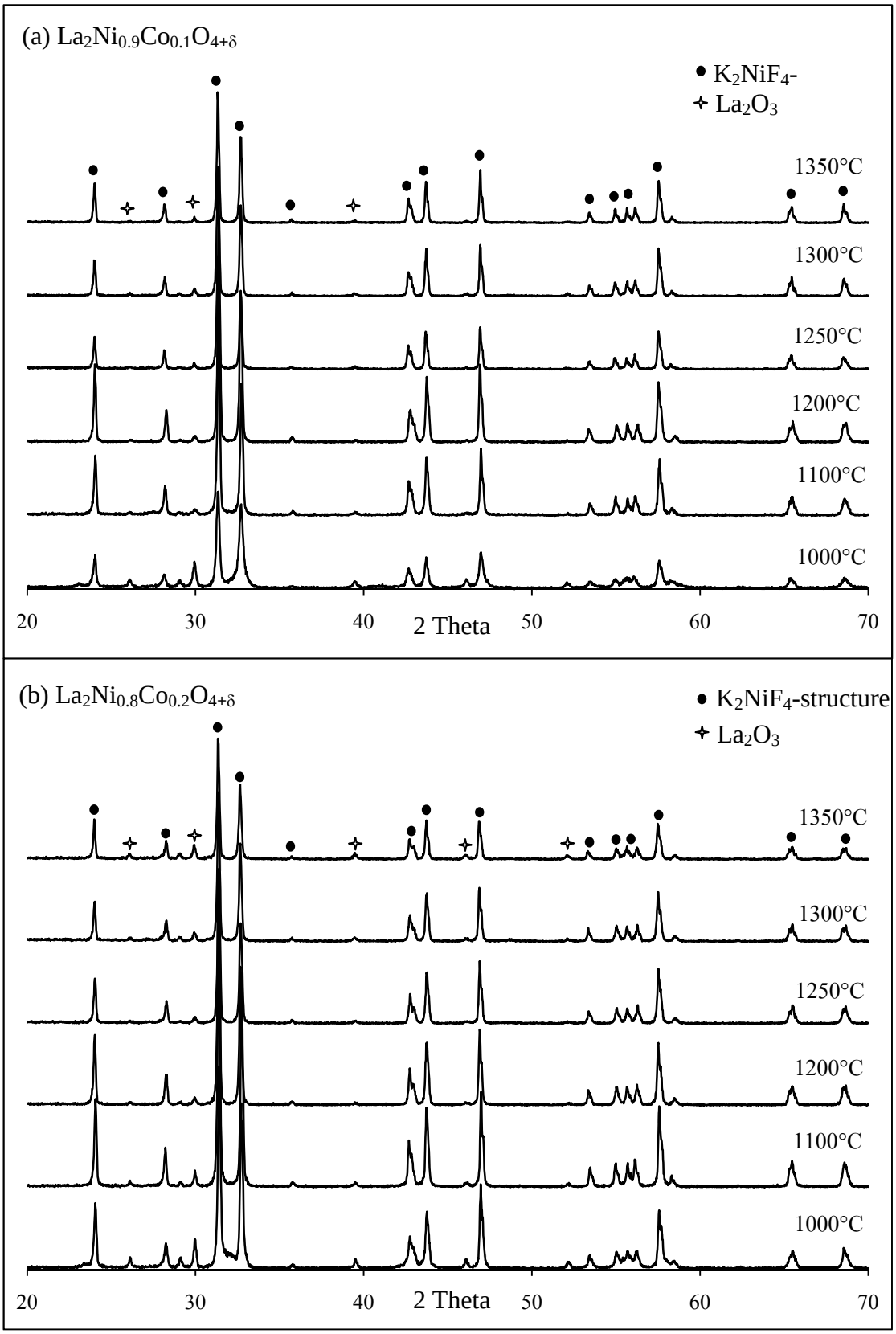

Figure 4.2 XRD patterns of calcined materials at various temperatures (a) $La_2Ni_{0.9}Co_{0.1}O_{4+\delta}$, (b) $La_2Ni_{0.8}Co_{0.2}O_{4+\delta}$.

All of materials still exhibit the tetragonal structure of K_2NiF_4-type materials and small amount of La_2O_3 impurity. However, the intensity of impurity peaks varies, with calcining temperatures. Therefore, the peak area ratio between the (103) peak of the K_2NiF_4-type materials and the (101) peak of La_2O_3 was calculated and the data are summarized in Table 4.1.

Table 4.1 Calculated ratio of peak area between the (101) diffraction peak of La_2O_3 and the (103) diffraction peak of $La_2Ni_{1-y}Co_yO_{4+\delta}$ (y = 0.1-0.2) materials.

Temperature (°C)	Peak area ratio between La_2O_3 and $La_2Ni_{1-y}Co_yO_{4+\delta}$	
	$La_2Ni_{0.9}Co_{0.1}O_{4+\delta}$	$La_2Ni_{0.8}Co_{0.2}O_{4+\delta}$
1000	15.60	15.00
1100	6.40	6.50
1200	3.20	3.02
1250	4.85	3.92
1300	4.75	6.49
1350	3.15	11.98

With increasing calcined temperature, the phase proportion of La_2O_3 decreases gradually and reaches the minimal portion at 1200°C. Increasing temperature from 1000°C to 1200°C, results in the high vibrational of bonding and weaker binding energy of La_2O_3 impurity [64]. When temperature was increased higher than 1200ºC, the decreasing of the main peak intensity of K_2NiF_4-type structure was observed. This can be explained by the loss of A-site (La^{3+}) ion from K_2NiF_4-type structure, resulting in the formation of metal oxide (La_2O_3) impurity and $La_2Ni_{.9}Co_{0.1}O_{4+\delta}$, the decreasing of the crystal of K_2NiF_4-type structure, resulting the La_2O_3 impurity decreased. Thus, $La_2Ni_{1-y}Co_yO_{4+\delta}$ (y = 0.1-0.2) samples calcined at 1200°C was selected for further study on the sintering effect of membranes.

4.1.3 Effect of sintering temperature

Since the La_2O_3 impurity was minimal observed on $La_2Ni_{1-y}Co_yO_{4+\delta}$ (y = 0.1-0.2) materials at calcined temperature of 1200ºC for 6 hrs. The samples were pressed into a membrane discs and sintered at 1300-1400ºC for 6 hrs. The XRD analyses for phase identification were performed and the patterns are displayed in Figure 4.3

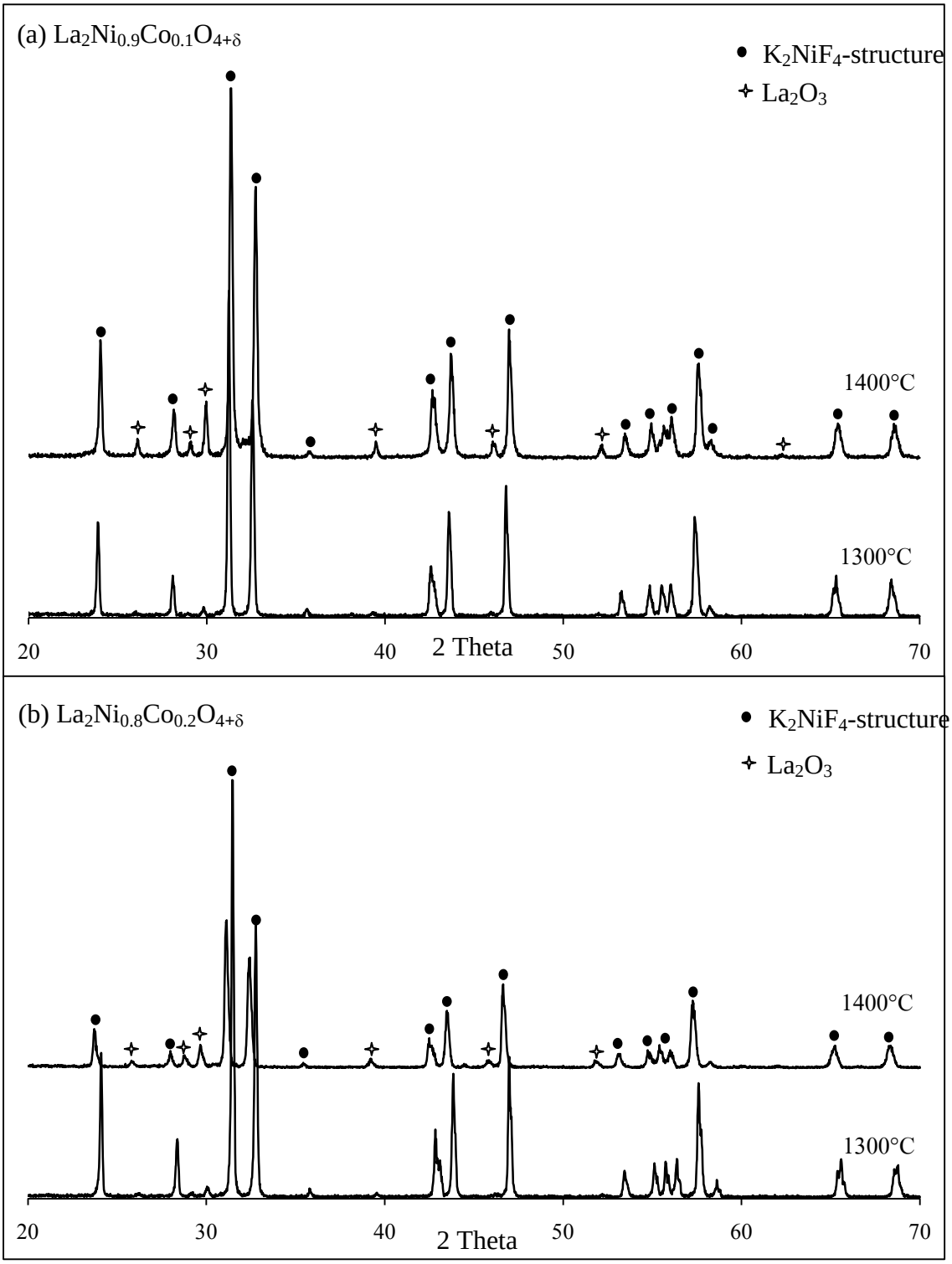

Figure 4.3 XRD patterns of sintered materials at various temperatures for 6 hrs. (a) $La_2Ni_{0.9}Co_{0.1}O_{4+\delta}$, (b) $La_2Ni_{0.8}Co_{0.2}O_{4+\delta}$.

From the result, both the samples show the optimum sintering temperature around 1300°C because the content of La_2O_3 impurity phase is minimized. The

content of impurity phase increases as the sintering temperature increases. This may be because at higher sintering temperature, melting and deformation of the disc may occur and the molecular motion takes place resulting in the weaker bond in K_2NiF_4-type structure and the distortion of structure [64]. Therefore, the optimal condition for calcining and sintering $La_2Ni_{1-y}Co_yO_{4+\delta}$ (y = 0.1-0.2) material in this research are at 1200°C and 1300ºC, respectively.

The lattice parameter and relative density of $La_2Ni_{1-y}Co_yO_{4+\delta}$ (y = 0.1-0.2) were calculated and indexed in tetragonal symmetry, as shown in Table 4.2. The increase in lattice parameter along *a*-axis as Co^{2+} content is increasingly substituted can be explained by the ionic radii of octahedrally coordinated Co^{2+} ion (0.75°A), which is longer than that of Ni^{2+} ion (0.69°A). This causes the shifting of characteristic K_2NiF_4-type structure pattern to the lower angle, as shown in Figure 4.4. In addition this substitution also causes the tilting of BO_6 octahedral layer in ABO_3 perovskite structure along the *a*-axis and exhibits a decrease along the *c*-axis [63]. The B-O-B angle which represents the tilting level of the BO_6 octahedron and the rotation of the BO_6 octahedral is illustrated in Figure 4.5 [65]. The distortion of K_2NiF_4-type structure by doping Co^{2+} in Ni^{2+} site also enhances the increment of cell volume. The increase of cell volume is effective from the increase of ion size in B-site substitution.

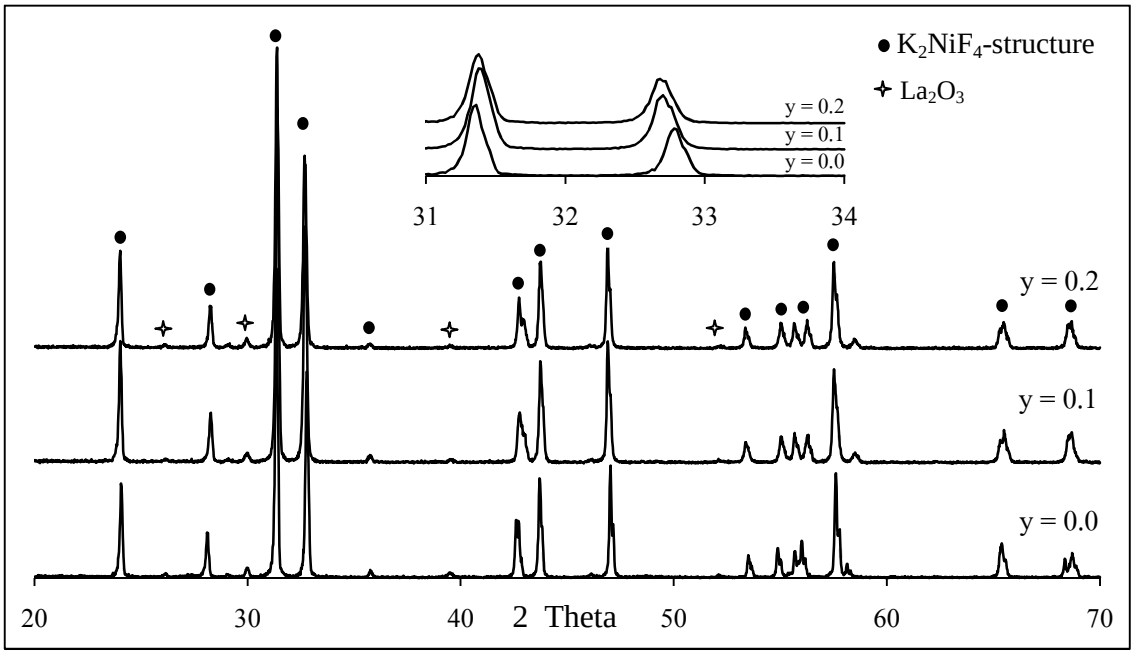

Figure 4.4 XRD patterns of $La_2Ni_{1-y}Co_yO_{4+\delta}$ (y = 0.0-0.2) discs after sintered at 1300°C for 6 hrs.

Table 4.2 The lattice parameters and cell volume of $La_2Ni_{1-y}Co_yO_{4+\delta}$ (y = 0.0-0.2).

Sample	Lattice parameter (A°)		Cell volume(A^{o3})
	a	*c*	
$La_2NiO_{4+\delta}$	3.853	12.751	189.28
$La_2Ni_{0.9}Co_{0.1}O_{4+\delta}$	3.894	12.496	189.48
$La_2Ni_{0.8}Co_{0.2}O_{4+\delta}$	3.998	12.057	192.76

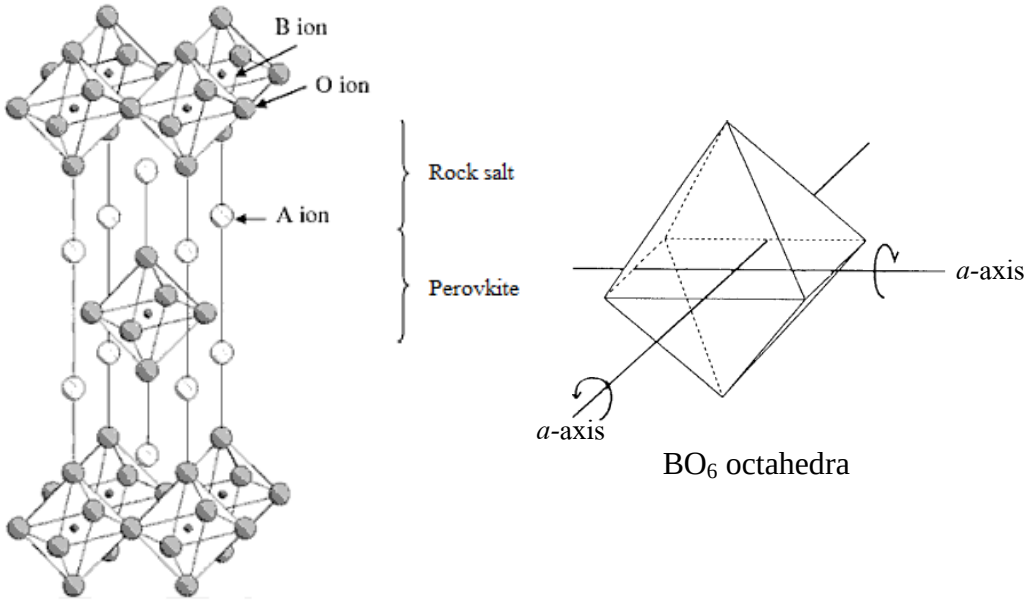

Figure 4.5 Rotation of BO_6 octahedra in perovskite layer of K_2NiF_4-type structure [66].

4.1.4 The surface morphology of $La_2Ni_{1-y}Co_yO_{4+\delta}$ (y = 0.0-0.2)

The surface morphology of $La_2Ni_{1-y}Co_yO_{4+\delta}$ (y = 0.0-0.2) sintered discs was investigated by SEM as shown in Figure 4.6. $La_2NiO_{4+\delta}$ disc exhibits porous materials with grain size around 8.89 µm. The grain size of $La_2Ni_{1-y}Co_yO_{4+\delta}$ (y = 0.0-0.2) increases when the Co content increases and the porosity is decreased. It is suggested that the increase of Co substitution promotes grain size and high relative density of materials as shown in the Table 4.3.

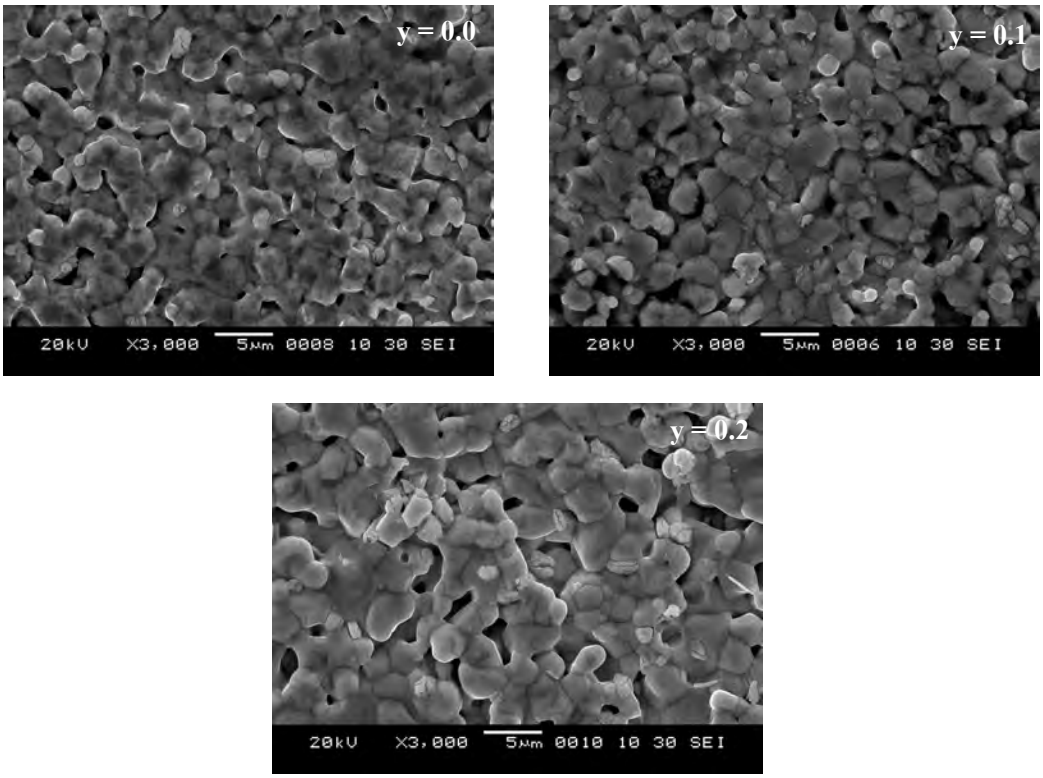

Figure 4.6 Surface morphology of $La_2Ni_{1-y}Co_yO_{4+\delta}$ (y = 0.0-0.2) discs.

Table 4.3 Grain size and relative density of $La_2Ni_{1-y}Co_yO_{4+\delta}$ (y = 0.0-0.2).

Sample	Grain size (μm)	Relative Density (%)
$La_2NiO_{4+\delta}$	8.89	86.64
$La_2Ni_{0.9}Co_{0.1}O_{4+\delta}$	9.10	86.85
$La_2Ni_{0.8}Co_{0.2}O_{4+\delta}$	10.67	87.34

4.1.5 The oxygen permeation of $La_2Ni_{1-y}Co_yO_{4+\delta}$ (y = 0.0-0.2)

The oxygen permeation property of $La_2Ni_{1-y}Co_yO_{4+\delta}$ (y = 0.0-0.2) discs were investigated as a function of temperature shown in Figure 4.7.

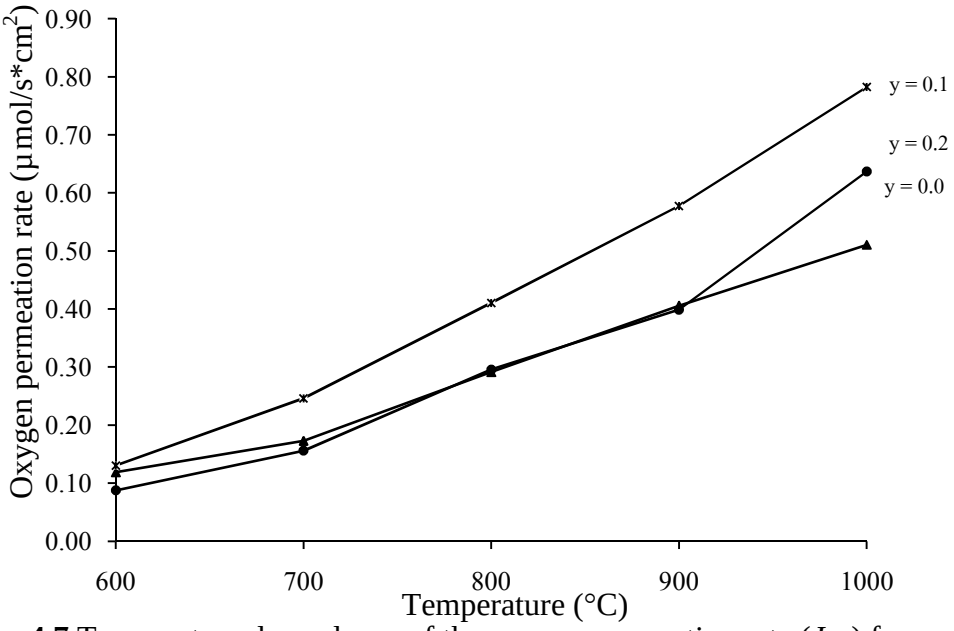

Figure 4.7 Temperature dependence of the oxygen permeation rate (Jo_2) for $La_2Ni_{1-y}Co_yO_{4+\delta}$ (y = 0.0-0.2).

The temperature dependence of the oxygen permeation rate of $La_2Ni_{1-y}Co_yO_{4+\delta}$ (y = 0.0-0.2) was increased with increasing temperature. The increasing temperature indicates the tendency of oxide ion vancancies increased. The oxygen permeation rate of $La_2Ni_{0.9}Co_{0.1}O_{4+\delta}$ is greater than of $La_2NiO_{4+\delta}$ especially at high temperatures. The highest oxygen permeation rate can be obtained from $La_2Ni_{0.9}Co_{0.1}O_{4+\delta}$ for 0.78 µmol/s.cm^2 at 1000ºC. A high oxygen permeation of $La_2Ni_{0.9}Co_{0.1}O_{4+\delta}$, can be attributed to the increase in oxygen vacancy in the perovskite layer the excess oxygen on the rock-salt layer can easily diffuse into oxygen vacancies resulting in the improvement of oxygen permeation rate [67]. For $La_2Ni_{0.8}Co_{0.2}O_{4+\delta}$ the oxygen permeation rate is less than that of $La_2Ni_{0.9}Co_{0.1}O_{4+\delta}$ because with increasing Co^{2+} ion substitution, the K_2NiF_4- type structure is more distorted due to the B-O-B angle and the rotation of the BO_6 octahedral. The distance between the defects will be longer with increasing defect concentration [64], therefore, the transport of oxygen interstitials in the rock-salt layers can't move through the oxygen vacancies in the perovskite layer. Whereas, $La_2Ni_{0.8}Co_{0.2}O_{4+\delta}$ has higher oxygen permeation than $La_2NiO_{4+\delta}$.

In oxide materials with K_2NiF_4-like lattice, diffusion of oxygen along *a-b* planes (oxygen vacancy in perovskite layer) is much faster than the diffusion in the

c direction (interstitials in rock-salt). Therefore, the highest oxygen permeation rate is related to oxygen migration, which moves through oxygen vacancies in perovskite layer and oxygen interstitials in rock-salt layer [68] showed in Figure 4.8.

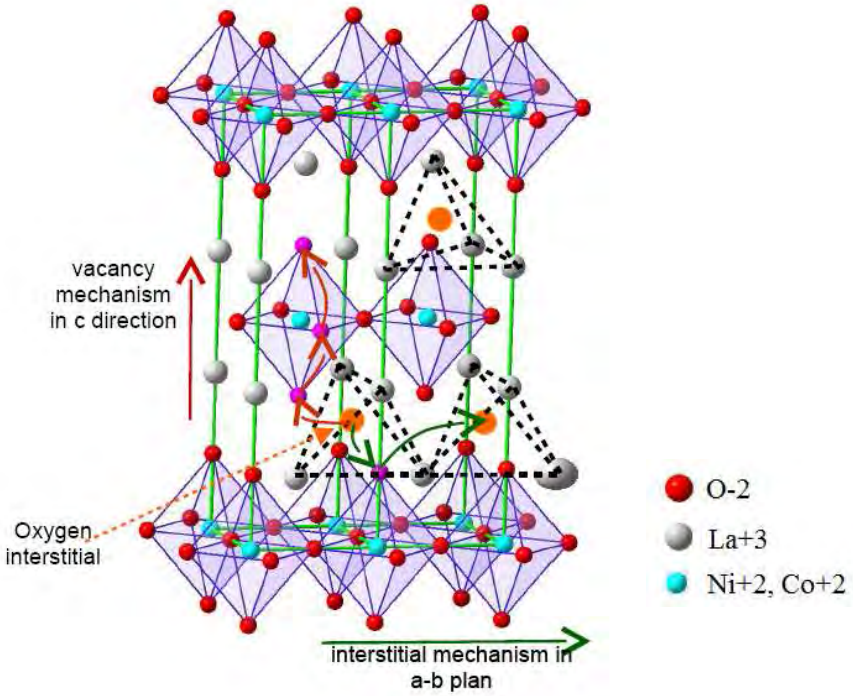

Figure 4.8 Oxygen migration path in *a-b* plane and *c* direction.

4.1.6 Electrical conductivity of $La_2Ni_{1-y}Co_yO_{4+\delta}$ (y = 0.0-0.2)

Electrical conductivity of $La_2Ni_{1-y}Co_yO_{4+\delta}$ (y = 0.0-0.2) materials were investigated as a function of temperature shown in Figure 4.9 and the data are summarized in Table 4.4.

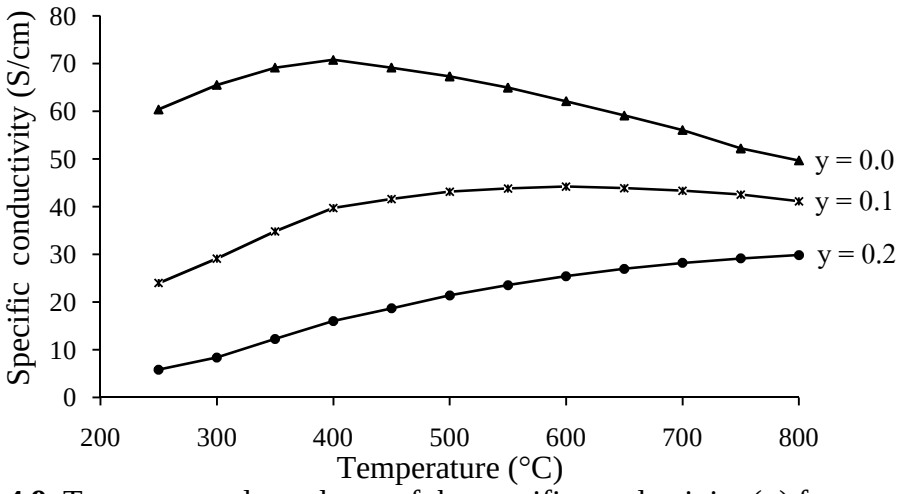

Figure 4.9 Temperature dependence of the specific conductivity (σ) for $La_2Ni_{1-y}Co_yO_{4+\delta}$ (y = 0.0-0.2).

Table 4.4 Specific conductivity of $La_2Ni_{1-y}Co_yO_{4+\delta}$ (y = 0.0-0.2).

Sample	Specific conductivity (S/cm)						
	300°C	400°C	500°C	600°C	700°C	800°C	σ_{max} (T_{max},°C)
$La_2NiO_{4+\delta}$	65.52	70.78	67.31	62.09	56.07	49.69	70.78 (400)
$La_2Ni_{0.9}Co_{0.1}O_{4+\delta}$	29.11	39.72	43.16	44.20	43.34	41.14	44.20 (600)
$La_2Ni_{0.8}Co_{0.2}O_{4+\delta}$	8.39	16.04	21.41	25.42	28.22	29.85	29.85 (800)

The temperature dependence of the electrical conductivity of $La_2NiO_{4+\delta}$ increased with measuring temperature through a maximum near 400ºC (T_{max}) and decreased with elevating temperature. At high temperature, the loss of oxygen from the lattice [69], led to the low ionic conductivity. This is because at high temperature the valency state of Ni ions at B-site in $LaNiO_3$ (ABO_3) perovskite layer is changed from Ni^{3+} to Ni^{2+} [70]. With substitution of Co^{2+} ions in Ni^{2+}-site, electrical conductivity decreases but the ionic conductivity is improved. The ionic conductivity of $La_2Ni_{1-y}Co_yO_{4+\delta}$ (y = 0.1-0.2) compounds increases with increasing temperature, suggesting the increase in oxygen vacancy. The oxygen atom loss from the lattice [69]. The substitution of Co^{2+} in Ni^{3+} site made the change in oxidation state of Co^{2+} to Co^{3+} or Co^{4+} ions which associated with the formation of the oxygen vacancies. Therefore, increasing substitution of Co^{2+} for Ni^{3+} site decreased electrical conductivity [71].

The Arrhenius plot of $La_2Ni_{1-y}Co_yO_{4+\delta}$ (y = 0.0-0.2) is given in Figure 4.10. Its linear parts can be described by the formula.

$$\sigma = (A/T) \exp(-E_a/kT) \quad (4.1)$$

and

$$\text{Slope} = -E_a/k \quad (4.2)$$

Where A is material constant including the carrier concentration term, E_a is the activation energy, k is the Boltzmann's content and T is the temperature (K). The activation energy calculated from the linear part of Arrhenius plot and the data are summarized in Table 4.5. It can be seen that the activation energy increases with the

increase in the Co^{2+} ion content. According to these results, $La_2NiO_{4+\delta}$ shows the lowest activation energy, corresponding to the highest electrical conductivity.

Activation energy is related to the different lattice structure and the energy gap of the $La_2Ni_{1-y}Co_yO_{4+\delta}$ (y = 0.0-0.2). The increasing of activity energy of doped $La_2NiO_{4+\delta}$ can be attributed to the defect structure from the tiling BO_6 octahedra prohibits the overlap of the oxygen 2p orbital with the transition metal 3d orbital. When Co^{2+} is substituted for the Ni^{3+} ions. The change carriers are transported by the M-O-M. It is well-known that increases Co^{2+} to lattice distortion and corresponding oxygen vacancies increasing result to increases of activation energy. The distortion in M-O-M bond wide energy band-width and decreases the mobility of change carrier between two metal sites. Consequently, lattice distortion increases the activation energy for change carrier hopping [72].

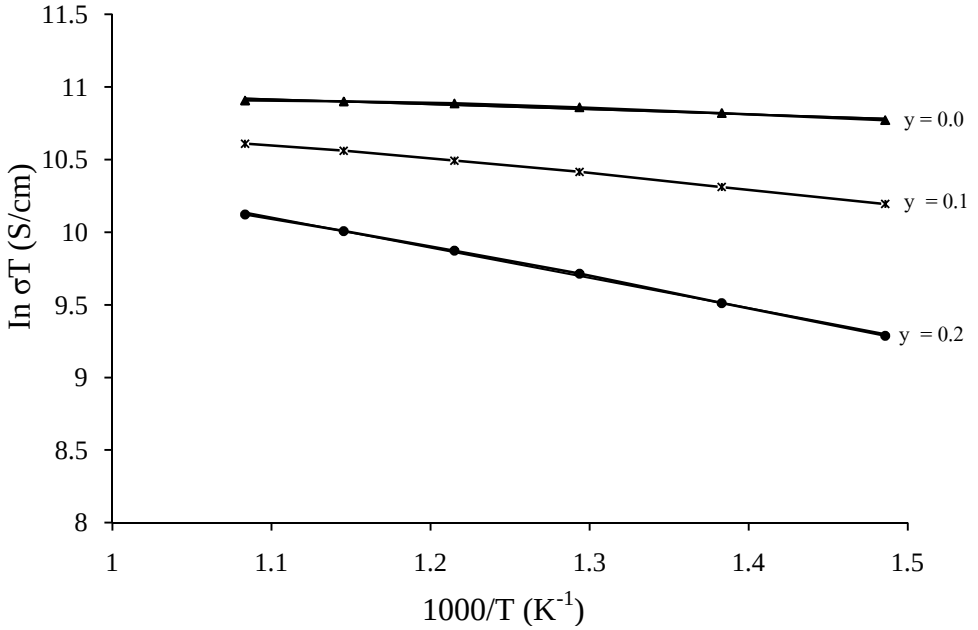

Figure 4.10 Arrhenius plot of the electrical conductivity of $La_2Ni_{1-y}Co_yO_{4+\delta}$ (y = 0.0-0.2).

Activation energies of $La_2Ni_{1-y}Co_yO_{4+\delta}$ (y = 0.0-0.1) in this research are lower than those values reported by *Nishiyama et al.* [63], as shown in Table 4.5. This may be due to the different synthesis method and the small grain sized particles of synthesized materials.

Table 4.5 Activation energy of $La_2Ni_{1-y}Co_yO_{4+\delta}$ (y = 0.0-0.2) at 400-700ºC.

Sample	E_a (kJ/mol)	
$La_2NiO_{4+\delta}$	2.86	This work
	4.36	[63]
$La_2Ni_{0.9}Co_{0.1}O_{4+\delta}$	8.66	This work
	12.82	[63]
$La_2Ni_{0.8}Co_{0.2}O_{4+\delta}$	17.32	This work

4.1.7 Thermal expansion coefficients of $La_2Ni_{1-y}Co_yO_{4+\delta}$ (y = 0.0-0.2)

Dilatometric curves for the $La_2Ni_{1-y}Co_yO_{4+\delta}$ (y = 0.0-0.2) in air are shown in Figure 4.11. The average thermal expansion coefficient (TEC) was defined as the slope of curves and be summarized in Table 4.6.

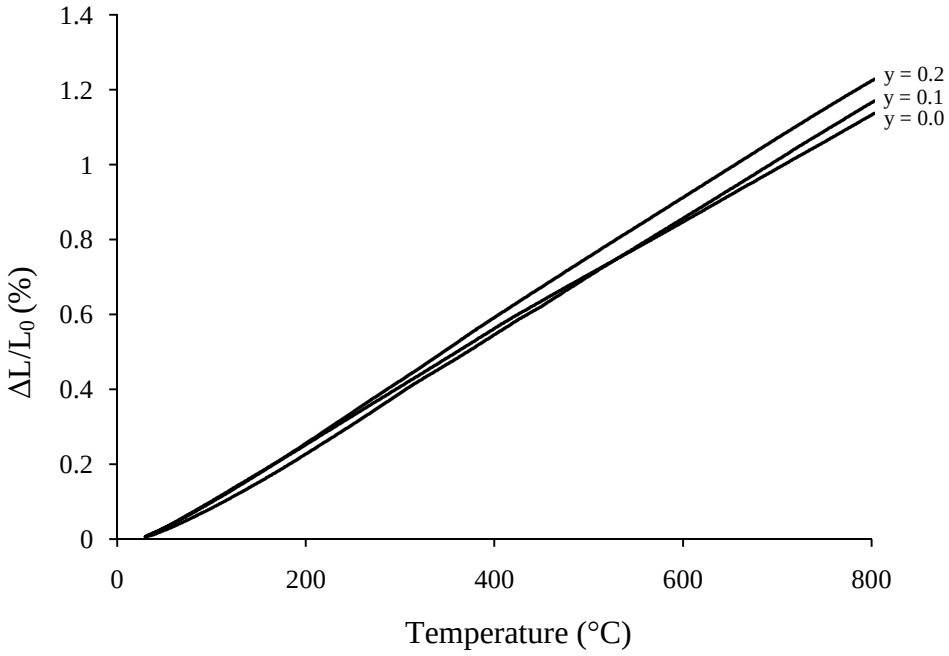

Figure 4.11 Temperature dependence of the thermal expansion for $La_2Ni_{1-y}Co_yO_{4+\delta}$ (y = 0.0-0.2)

Table 4.6 The average TEC values of $La_2Ni_{1-y}Co_yO_{4+\delta}$ (y = 0.0-0.2) at 50-800ºC.

Sample	TEC ($x10^{-6}$ $°C^{-1}$)
$La_2NiO_{4+\delta}$	14.69
$La_2Ni_{0.9}Co_{0.1}O_{4+\delta}$	15.22
$La_2Ni_{0.8}Co_{0.2}O_{4+\delta}$	15.92

Thermal expansion coefficient (TEC) slopes are linear and increased at elevated temperature, which is attributed to the loss of lattice oxygen. That is associated with the formation of the oxygen vacancies in the lattice, result to difference in the oxidation state in B-site. It is also seen that the value of TEC increases with increasing cobalt content. The change in oxidation states of cobalt ions in B-site and the consequent changes in the ionic size from Co^{2+} to Co^{3+} or Co^{4+} ions can be also accounted for the loss of lattice oxygen. That is associated with the formation of the oxygen vacancies in the lattice and the transformation of the changes in valency state in B-site, which can be accomplished by Eq 4.3.

$$O_o = V_o^{\cdot\cdot} + \tfrac{1}{2} O_2 + 2e^- \qquad (4.3)$$

Where O_o = oxygen ion

$V_o^{\cdot\cdot}$ = oxygen vacancies

The formation of oxygen vacancies ($V_o^{\cdot\cdot}$) can let to the lattice expansion to occur due to a weak bonding of metal-oxygen-metal and a change in the oxidation state of the B-site cations by the reduction of Ni^{3+} to Ni^{2+} ion and the oxidation of Co^{2+} to Co^{3+} or Co^{4+} state. The different valence charges of B-site are also associated with the difference of the ionic radius of M-O-M bond according to the size BO_6 octahedral and the defect structure from the tilting BO_6 octahedral. Thus, the substitution of Co in Ni increases the TEC [64].

4.2 Preparation and properties of $La_{2-x}Ca_xNi_{0.9}Co_{0.1}O_{4+\delta}$ (x = 0.0-1.0)

Since the effect of Co^{2+} substitution in Ni^{2+}-site on the oxygen permeation rate of $La_2NiO_{4+\delta}$, results the highest oxygen permeation rate of $La_2Ni_{0.9}Co_{0.1}O_{4+\delta}$, the substitution of Ca^{2+} in La^{3+}-site on the K_2NiF_4-type structure and electrical conductivity is further investigated.

4.2.1 Synthesis of $La_{2-x}Ca_xNi_{0.9}Co_{0.1}O_{4+\delta}$ (x = 0.0-1.0)

$La_{2-x}Ca_xNi_{0.9}Co_{0.1}O_{4+\delta}$ (x = 0.0-1.0) powders were prepared and calcined at 1200ºC for 6 hrs. The XRD patterns are illustrated in Figure 4.12.

$La_{2-x}Ca_xNi_{0.9}Co_{0.1}O_{4+\delta}$ (x = 0.0-0.3) shows the characteristic diffraction pattern of tetragonal K_2NiF_4 type structure whereas small peaks of La_2O_3 impurity phase are also observed. As the material composition of $x \geq 0.5$, the tetragonal K_2NiF_4-type structure and small amount of CaO impurity phase (PDF No. 75-0264) are detected.

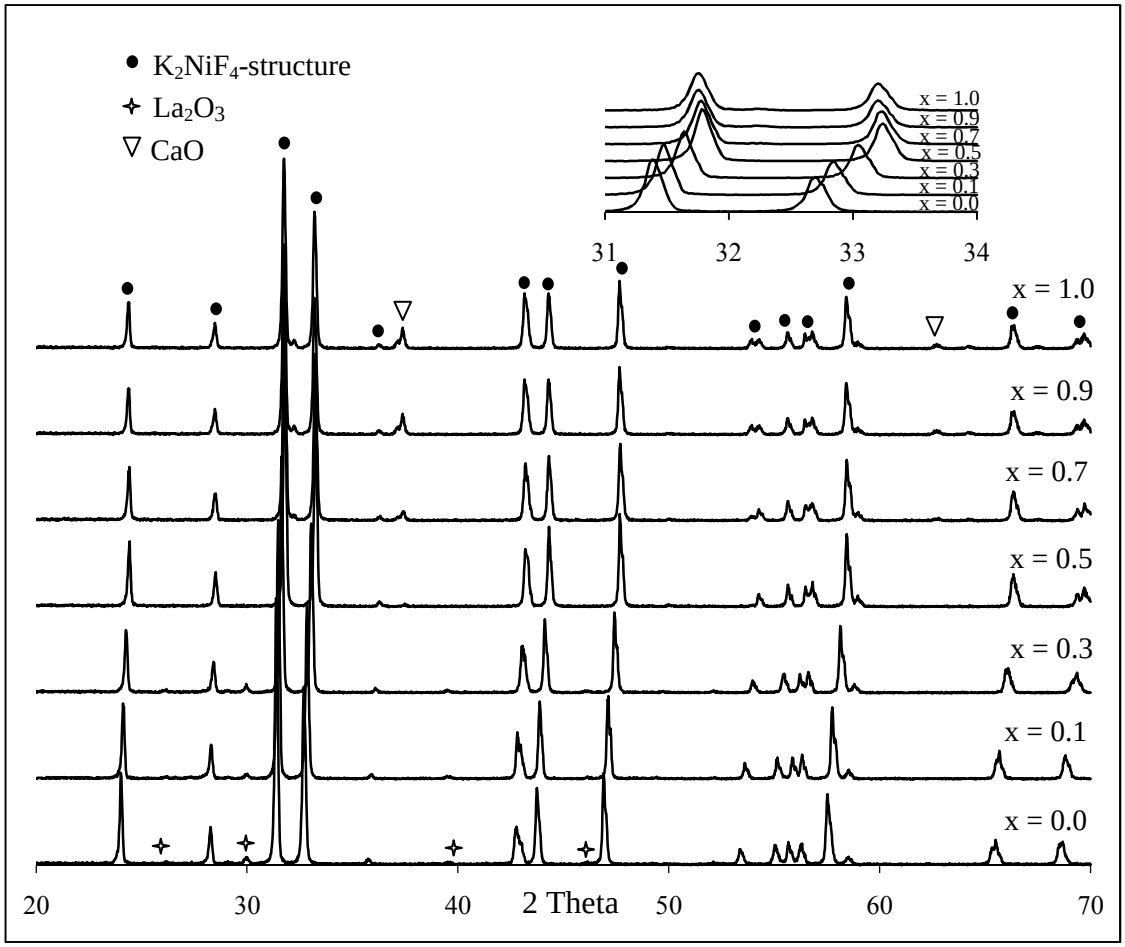

Figure 4.12 XRD patterns of $La_{2-x}Ca_xNi_{0.9}Co_{0.1}O_{4+\delta}$ (x = 0.0-1.0) powder after calcined at 1200ºC for 6 hrs.

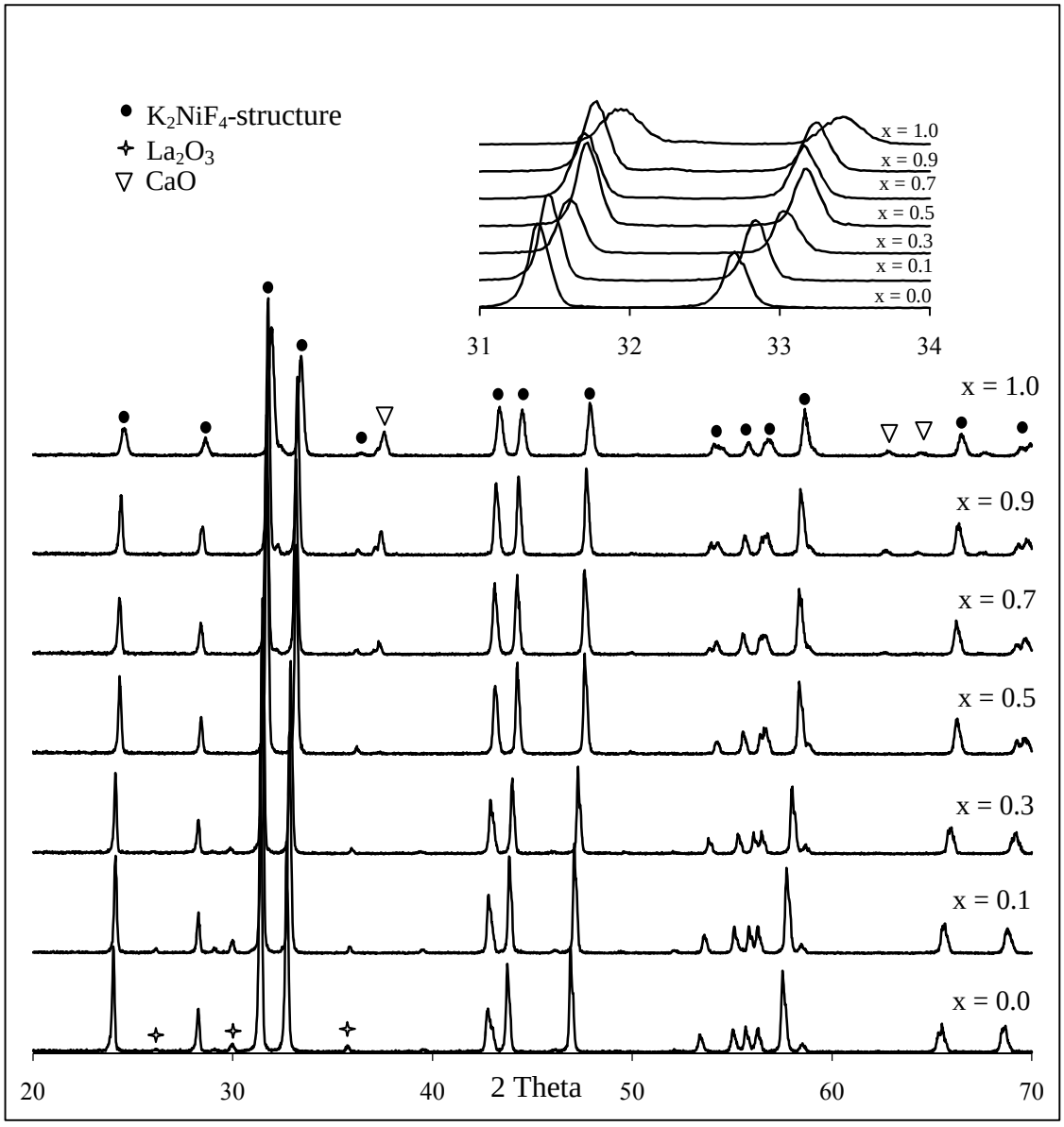

Figure 4.13 XRD patterns of $La_{2-x}Ca_xNi_{0.9}Co_{0.1}O_{4+\delta}$ (x = 0.0-1.0) discs after sintered at 1300ºC for 6 hrs.

Figure 4.13 illustrates the XRD patterns of samples sintered at 1300°C for 6 hrs. All of $La_{2-x}Ca_xNi_{0.9}Co_{0.1}O_{4+\delta}$ samples distinctively show the K_2NiF_4–type with tetragonal structure. At x = 0.0-0.3, not only diffraction lines of K_2NiF_4-type, but also the secondary phase of La_2O_3 are observed. At x equals 0.5, only single phase K_2NiF_4-type structure is observed. At x = 0.7-1.0, it is found that secondary phase as CaO (2θ = 37.5°, PDF No. 75-0264) is observed and the amount of the CaO phase increases with the increasing amount of Ca^{2+} doped at La^{3+} (A-site). The XRD patterns of Ca^{2+} doped materials (2θ ≈ 31.7° and 33.2°) are slightly shifted to the

higher angle compared to the undoped one and the relationship of lattice parameter and cell volume are summarized as shown in Table 4.7. The lattice parameters and cell volume decrease with the increase of Ca^{2+} ions in A-site of K_2NiF_4 (A_2BO_4)-type structure. Two plausible explanation can be accounted. Firstly, the ionic radii of Ca^{2+} ion is smaller than that of La^{3+} thus the substitution of Ca^{2+} ion in the A-site will affect the A-O bond in the rock salt layer causing the shrinkage of A-O bond. And, secondly, the substitution of Ca^{2+} ions for La^{3+} ion in the A-site will induce the oxidation state of B-site ion in the ABO_3 layer from Ni^{3+} to Ni^{4+} or Co^{2+} to Co^{3+} or Co^{4+}. Therefore the bond distance of B-O-B becomes stronger and shorter [73] and when x = 0.9, 1.0 leading to the expansion of *c*-axis because of transition metal ions with different sizes at A-site can cause simple distortion of the rock-salt layer.

Table 4.7 The lattice parameters and cell volume of $La_{2-x}Ca_xNi_{0.9}Co_{0.1}O_{4+\delta}$ (x = 0.0-1.0).

Ration	Lattice parameter (A°)		Cell volume (A^{o3})
	a	*c*	
x = 0.0	3.894	12.496	189
x = 0.1	3.862	12.242	182
x = 0.3	3.859	12.181	181
x = 0.5	3.841	12.120	178
x = 0.7	3.832	12.114	177
x = 0.9	3.819	12.129	176
x = 1.0	3.793	12.142	174

4.2.2 The surface morphology of $La_{2-x}Ca_xNi_{0.9}Co_{0.1}O_{4+\delta}$ (x = 0.0-1.0)

The surface morphology of $La_{2-x}Ca_xNi_{0.9}Co_{0.1}O_{4+\delta}$ (x = 0.0-1.0) sintered discs were investigated by SEM as shown in Figure 4.14.

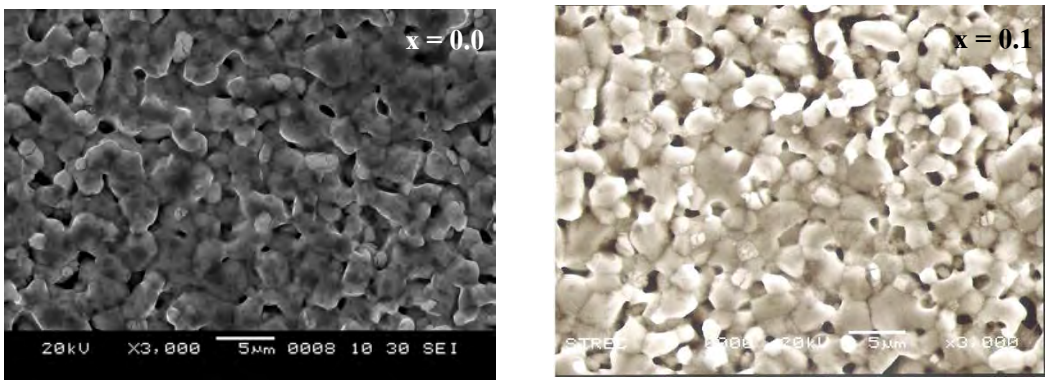

Figure 4.14 Surface morphology of $La_{2-x}Ca_xNi_{0.9}Co_{0.1}O_{4+\delta}$ (x = 0.0-1.0) discs.

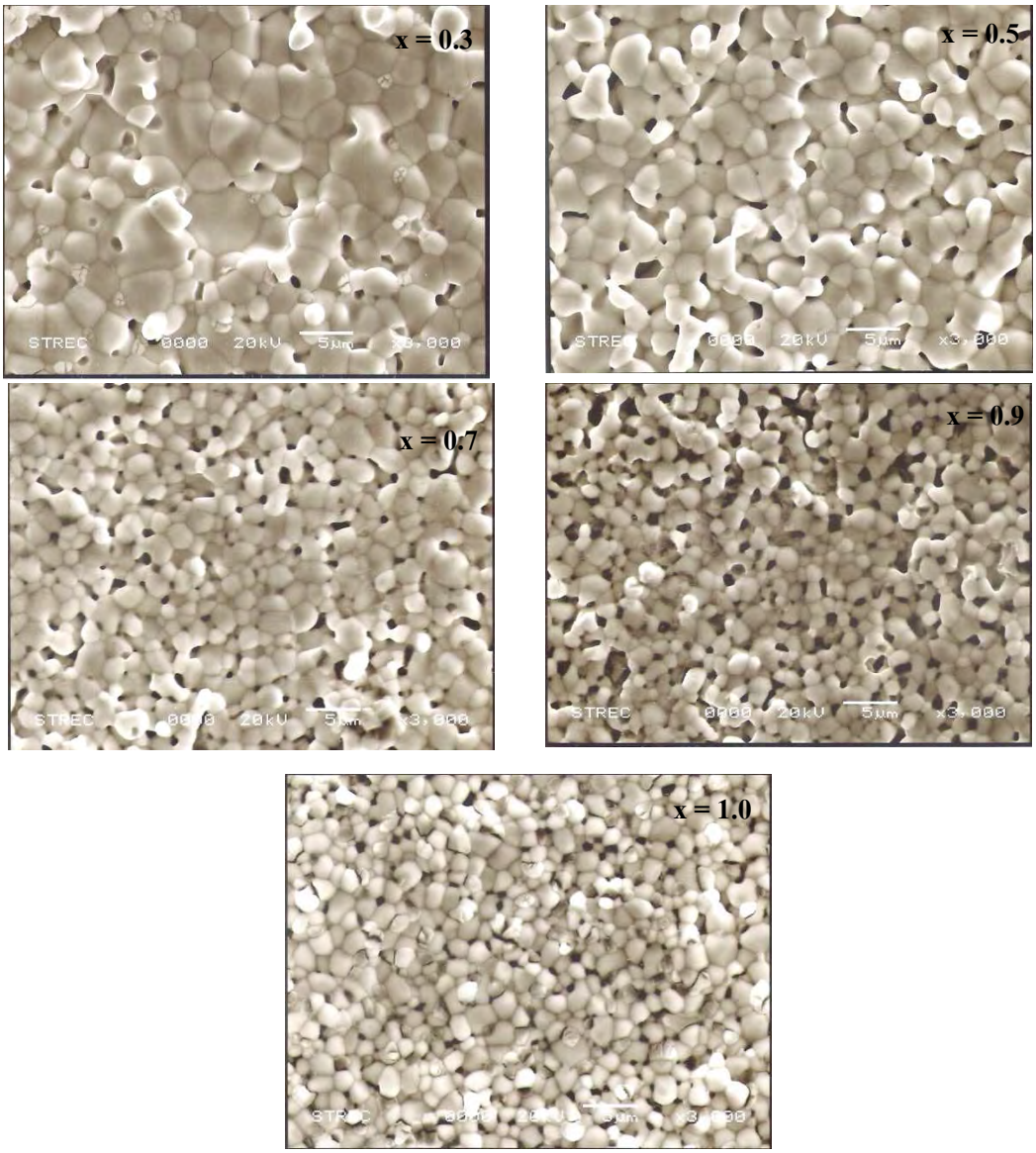

Figure 4.14 Surface morphology of $La_{2-x}Ca_xNi_{0.9}Co_{0.1}O_{4+\delta}$ (x = 0.0-1.0) discs.

$La_{2-x}Ca_xNi_{0.9}Co_{0.1}O_{4+\delta}$ (x = 0.0-1.0) discs exhibit porous surface materials. The grain size of samples tends to decreases with increasing the content of Ca^{2+} ion doping since the ionic size of Ca^{2+} ion (1.14ºA) is smaller than that of La^{3+} ion (1.17ºA), the bond distance in the structure becomes shorter leading to the small particles, which relates to the density of materials. The smaller the grain size are, the higher the relative density of materials obtained. Conclusively, the increase in Ca^{2+} ion substitution promotes the smaller grain size and high relative density of materials as shown in the Table 4.8.

Table 4.8 Grains size and relative density of $La_{2-x}Ca_xNi_{0.9}Co_{0.1}O_{4+\delta}$ (x = 0.0-1.0).

Ratio	Grain size (µm)	Relative density (%)
x = 0.0	9.1	86.85
x = 0.1	10.7	93.72
x = 0.3	8.0	95.96
x = 0.5	7.6	97.86
x = 0.7	6.1	97.97
x = 0.9	5.8	98.11
x = 1.0	5.5	98.19

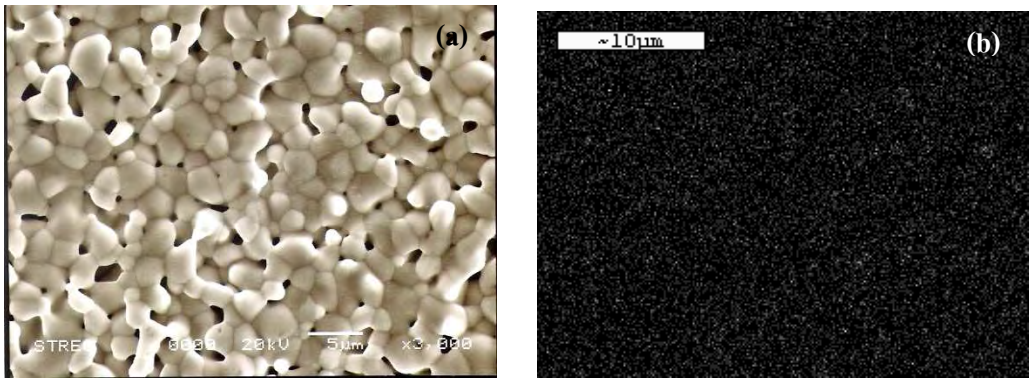

Figure 4.15 Surface morphology (a) and Ca-mapping (b) of $La_{1.5}Ca_{0.5}Ni_{0.9}Co_{0.1}O_{4+\delta}$ discs.

Figure 4.15(b) illustrates the homogeneous distribution of Ca^{2+} ion on $La_{1.5}Ca_{0.5}Ni_{0.9}Co_{0.1}O_{4+\delta}$ material. This result is in agreement with the XRD analysis, which indicates only $La_{1.5}Ca_{0.5}Ni_{0.9}Co_{0.1}O_{4+\delta}$ is a pure single phase material.

4.2.3 Electrical conductivity of $La_{2-x}Ca_xNi_{0.9}Co_{0.1}O_{4+\delta}$ (x = 0.0-1.0)

Electrical conductivity of $La_{2-x}Ca_xNi_{0.9}Co_{0.1}O_{4+\delta}$ (x = 0.0-1.0) materials were investigated as a function of temperature shown in Figure 4.16 and the data are summarized in Table 4.9.

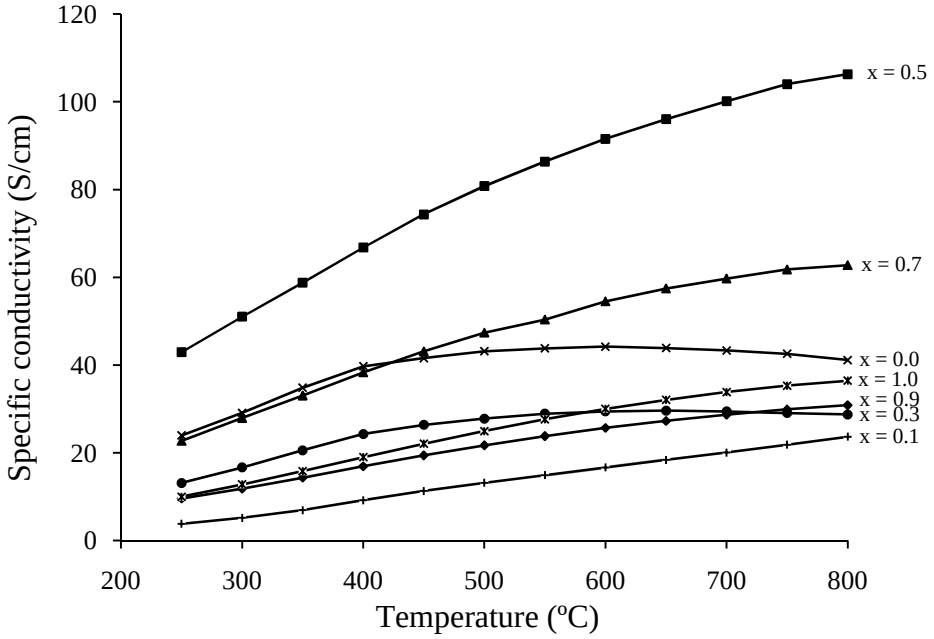

Figure 4.16 Temperature dependence of the specific conductivity (σ) for $La_{2-x}Ca_xNi_{0.9}Co_{0.1}O_{4+\delta}$ (x = 0.0-1.0).

The temperature dependence on the electrical conductivity of $La_2Ni_{0.9}Co_{0.1}O_{4+\delta}$ increases with increasing the measuring temperature and slightly decrease at elevating temperature. At high temperature, electrons move no direction causing the high resistance and the loss in electrical conductivity. In addition, it is also attributed to the loss of oxygen from the lattice to the formation of oxygen vacancies [74]. When Ca^{2+} ions substitutes into the La^{3+}-site, the conductivity of $La_{2-x}Ca_xNi_{0.9}Co_{0.1}O_{4+\delta}$ materials increase with the increasing of temperature. It is suggested that the partial replacement of La^{3+} ion by Ca^{2+} ion leads to the direct increase in electrical hole which plays an important role in electronic conductivity and the formation of oxygen vacancies. While the change in oxidation state of Ni^{2+} and Co^{2+} plays a minor rule in oxide ion conductivity [75]. The maximum electrical conductivity in the research is obtained from $La_{1.5}Ca_{0.5}Ni_{0.9}Co_{0.1}O_{4+\delta}$ sample. The individual defect equilibrium can be expressed as following Eq. 4.5.

$$[Ca'_{La}] = [Ni_{Ni}^{\bullet}] + [Co_{Co}^{\bullet}] + 2[V_o^{\bullet\bullet}] \quad (4.5)$$

Where $[Ni_{Ni}^{\bullet}]$ and $[Co_{Co}^{\bullet}]$ is electron hole

$[V_o^{\bullet\bullet}]$ is oxygen vacancies

The electrical conductivities of samples with x < 0.5 are lower than the undoped samples. It may be due to the existence of La_2O_3 impurity phase, which is similar to the samples with the Ca^{2+} ion substitution are greater than x > 0.5, where CaO is recognized as the impurity phase from XRD analysis. In addition, the decreases of electrical conductivity when x < 0.5 and x > 0.5 may associate with the distorted structure of K_2NiF_4-type from the B-O-B angle and the tilting of the BO_6 octahedral in perovskite layer. That prohibits the overlap of the oxygen 2p orbital with the transition metal 3d orbital.

Table 4.9 Specific conductivity of $La_{2-x}Ca_xNi_{0.9}Co_{0.1}O_{4+\delta}$ (x = 0.0-1.0).

Sample	**Specific conductivity (S/cm)**						
	300°C	400°C	500°C	600°C	700°C	800°C	σ_{max} (T,°C)
$La_2Ni_{0.9}Co_{0.1}O_{4+\delta}$	29.11	39.72	43.16	44.20	43.34	41.13	44.20 (600)
$La_{1.9}Ca_{0.1}Ni_{0.9}Co_{0.1}O_{4+\delta}$	16.67	24.29	27.81	29.45	29.45	28.74	29.82 (650)
$La_{1.7}Ca_{0.3}Ni_{0.9}Co_{0.1}O_{4+\delta}$	5.18	9.21	13.56	16.67	20.07	23.67	23.67 (800)
$La_{1.5}Ca_{0.5}Ni_{0.9}Co_{0.1}O_{4+\delta}$	51.01	66.78	80.79	91.54	100.1	106.3	106.3 (800)
$La_{1.3}Ca_{0.7}Ni_{0.9}Co_{0.1}O_{4+\delta}$	27.95	38.35	47.40	54.52	59.72	62.79	62.79 (800)
$La_{1.1}Ca_{0.9}Ni_{0.9}Co_{0.1}O_{4+\delta}$	11.84	16.94	21.72	25.71	28.72	30.89	30.89 (800)
$LaCaNi_{0.9}Co_{0.1}O_{4+\delta}$	12.82	19.00	24.94	30.02	33.86	36.42	36.42 (800)

The Arrhenius plot of $La_{2-x}Ca_xNi_{0.9}Co_{0.1}O_{4+\delta}$ (x = 0.0-1.0) is given in Figure 4.17 and the activation energy calculated from the liner part of Arrhenius plot are summarized in Table 4.10. It can be seen that the activation energy increases with the increase in the Ca^{2+} ion content. Increasing distortion in the structure produces the higher activation energy.

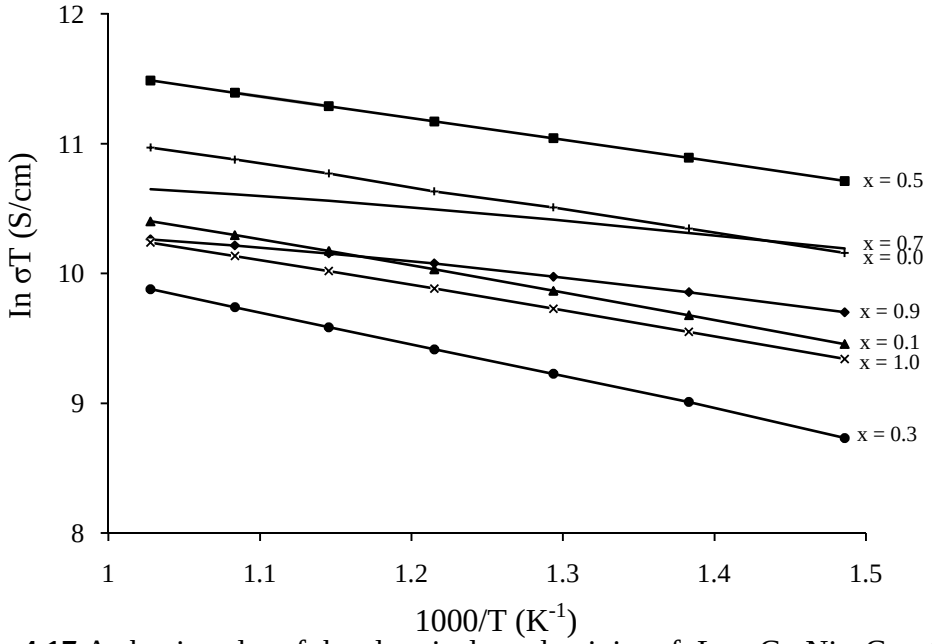

Figure 4.17 Arrhenius plot of the electrical conductivity of $La_{2-x}Ca_xNi_{0.9}Co_{0.1}O_{4+\delta}$ (x = 0.0-1.0).

Table 4.10 Activation energy of $La_{2-x}Ca_xNi_{0.9}Co_{0.1}O_{4+\delta}$ (x = 0.0-1.0) at 400-700ºC.

Sample	E_a **(kJ/mol)**
x = 0.0	8.66
x = 0.1	10.21
x = 0.3	20.63
x = 0.5	13.98
x = 0.7	14.74
x = 0.9	16.28
x = 1.0	17.21

4.2.4 The oxygen permeation of $La_{2-x}Ca_xNi_{0.9}Co_{0.1}O_{4+\delta}$ (x = 0, 0.5)

Since the substitution of $La_{1.5}Ca_{0.5}Ni_{0.9}Co_{0.1}O_{4+\delta}$ gave the pure single phase structure and the highest electrical conductivity, the oxygen permeation of the material disc was investigated as a function of temperature shown in Figure 4.18, compared with the undoped materials.

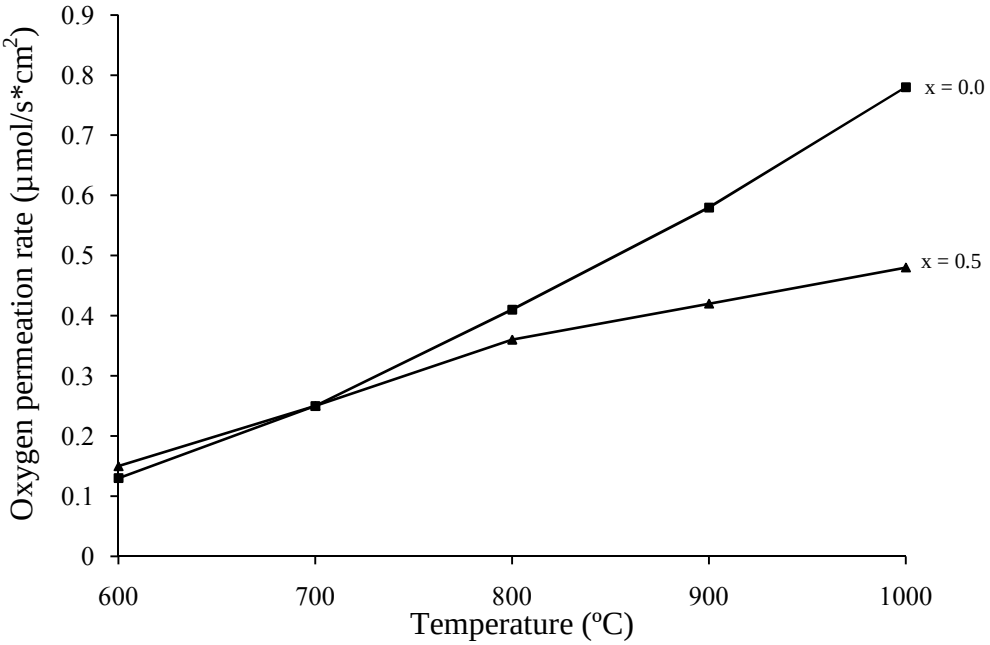

Figure 4.18 Temperature dependence of the oxygen permeation rate (Jo_2) for $La_{2-x}Ca_xNi_{0.9}Co_{0.1}O_{4+\delta}$ (x = 0, 0.5).

The temperature dependence of the oxygen permeation rate of $La_{2-x}Ca_xNi_{0.9}Co_{0.1}O_{4+\delta}$ (x = 0, 0.5) materials were increased with increasing temperature, indicating the tendency of oxygen vacancies increases with increasing temperature. When trivalent La^{3+} ion is substituted by divalent ions *e.q.* Ca^{2+} ion, the oxygen permeation rates of both samples at 600-800ºC are not different, suggesting $La_2Ni_{0.9}Co_{0.1}O_{4+\delta}$ and $La_{1.5}Ca_{0.5}Ni_{0.9}Co_{0.1}O_{4+\delta}$ are good as materials for intermediate-temperature solid oxide fuel cell (IT-SOFC).

At temperature of 800-1000ºC, the oxygen permeation rate of $La_{1.5}Ca_{0.5}Ni_{0.9}Co_{0.1}O_{4+\delta}$ is lower than the oxygen permeation rate of $La_2Ni_{0.9}Co_{0.1}O_{4+\delta}$, suggesting the effect of Ca^{2+} ion substituted in La^{3+}-site. Since the oxidation state of Ca^{2+} ion is less than the La^{3+} ion, the change in oxidation state of cation in A-site position induces the change in oxidation state of B-site from Ni^{3+} to Ni^{4+} and Co^{2+} to Co^{3+} or Co^{4+}. Therefore the bond energy of B-O in B-O plane becomes stronger and the bond distance becomes shorter in ABO_3 structure and the A-O bond distance in rock-salt layer will become higher in bond-strength. The increase in bonding energy inhibits the migration of oxygen in structure. This effect will decrease the free space of excess oxygen from the interstitial sites in the rock-salt layer, to migrate to the oxygen vacancies in the perovskite layer [87,91]. Therefore, $La_2Ni_{0.9}Co_{0.1}O_{4+\delta}$ is more

appropriate material than $La_{1.5}Ca_{0.5}Ni_{0.9}Co_{0.1}O_{4+\delta}$ for using at high temperature solid oxide fuel cell (>800ºC)

4.2.5 Thermal expansion coefficients of $La_{2-x}Ca_xNi_{0.9}Co_{0.1}O_{4+\delta}$ (x = 0, 0.5)

Dilatometric curves for the $La_{2-x}Ca_xNi_{0.9}Co_{0.1}O_{4+\delta}$ (x = 0, 0.5) in air are shown in Figure 4.19. The average thermal expansion coefficient (TEC) was defined as the slope of curves and be summarized in Table 4.11.

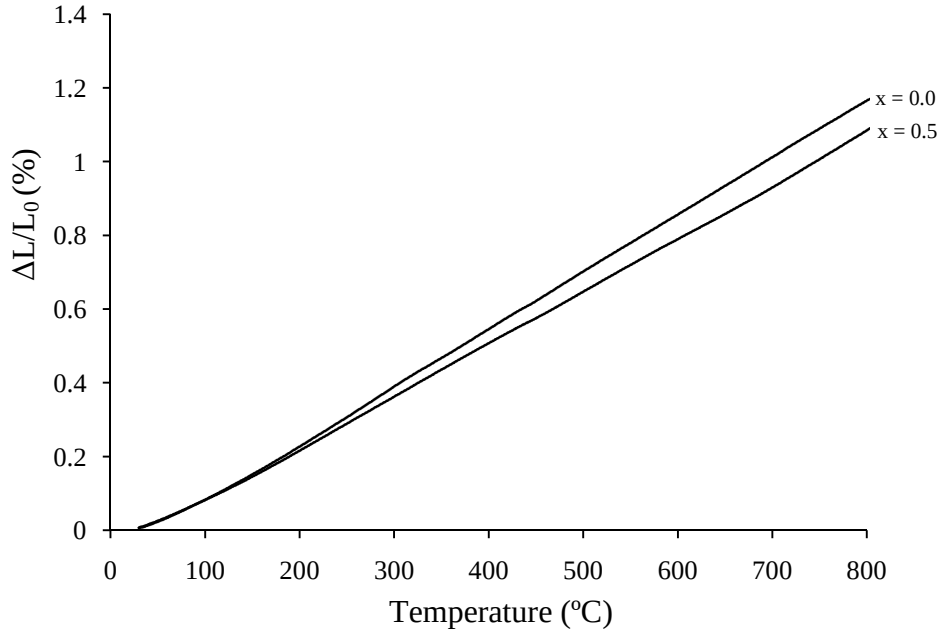

Figure 4.19 Temperature dependence of the thermal expansion for $La_{2-x}Ca_xNi_{0.9}Co_{0.1}O_{4+\delta}$ (x = 0, 0.5).

Table 4.11 The average TEC values of $La_{2-x}Ca_xNi_{0.9}Co_{0.1}O_{4+\delta}$ (x = 0, 0.5) at 50-800ºC.

Sample	TEC ($x10^{-6}$ °C^{-1})
$La_2Ni_{0.9}Co_{0.1}O_{4+\delta}$	15.22
$La_{1.5}Ca_{0.5}Ni_{0.9}Co_{0.1}O_{4+\delta}$	13.82

Thermal expansion coefficient (TEC) slopes are linear and increased at elevated temperature, which is attributed to the loss of lattice oxygen. That is associated with the formation of the oxygen vacancies in the lattice. The substitution of a Ca^{2+} ion for La^{3+}-site associates with the decreasing of ionic radius at the A-site, the A-O bond in rock-salt layer, and the B-O-B bond in perovskite layer and the size

BO_6 octahedral structure, which suggests a lower concentration of oxygen vacancy formation [77]. Thus, the substitution of Ca^{2+} ion in La^{3+}-site decreases the TEC.

4.3 Preparation and properties of $La_{1.5}Ca_{0.5}Ni_{0.9}Co_{0.1}(Ga, Ti)_zO_{4+\delta}$ (z = 0.00-0.1, 0.2)

Since the effect of Ca^{2+} substitution in La^{3+}-site on electrical conductivity of $La_2Ni_{0.9}Co_{0.1}O_{4+\delta}$, results in the higher electrical conductivity of $La_{1.5}Ca_{0.5}Ni_{0.9}Co_{0.1}O_{4+\delta}$, the addition of Ga^{3+} and Ti^{4+} ions on the K_2NiF_4-type structure and the oxygen permeation rate is further investigated.

4.3.1 Synthesis and properties of $La_{1.5}Ca_{0.5}Ni_{0.9}Co_{0.1}Ga_zO_{4+\delta}$ (z = 0.00-0.1, 0.2)

4.3.1.1 Synthesis of $La_{1.5}Ca_{0.5}Ni_{0.9}Co_{0.1}Ga_zO_{4+\delta}$ (z = 0.00-0.1, 0.2)

$La_{1.5}Ca_{0.5}Ni_{0.9}Co_{0.1}Ga_zO_{4+\delta}$ (z = 0.00-0.1, 0.2) powders were prepared and calcined at 1200ºC for 6 hrs. The XRD patterns are illustrated in Figure 4.20. $La_{1.5}Ca_{0.5}Ni_{0.9}Co_{0.1}Ga_zO_{4+\delta}$ (z = 0.00-0.1, 0.2) shows the characteristic pattern of single-phase tetragonal K_2NiF_4-type structure.

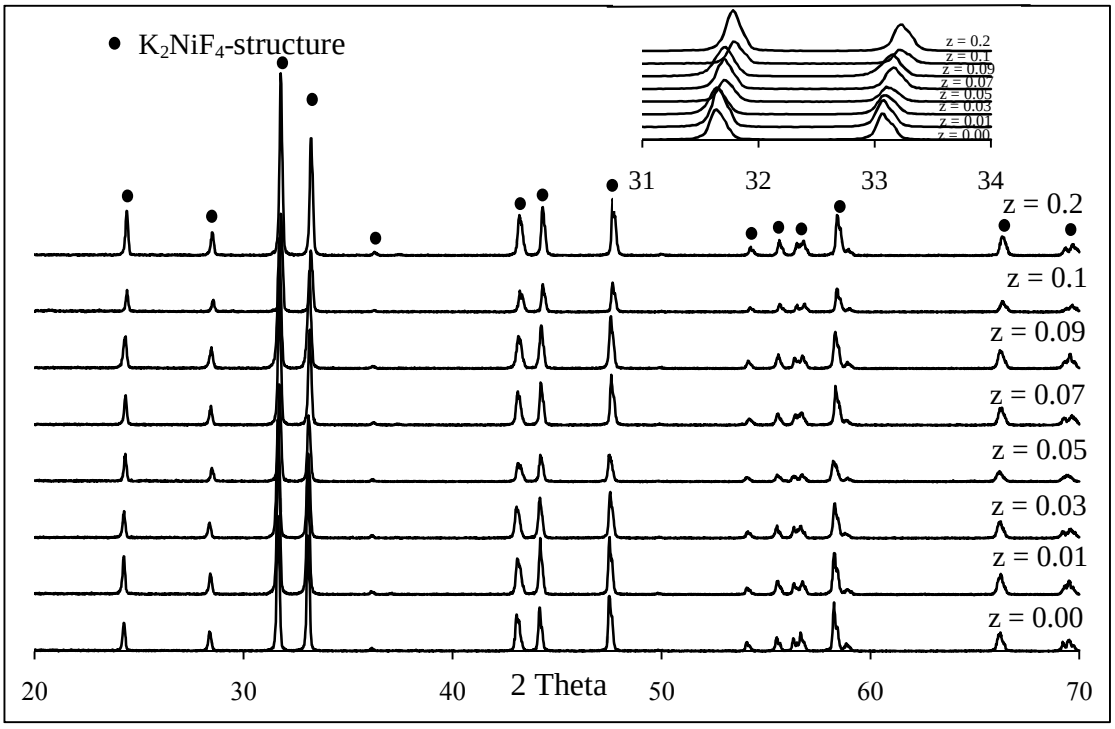

Figure 4.20 XRD patterns of $La_{1.5}Ca_{0.5}Ni_{0.9}Co_{0.1}Ga_zO_{4+\delta}$ (z = 0.00-0.1, 0.2) powder after calcined at 1200°C for 6 hrs.

Figure 4.21 illustrates the XRD patterns of samples sintered at1300ºC for 6 hrs. All of $La_{1.5}Ca_{0.5}Ni_{0.9}Co_{0.1}Ga_zO_{4+\delta}$ samples distinctively show the single-phase K_2NiF_4-type with tetragonal structure and no peak from a secondary phase is observed. The XRD patterns of Ga^{3+} doped materials ($2\theta \approx 31.7^o$ and 33.2^o) are slightly shifted to the lower angle compared to the undoped one and the relationship of lattice parameter and cell volume are summarized as shown in Table 4.12. Since the ionic size of Ga^{3+} ion is small (0.68Aº), it can be inserted into the interstitial position of the rock-salt and the perovskite layers leading to the expansion of A-O bond along the *c*-axis[13] and the cell volume.

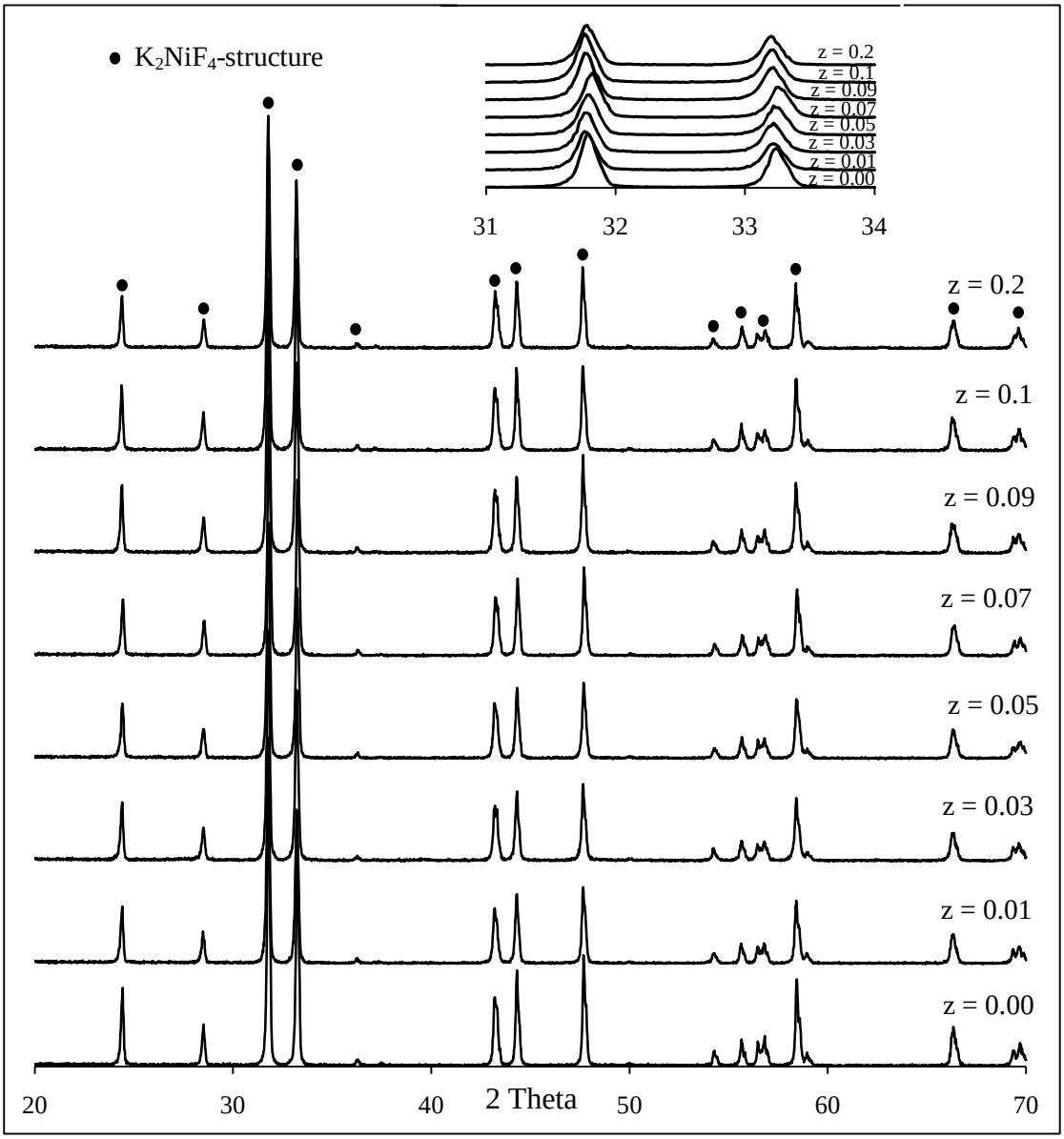

Figure 4.21 XRD patterns of $La_{1.5}Ca_{0.5}Ni_{0.9}Co_{0.1}Ga_zO_{4+\delta}$ (z = 0.00-0.1, 0.2) discs after sintered at 1300°C for 6 hrs.

Table 4.12 The lattice parameters and cell volume of $La_{1.5}Ca_{0.5}Ni_{0.9}Co_{0.1}Ga_zO_{4+\delta}$ (z = 0.00-0.1, 0.2).

Ration	Lattice parameter (A°)		Cell volume (A^{o3})
	a	*c*	
z = 0.00	3.841	12.120	178
z = 0.01	3.807	12.599	183
z = 0.03	3.810	12.548	182
z = 0.05	3.807	12.586	182
z = 0.07	3.801	12.635	182
z = 0.09	3.810	12.568	182
z = 0.1	3.811	12.564	182
z = 0.2	3.813	12.514	182

4.3.1.2 The surface morphology of $La_{1.5}Ca_{0.5}Ni_{0.9}Co_{0.1}Ga_zO_{4+\delta}$ (z = 0.00-0.1, 0.2)

The surface morphology of $La_{1.5}Ca_{0.5}Ni_{0.9}Co_{0.1}Ga_zO_{4+\delta}$ (z = 0.00-0.1, 0.2) sintered discs were investigated by SEM as shown in Figure 4.22. All discs exhibits porous surface materials. The grain size of samples tends to increase with increasing the content of Ga^{3+} ion doping. Then the relative density is lower than the undoped material. In addition, there is no relationship between relative density and the content of Ga^{3+} ion.

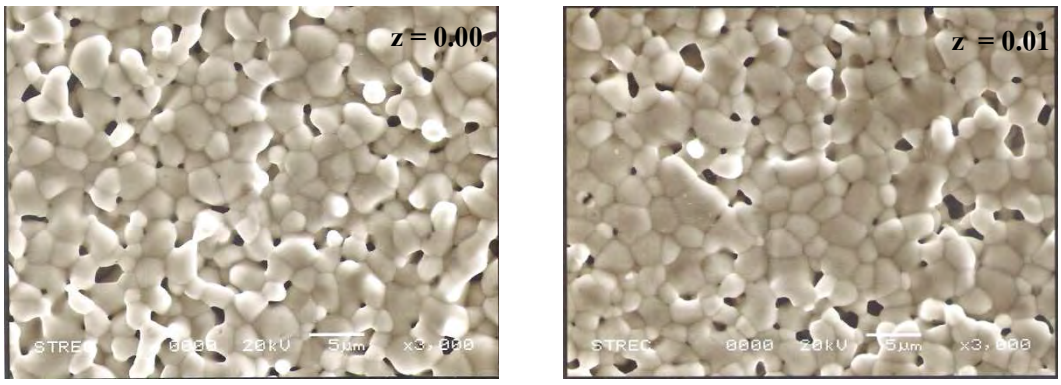

Figure 4.22 Surface morphology of $La_{1.5}Ca_{0.5}Ni_{0.9}Co_{0.1}Ga_zO_{4+\delta}$ (z = 0.00-0.1, 0.2) discs.

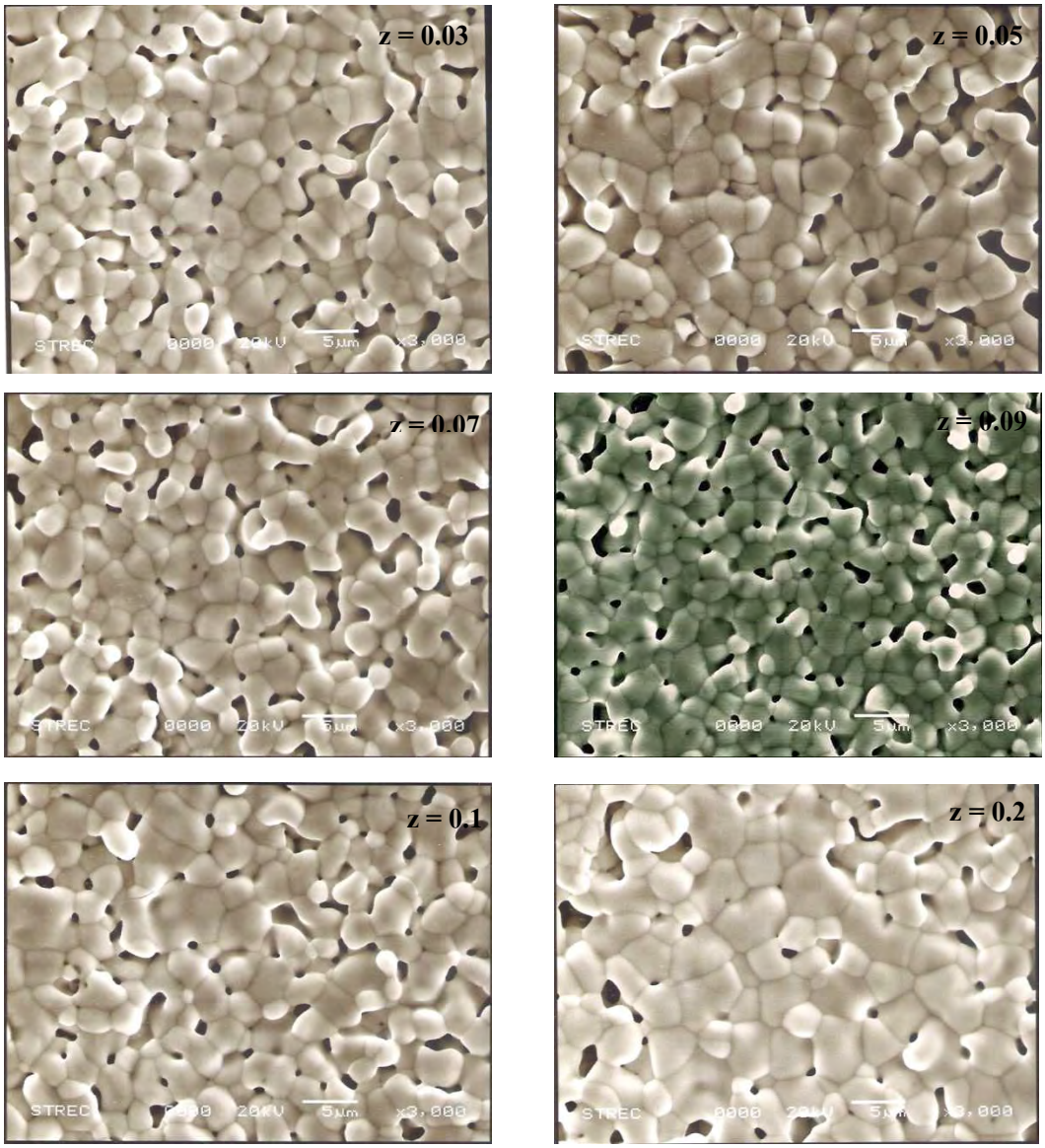

Figure 4.22 Surface morphology of $La_{1.5}Ca_{0.5}Ni_{0.9}Co_{0.1}Ga_zO_{4+\delta}$ (z = 0.00-0.1, 0.2) discs.

Table 4.13 Grains size and relative density of $La_{1.5}Ca_{0.5}Ni_{0.9}Co_{0.1}Ga_zO_{4+\delta}$ (z = 0.00-0.1, 0.2).

Ratio	Grain size (μm)	Relative density (%)
z = 0.0	7.6	97.86
z = 0.01	8.3	88.75
z = 0.03	9.0	89.21
z = 0.05	9.6	90.27
z = 0.07	8.4	90.69
z = 0.09	9.1	89.13
z = 0.1	10.1	89.65
z = 0.2	10.3	90.38

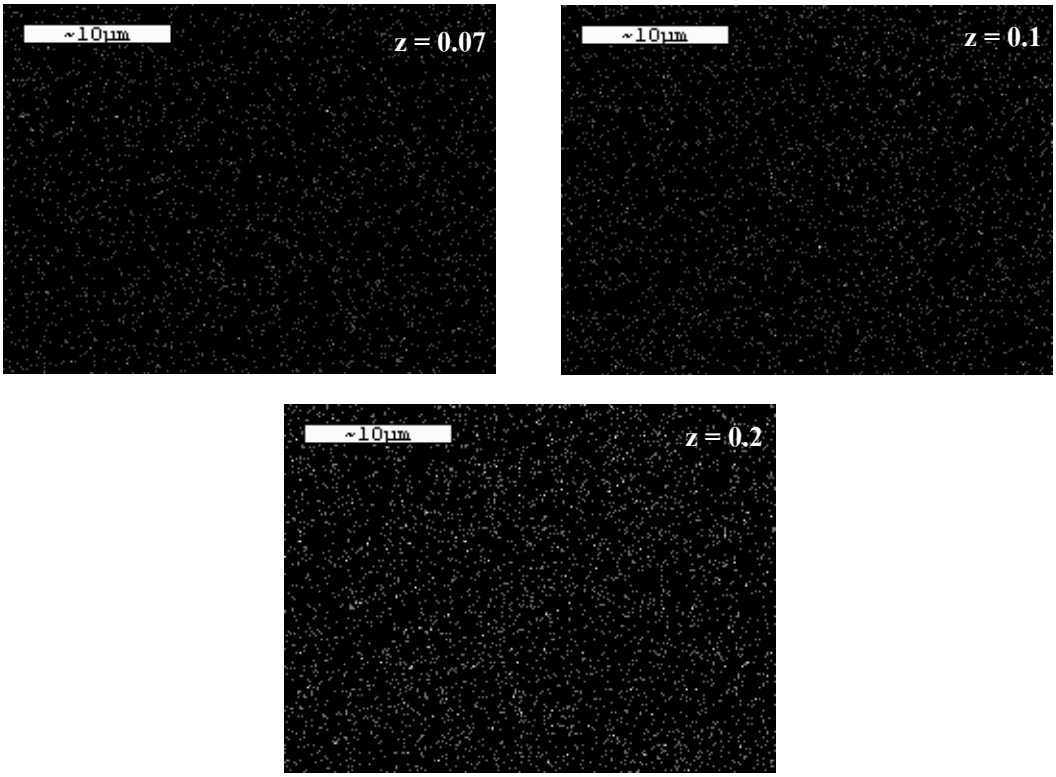

Figure 4.23 Ga-mapping of $La_{1.5}Ca_{0.5}Ni_{0.9}Co_{0.1}Ga_zO_{4+\delta}$ (z = 0.07, 0.1, 0.2) discs.

Figure 4.23 illustrates the homogeneous distribution of Ga^{3+} ion on $La_{1.5}Ca_{0.5}Ni_{0.9}Co_{0.1}Ga_zO_{4+\delta}$ (z = 0.07, 0.1, 0.2) materials. No gallium oxide secondary phase was observed. This result is in agreement with the XRD analysis, which indicates $La_{1.5}Ca_{0.5}Ni_{0.9}Co_{0.1}Ga_zO_{4+\delta}$ (z = 0.07, 0.1, 0.2) are pure single phase materials.

4.3.1.3 The oxygen permeation of $La_{1.5}Ca_{0.5}Ni_{0.9}Co_{0.1}Ga_zO_{4+\delta}$ (z = 0.00-0.1, 0.2)

The oxygen permeation property of $La_{1.5}Ca_{0.5}Ni_{0.9}Co_{0.1}Ga_zO_{4+\delta}$ (z = 0.00-0.1,0.2) were investigated as a function of temperature shown in Figure 4.24.

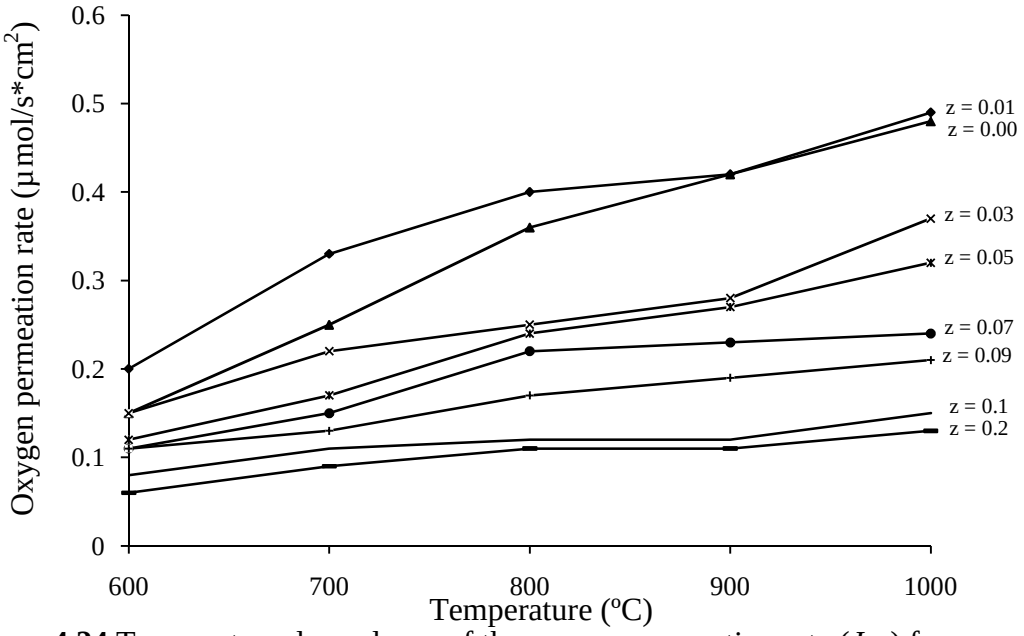

Figure 4.24 Temperature dependence of the oxygen permeation rate (Jo_2) for $La_{1.5}Ca_{0.5}Ni_{0.9}Co_{0.1}Ga_zO_{4+\delta}$ (z = 0.00-0.1, 0.2).

The temperature dependence of the oxygen permeation rate of $La_{1.5}Ca_{0.5}Ni_{0.9}Co_{0.1}Ga_zO_{4+\delta}$ (z = 0.00-0.1, 0.2) materials were increased with increasing temperature, indicating the tendency of oxygen vacancies increase with increasing temperature. With a small amount of Ga^{3+} ion doped by 0.01, the oxygen permeation rate is slightly increased whereas the higher content of Ga^{3+} ion results in the deplete of oxygen permeation rate. Since Ga^{3+} ions are inserted into the spaces availability in the rock-salt layer in K_2NiF_4–type structure, therefore, a small amount of excess Ga^{3+} ion is effective for increasing of oxygen excess interstitial in the rock-salt layer. The introducing of excess oxygen from the interstitial site may diffuse or migrate to the oxygen vacancies in the perovskite layer resulting in the improvement of oxygen permeation rate [76, 79]. While further addition of the excess Ga^{3+} ion from 0.03 to 0.2 reduces the number of oxygen excess in the interstitial position of the rock-salt layer. Then the migration of oxygen excess to the oxygen vacancies is reduced [78]. Therefore, a small amount of excess Ga^{3+} ion is effective for increasing oxygen permeation rate and considering the oxygen permeation rate at 600-800ºC, $La_{1.5}Ca_{0.5}Ni_{0.9}Co_{0.1}Ga_{0.01}O_{4+\delta}$ is a good material for intermediate-temperature solid oxide fuel cell (IT-SOFC).

4.3.1.4 Electrical conductivity of $La_{1.5}Ca_{0.5}Ni_{0.9}Co_{0.1}Ga_zO_{4+\delta}$ (z = 0.00-0.1, 0.2)

Electrical conductivity property of $La_{1.5}Ca_{0.5}Ni_{0.9}Co_{0.1}Ga_zO_{4+\delta}$ (z = 0.00-0.1, 0.2) discs were investigated as a function of temperature as shown in Figure 4.25 and the data are summarized in Table 4.14.

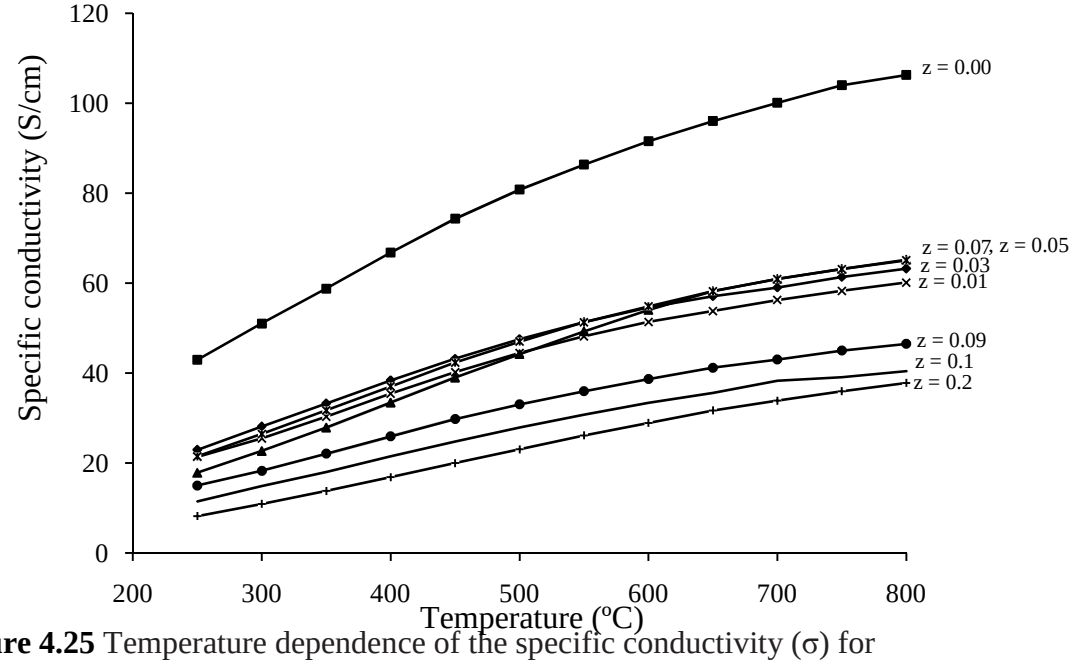

Figure 4.25 Temperature dependence of the specific conductivity (σ) for $La_{1.5}Ca_{0.5}Ni_{0.9}Co_{0.1}Ga_zO_{4+\delta}$ (z = 0.00-0.1, 0.2).

The temperature dependence on the electrical conductivity of $La_{1.5}Ca_{0.5}Ni_{0.9}Co_{0.1}Ga_zO_{4+\delta}$ (z = 0.00-0.1, 0.2) increases with increasing the measuring temperature. In addition, it is also attributed to the loss of oxygen from the lattice to the formation of oxygen vacancies at high temperature [74]. The result shows that the electrical conductivity is decreased when the amount of Ga^{3+} ion was added to the materials. This may be due to the change in oxidation state of La^{3+} and Ni^{3+}, and the distortion of the structure. Considering the change in oxidation state of La^{3+} and Ni^{3+} ions, La^{3+} and Ni^{3+} will be reduced in to La^{2+} or Ni^{2+} and Ni^{1+} ion, when Ga^{3+} is added, the formation of lower valence state of La and Ni introduces the decreased electron hole by the change of neutralization reaction resulting in the decreasing of electronic conductivity [13]. In addition, by doping small amounts of excess Ga^{3+} ion to the interstitial site in the BO_6 octahedral in perovskite layer, the ions are closed and repeled each others causing the distorted structure of K_2NiF_4-type from the B-O-B

angle and tilting of the BO_6 octahedral. That prohibits the overlap of oxygen 2p orbital with the 3d orbital of transition metal.

Table 4.14 Specific conductivity of $La_{1.5}Ca_{0.5}Ni_{0.9}Co_{0.1}Ga_zO_{4+\delta}$ (z = 0.00-0.1, 0.2).

Sample	Specific conductivity (S/cm)						
	300°C	400°C	500°C	600°C	700°C	800°C	σ_{max} (T,°C)
z = 0.00	51.01	66.78	80.79	91.54	100.1	106.3	106.3 (800)
z = 0.01	25.47	35.44	44.56	51.39	56.25	60.12	60.12 (800)
z = 0.03	28.13	38.40	47.56	54.56	59.00	63.21	63.21 (800)
z = 0.05	22.68	33.46	44.22	54.03	60.93	65.20	65.20 (800)
z = 0.07	26.46	37.04	47.00	54.84	60.90	65.09	65.09 (800)
z = 0.09	18.29	25.93	33.06	38.69	43.02	46.52	46.52 (800)
z = 0.1	14.89	21.49	27.91	33.38	38.30	40.43	40.43 (800)
z = 0.2	10.93	16.85	23.04	28.92	33.88	37.83	37.83 (800)

The Arrhenius plot of $La_{1.5}Ca_{0.5}Ni_{0.9}Co_{0.1}Ga_zO_{4+\delta}$ (z = 0.00-0.1, 0.2) is given in Figure 4.26 and the activation energy calculated from the line part of Arrhenius plot are summarized in Table 4.15. It can be seen that the activation energy of in $La_{1.5}Ca_{0.5}Ni_{0.9}Co_{0.1}Ga_zO_{4+\delta}$ increased with increasing the Ga^{3+} ion content.

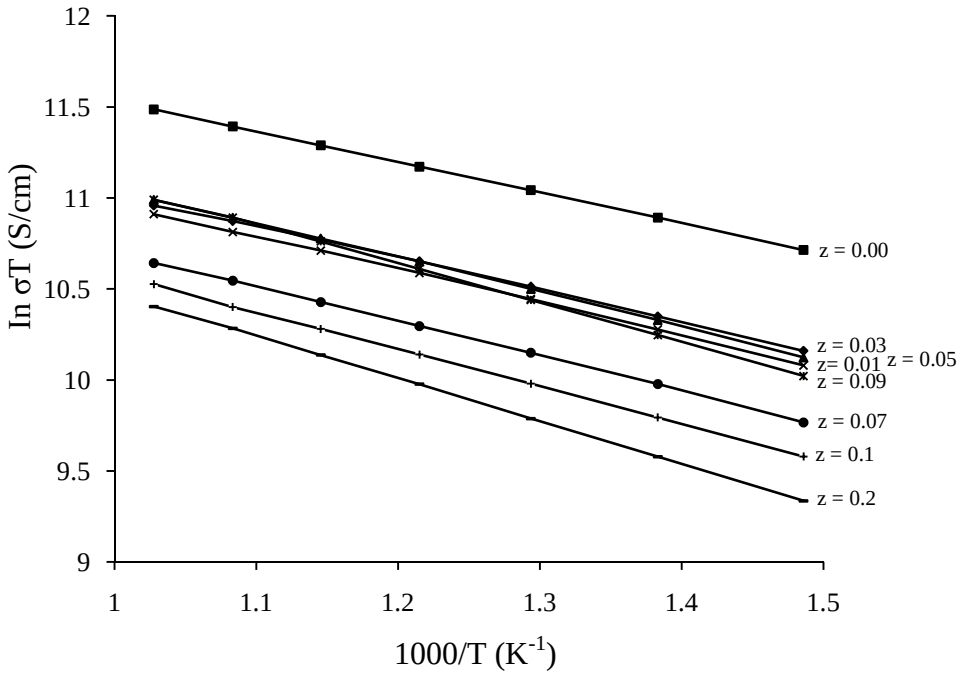

Figure 4.26 Arrhenius plot of the electrical conductivity of $La_{1.5}Ca_{0.5}Ni_{0.9}Co_{0.1}Ga_zO_{4+\delta}$ (z = 0.00-0.1, 0.2).

Table 4.15 Activation energy of $La_{1.5}Ca_{0.5}Ni_{0.9}Co_{0.1}Ga_zO_{4+\delta}$ (z = 0.00-0.1, 0.2) at 400-700ºC.

Sample	E_a **(kJ/mol)**
z = 0.0	12.87
z = 0.01	13.59
z = 0.03	15.64
z = 0.05	13.24
z = 0.07	14.76
z = 0.09	14.97
z = 0.1	15.64
z = 0.2	17.18

4.3.1.5 Thermal expansion coefficients of $La_{1.5}Ca_{0.5}Ni_{0.9}Co_{0.1}Ga_zO_{4+\delta}$ (z = 0.00-0.05)

Dilatometric curves for $La_{1.5}Ca_{0.5}Ni_{0.9}Co_{0.1}Ga_zO_{4+\delta}$ (z = 0.00-0.05) in air are shown in Figure 4.27. The average thermal expansion coefficient (TEC) was defined as the slope of curves and be summarized in Table 4.16.

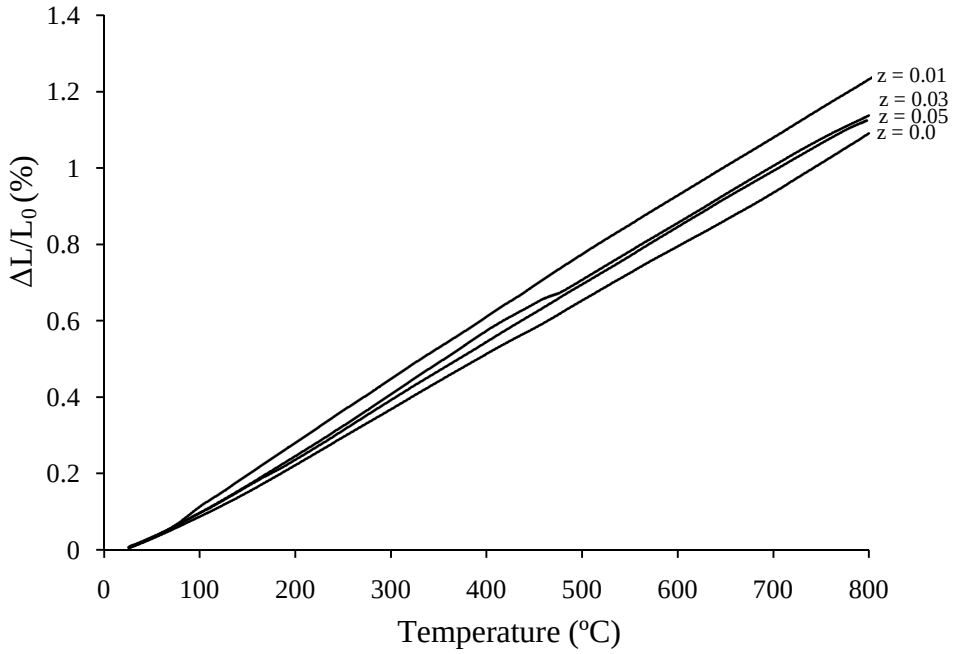

Figure 4.27 Temperature dependence of the thermal expansion for $La_{1.5}Ca_{0.5}Ni_{0.9}Co_{0.1}Ga_zO_{4+\delta}$ (z = 0.00-0.05).

Table 4.16 The average TEC values of $La_{1.5}Ca_{0.5}Ni_{0.9}Co_{0.1}Ga_zO_{4+\delta}$ (z = 0.00-0.05) at 50-800ºC.

Sample	**TEC ($x10^{-6}$ $°C^{-1}$)**
z = 0.00	13.82
z = 0.01	16.03
z = 0.03	14.75
z = 0.05	14.58

Thermal expansion coefficient (TEC) slopes are linear and increased at elevated temperature, which is attributed to the loss of lattice oxygen. That is also associated with the formation of the oxygen vacancies in the lattice. Small addition of Ga^{3+} ion in the K_2NiF_4-type structure associates with the change in low valence state of $La^{3+}$and Ni^{3+} ions to La^{2+} and Ni^{2+} or Ni^{1+} ions. This is the reason that the larger the ionic radius of the La- and Ni-ions, the longer the bond distance for A-O in rock-salt layer and the B-O-B bond in perovskite layer, which suggests a higher concentration of oxygen vacancy formation and the higher TEC [77].

4.3.2 Synthesis and properties of $La_{1.5}Ca_{0.5}Ni_{0.9}Co_{0.1}Ti_zO_{4+\delta}$ (z = 0.00-0.1, 0.2)

4.3.2.1 Synthesis of $La_{1.5}Ca_{0.5}Ni_{0.9}Co_{0.1}Ti_zO_{4+\delta}$ (z = 0.00-0.1, 0.2)

$La_{1.5}Ca_{0.5}Ni_{0.9}Co_{0.1}Ti_zO_{4+\delta}$ (z = 0.00-0.1, 0.2) powders were prepared and calcined at 1200ºC for 6 hrs. The XRD patterns are illustrated in Figure 4.28. $La_{1.5}Ca_{0.5}Ni_{0.9}Co_{0.1}Ti_zO_{4+\delta}$ (z = 0.00-0.05) shows the characteristic patterns of single phase tetragonal K_2NiF_4-type structure. As the material composition is greater than 0.07, the tetragonal K_2NiF_4-type structure and small amount of $CaTiO_3$ impurity phase (PDF No. 43-0226) are detected.

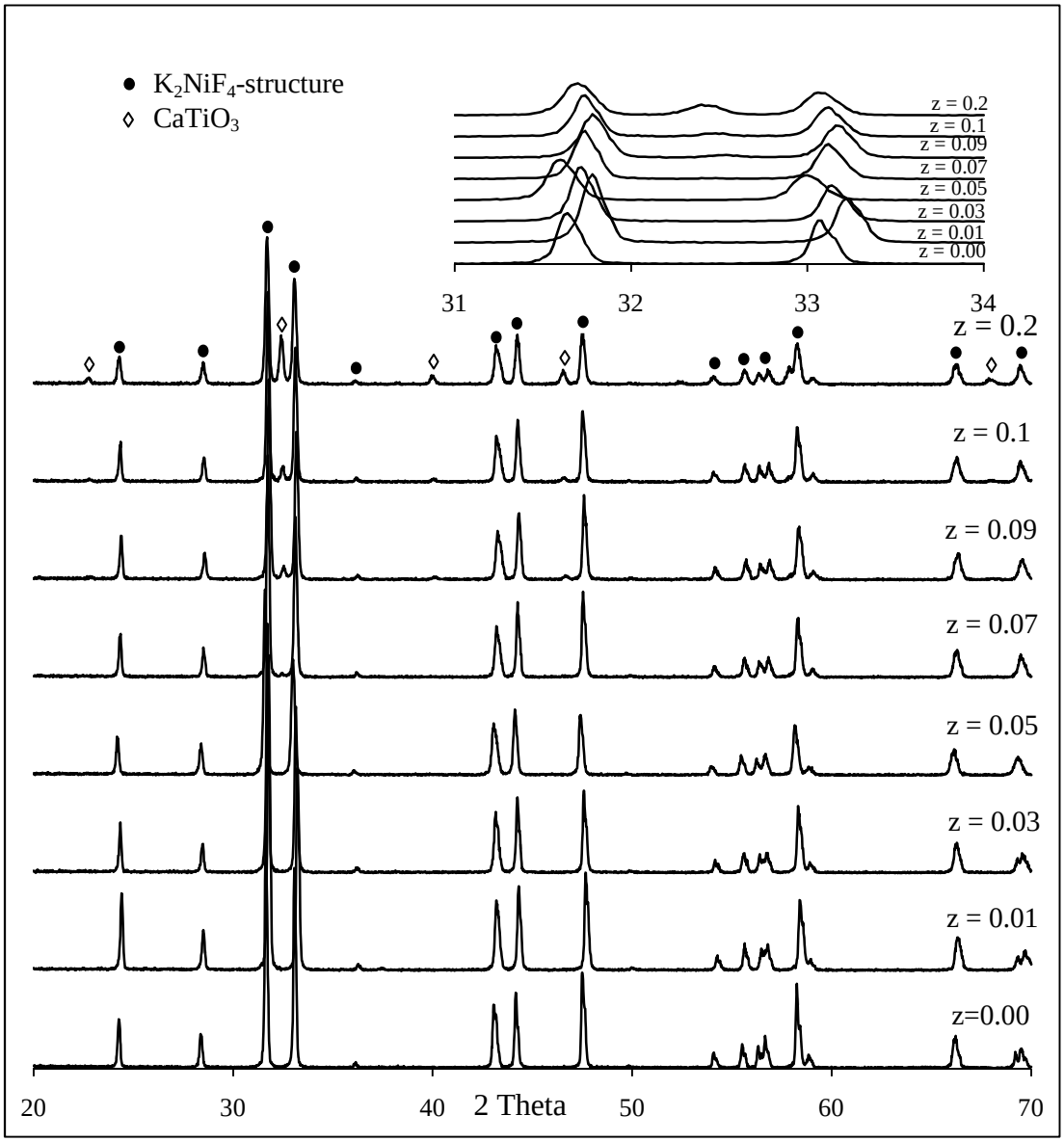

Figure 4.28 XRD patterns of $La_{1.5}Ca_{0.5}Ni_{0.9}Co_{0.1}Ti_zO_{4+\delta}$ (z = 0.00-0.1, 0.2) powder after calcined at 1200°C for 6 hrs.

Figure 4.29 illustrates the XRD patterns of samples sintered at 1300ºC for 6 hrs. All of $La_{1.5}Ca_{0.5}Ni_{0.9}Co_{0.1}Ti_zO_{4+\delta}$ samples distinctively show the K_2NiF_4-type structure. However, only $La_{1.5}Ca_{0.5}Ni_{0.9}Co_{0.1}Ti_zO_{4+\delta}$ (z = 0.00-0.05) gives the pure single phase of tetragonal K_2NiF_4-type structure, while at composition of z = 0.07-0.1, 0.2, secondary phase as $CaTiO_3$ (2θ = 32.5º, PDF No. 43-0226) is observed. The amount of $CaTiO_3$ phase is increased with increasing the addition of Ti^{4+} ion in K_2NiF_4-type structure. The (103) and (110) refection peaks of materials ($2\theta \approx 31.7º$ and 33.2º) are slightly shifted to the lower angle compared to the undoped one, suggesting the expansion of unit cell. The relationship of lattice parameter and cell volume are calculated summarized in Table 4.17. Since the ionic size of Ti^{4+} ion is large (0.75Aº), it can be inserted into the interstitial position in the rock-salt layer leading to the expansion along the *c*-axis and the little shrinkage along the *a*-axis.

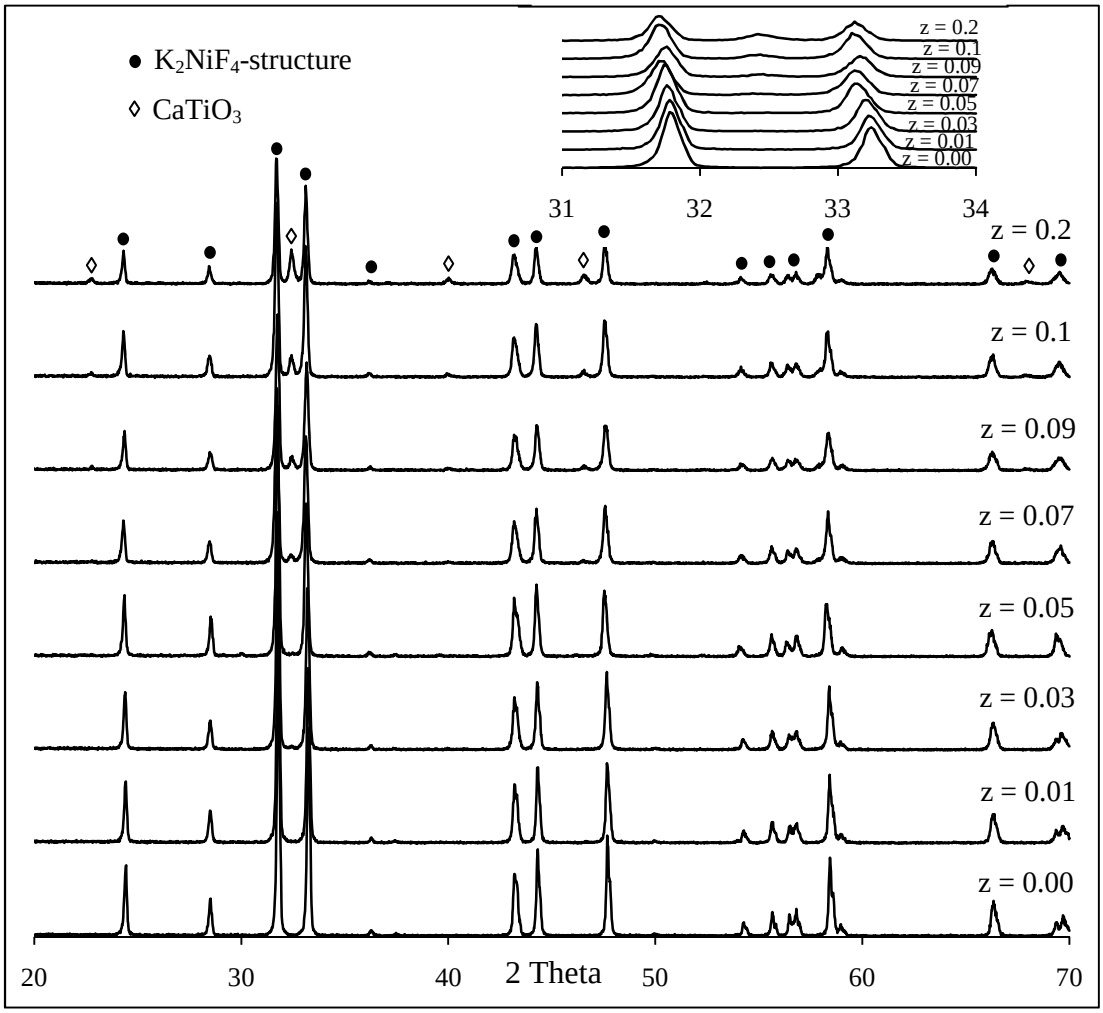

Figure 4.29 XRD patterns of $La_{1.5}Ca_{0.5}Ni_{0.9}Co_{0.1}Ti_zO_{4+\delta}$ (z = 0.00-0.1, 0.2) discs after sintered at 1300ºC for 6 hrs.

Table 4.17 The lattice parameters and cell volume of $La_{1.5}Ca_{0.5}Ni_{0.9}Co_{0.1}Ti_zO_{4+\delta}$ (z = 0.00-0.1, 0.2).

Ration	Lattice parameter (A°)		Cell volume (A^{o3})
	a	*c*	
z = 0.00	3.841	12.120	178
z = 0.01	3.807	12.592	183
z = 0.03	3.811	12.569	183
z = 0.05	3.818	12.568	183
z = 0.07	3.827	12.422	182
z = 0.09	3.818	12.501	182
z = 0.1	3.818	12.591	183
z = 0.2	3.828	12.463	183

4.3.2.2 The surface morphology of $La_{1.5}Ca_{0.5}Ni_{0.9}Co_{0.1}Ti_zO_{4+\delta}$ (z = 0.00-0.1, 0.2)

The surface morphology of $La_{1.5}Ca_{0.5}Ni_{0.9}Co_{0.1}Ti_zO_{4+\delta}$ (z = 0.00-0.1, 0.2) sintered discs were investigated by SEM as shown in Figure 4.30. All discs exhibit porous surface materials. The grain size of samples tends to decrease with increasing the content of Ti^{4+} ion doping, and the relative densities are lower than the undoped material, as summarized in Table 4.18.

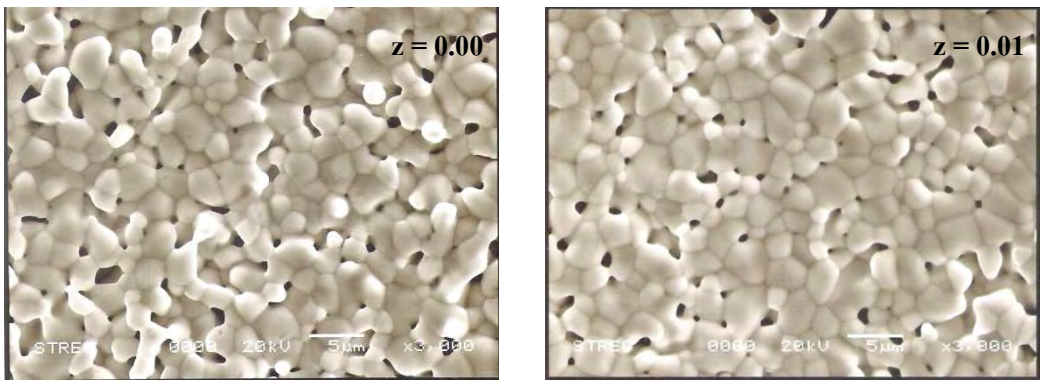

Figure 4.30 Surface morphology of $La_{1.5}Ca_{0.5}Ni_{0.9}Co_{0.1}Ti_zO_{4+\delta}$ (z = 0.00-0.1, 0.2) discs.

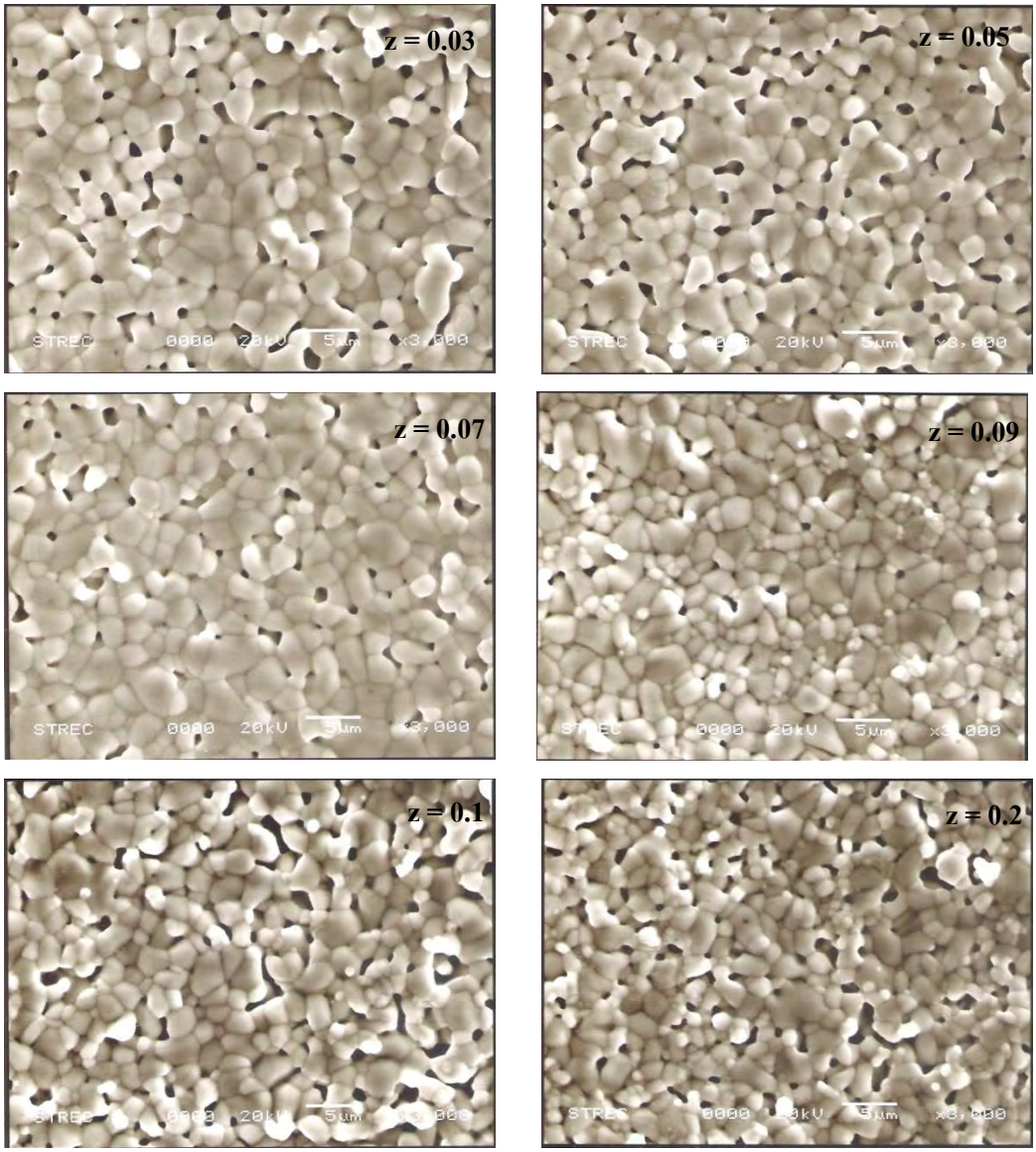

Figure 4.30 Surface morphology of $La_{1.5}Ca_{0.5}Ni_{0.9}Co_{0.1}Ti_zO_{4+\delta}$ (z = 0.00-0.1, 0.2) discs.

Table 4.18 Grain size and relative density of $La_{1.5}Ca_{0.5}Ni_{0.9}Co_{0.1}Ti_zO_{4+\delta}$ (z = 0.00-0.05).

Ratio	Grain size (μm)	Relative density (%)
z = 0.0	7.6	97.86
z = 0.01	7.4	95.97
z = 0.03	6.5	93.56
z = 0.05	6.5	91.23

4.3.2.3 The oxygen permeation of $La_{1.5}Ca_{0.5}Ni_{0.9}Co_{0.1}Ti_zO_{4+\delta}$ (z = 0.00-0.05)

The oxygen permeation property of $La_{1.5}Ca_{0.5}Ni_{0.9}Co_{0.1}Ti_zO_{4+\delta}$ (z = 0.00-0.05) were investigated as a function of temperature shown in Figure 4.31.

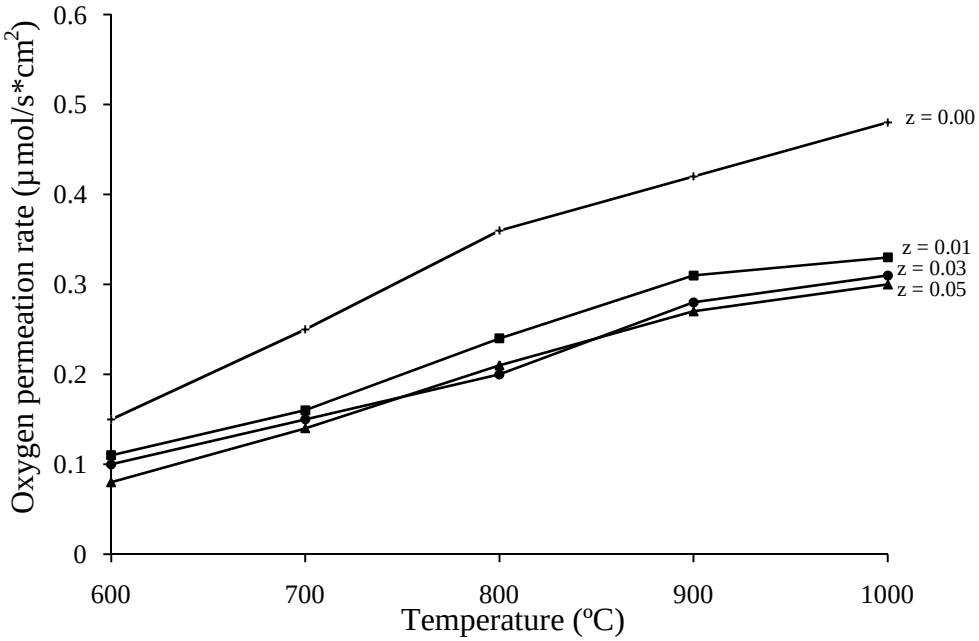

Figure 4.31 Temperature dependence of the oxygen permeation rate (Jo_2) for $La_{1.5}Ca_{0.5}Ni_{0.9}Co_{0.1}Ti_zO_{4+\delta}$ (z = 0.00-0.05).

The temperature dependence of oxygen permeation rate of $La_{1.5}Ca_{0.5}Ni_{0.9}Co_{0.1}Ga_zO_{4+\delta}$ (z = 0.00-0.05) materials were increased with increasing temperature, indicating the tendency of oxygen vacancy increases at high temperature. With a small amount of Ti^{4+} ion doped, the oxygen permeation rate is decreased indicating that the oxygen vacancy is decreased. This is because Ti^{4+} ion has a high valence state, which will annihilate oxygen vacancies in the perovskite layer by changing neutralization reaction. The excess oxygen in the rock – salt later cannot migrate to the oxygen vacancies in the perovskite layer resulting in the decrease of oxygen permeation rate [81]. In addition, the Ti^{4+} ion inserted into the interstitial position in the rock-salt layer, can reduce the number of oxygen excess in the interstitial position of rock – salt layer. Then the migration of oxygen excess from rock – salt structure to the oxygen vacancies in the perovskite layer is reduced [78, 82]. It has been concluded that a small amount of excess Ti^{4+} ion is effective for decreasing the oxygen permeation rate.

4.3.2.4 Electrical conductivity of $La_{1.5}Ca_{0.5}Ni_{0.9}Co_{0.1}Ti_zO_{4+\delta}$ (z = 0.00-0.05)

Since $La_{1.5}Ca_{0.5}Ni_{0.9}Co_{0.1}Ti_zO_{4+\delta}$ (z = 0.00-0.05) gave the pure single phase structure, the electrical conductivity of the material discs were investigated as a function of temperature shown in Figure 4.32 and the data are summarized in Table 4.19.

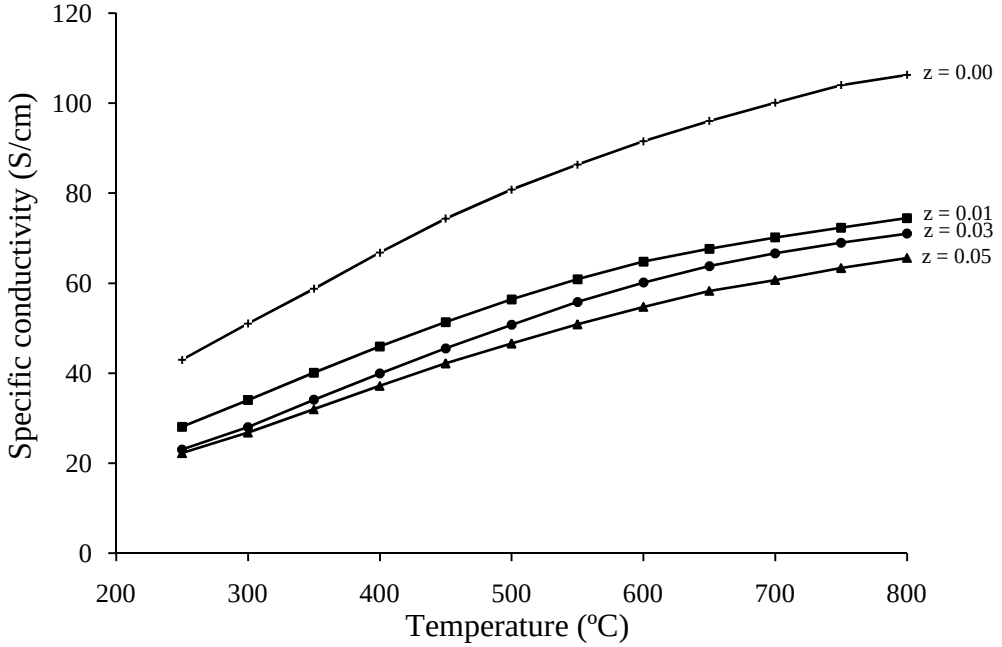

Figure 4.32 Temperature dependence of the specific conductivity (σ) for $La_{1.5}Ca_{0.5}Ni_{0.9}Co_{0.1}Ti_zO_{4+\delta}$ (z = 0.00-0.05).

The temperature dependence on electrical conductivity of $La_{1.5}Ca_{0.5}Ni_{0.9}Co_{0.1}Ti_zO_{4+\delta}$ (z = 0.00-0.05) increases with increasing the measuring temperature, which attributes to the loss of oxygen from the lattice to the formation of oxygen vacancies at high temperature [74]. For z = 0.01-0.05, the electrical conductivities are decreased. This result can be explained by the effect of Ti^{4+} ion doping, which may be introduced to the interstitial site in the BO_6 octahedral in perovskite layer. Since the Ti^{4+} ion has no 3d electrons, when Ti^{4+} ion is added, parts of the B-O-B are broken, due to no electron hopping from oxygen 2p orbital with the 3d orbital of transition metal. A disorder introduction of Ti^{4+} ion by B-O-Ti bond causes the decrease of electrical conductivity [80].

Table 4.19 Specific conductivity of $La_{1.5}Ca_{0.5}Ni_{0.9}Co_{0.1}Ti_zO_{4+\delta}$ (z = 0.00-0.05).

Sample	Specific conductivity (S/cm)						
	300°C	400°C	500°C	600°C	700°C	800°C	σ_{max} (T,°C)
z = 0.0	51.01	66.78	80.79	91.54	100.1	106.3	106.3 (800)
z = 0.01	34.01	45.92	56.39	64.79	70.17	74.45	74.45 (800)
z = 0.03	28.01	39.92	50.73	60.12	66.64	71.01	71.01 (800)
z = 0.05	26.81	37.17	46.59	54.72	60.67	65.61	65.61 (800)

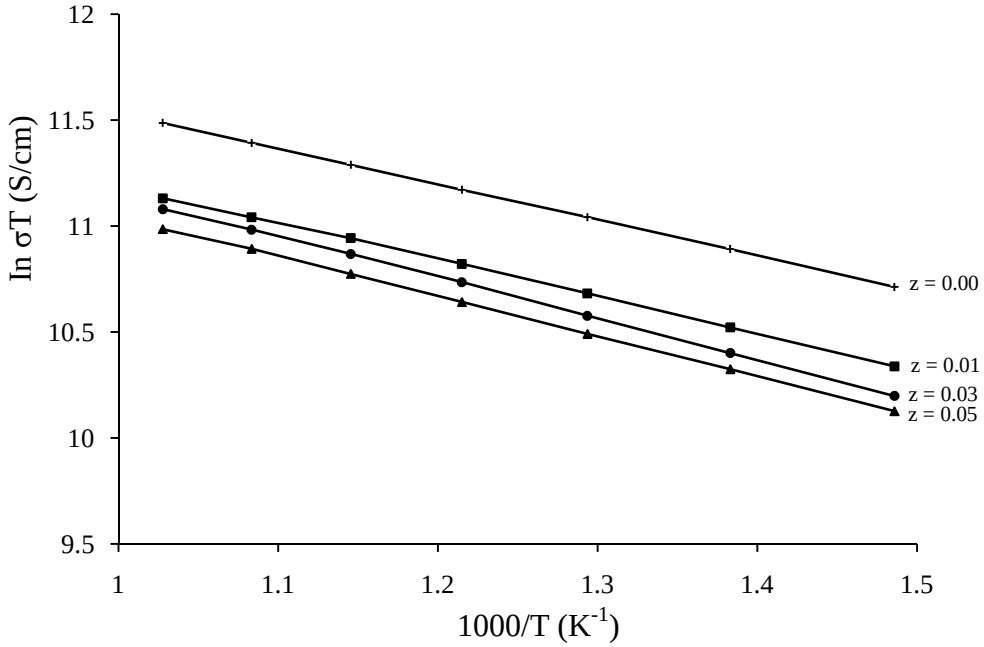

Figure 4.33 Arrhenius plot of the electrical conductivity of $La_{1.5}Ca_{0.5}Ni_{0.9}Co_{0.1}Ti_zO_{4+\delta}$ (z = 0.00-0.05).

Table 4.20 Activation energy of $La_{1.5}Ca_{0.5}Ni_{0.9}Co_{0.1}Ti_zO_{4+\delta}$ (z = 0.00-0.05) at 400-700ºC.

Sample	E_a (kJ/mol)
z = 0.0	12.87
z = 0.01	13.63
z = 0.03	14.72
z = 0.05	14.38

Table 4.20 shows the activation energy of materials increased with the Ti^{4+} ion addition.

4.3.2.5 Thermal expansion coefficients of $La_{1.5}Ca_{0.5}Ni_{0.9}Co_{0.1}Ti_zO_{4+\delta}$ (z = 0.00-0.05)

Dilatometric curves of $La_{1.5}Ca_{0.5}Ni_{0.9}Co_{0.1}Ti_zO_{4+\delta}$ (z = 0.00-0.05) in air are shown in Figure 4.33. The average thermal expansion coefficient (TEC) was defined as the slope of curves and be summarized in Table 4.21.

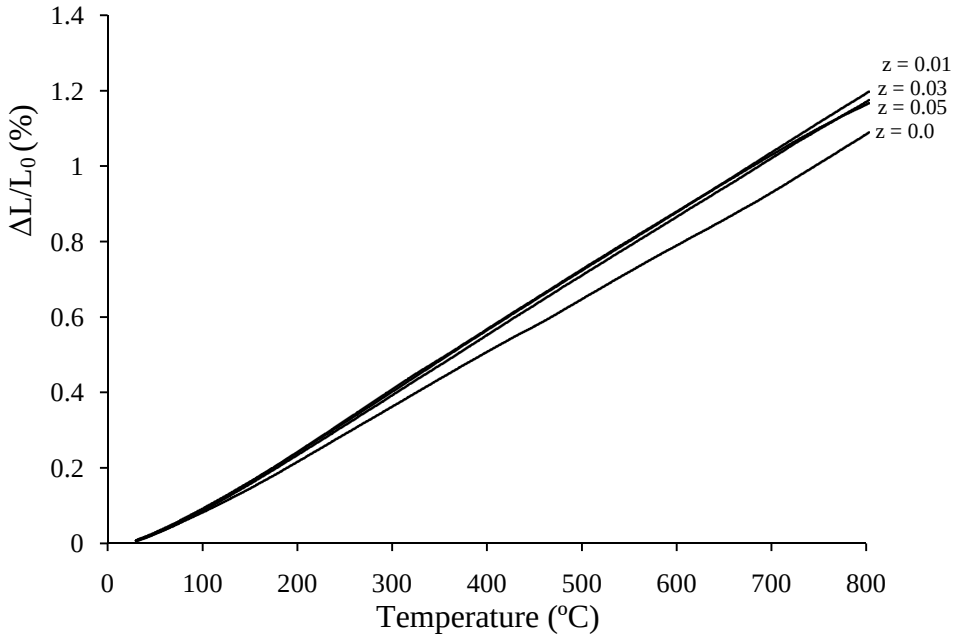

Figure 4.34 Temperature dependence of the thermal expansion for $La_{1.5}Ca_{0.5}Ni_{0.9}Co_{0.1}Ti_zO_{4+\delta}$ (z = 0.00-0.05)

Table 4.21 The average TEC values of $La_{1.5}Ca_{0.5}Ni_{0.9}Co_{0.1}Ti_zO_{4+\delta}$ (z = 0.00-0.05) at 50-800ºC.

Sample	TEC ($x10^{-6}$ °C^{-1})
z = 0.00	13.82
z = 0.01	15.26
z = 0.03	15.17
z = 0.05	15.52

Thermal expansion coefficient (TEC) sloped are linear and increased at elevated temperature, which is attributed to the loss of lattice oxygen. That is associated with the formation of the oxygen vacancies in the lattice. Small addition of Ti^{4+} ion in the K_2NiF_4-type structure makes the TEC value higher than the undoped

materials. The reason is that the larger the ionic radius of the Ti^{4+} ion, the longer the bond distance of A-O in rock-salt layer.

In this research the electrical conductivity was 106.03 S/cm at 800ºC and oxygen permeation rate was 0.48 µmol/s.cm^2 at 1000ºC of $La_{1.5}Ca_{0.5}Ni_{0.9}Co_{0.1}O_{4+\delta}$ are compared with those of other K_2NiF_4 structure *e.g.* the electrical conductivity of $Pr_2Ni_{0.75}Cu_{0.25}O_{4+\delta}$ was 79.43 S/cm at 1000ºC and the oxygen permeation rate was 0.83 µmol/s.cm^2 at 1000ºC reported [14]. Therefore, it is concluded that $La_{1.5}Ca_{0.5}Ni_{0.9}Co_{0.1}O_{4+\delta}$ is a potential candidacy for the intermediate temperature solid oxide fuel cell (IT-SOFC, 600-800ºC).

CHAPTER V

CONCLUSIONS

5.1 Conclusions

$La_2NiO_{4+\delta}$, the substitution of Co^{2+} ion at B-site, the substitution of Ca^{2+} ion at A-site and the additions of $Ga^{3+}$and Ti^{4+} ion in the structure were successfully synthesized by modified citrate method. All compositions were calcined at temperature of 1200ºC and sintered at 1300ºC for 6 hrs. The synthesized compounds were characterized by XRD, SEM and investigated the properties for oxygen permeation, electrical conductivity and thermal expansion coefficient.

$La_2Ni_{1-y}Co_yO_{4+\delta}$ (y = 0.1-0.2) materials have a tetragonal of the K_2NiF_4-type structure and small amount of La_2O_3 impurity phase. The surface morphology of the sintered discs examined by SEM revealed that the increase in Co^{2+} ion substitution promotes the increasing of grain size of materials. The oxygen permeation rate and thermal expansion coefficient were increased whereas the electrical conductivity was decreased when the Co^{2+} ion content increased. However, $La_2Ni_{0.9}Co_{0.1}O_{4+\delta}$ showed the highest oxygen permeation rate of 0.78 $\mu mol/s.cm^2$ at 1000ºC in this research.

The substitution of Ca^{2+} ion in $La_{2-x}Ca_xNi_{0.9}Co_{0.1}O_{4+\delta}$ (x = 0.0-1.0) to produce tetragonal K_2NiF_4-type structure was achieved. At x = 0.5, only pure single phase of K_2NiF_4-type structure was obtained whereas at x = 0.1-0.3 and x = 0.7-1.0, the La_2O_3 impurity phase and the CaO impurity phase were present, respectively. The SEM analysis was concluded that the grain size of samples decreases with increasing the content of Ca^{2+} ion doping because the ionic radii of Ca^{2+} ion is smaller than that of La^{3+} ion. The electrical conductivity was increased whereas oxygen permeation rate and thermal expansion coefficient were decreased when the increasing of Ca^{2+} ion doping at 0.5. However, The maximum electrical conductivity was achieved for the $La_{1.5}Ca_{0.5}Ni_{0.9}Co_{0.1}O_{4+\delta}$ sample at 106.3 S/cm^2 at 800ºC.

A single phase tetragonal of the K_2NiF_4-type structure was obtained from the addition of Ga^{3+} ion in the $La_{1.5}Ca_{0.5}Ni_{0.9}Co_{0.1}Ga_zO_{4+\delta}$ (z=0.00-0.1, 0.2). Since the ionic size of Ga^{3+} ion is small, it can be inserted into interstitial position of the rock – salt layer. The SEM characterization revealed that grain size of samples increases

with increasing of Ga^{3+} ion doping. The oxygen permeation rate, electrical conductivity and thermal expansion coefficient were decreased when the amount of Ga^{3+} ion was added to the materials. In this work, non-stochiometric $La_{1.5}Ca_{0.5}Ni_{0.9}Co_{0.1}Ga_{0.01}O_{4+\delta}$ material gave the highest oxygen permeation at 0.49 μmol/s.cm^2 at 1000ºC.

The addition of Ti^{4+} ion in $La_{1.5}Ca_{0.5}Ni_{0.9}Co_{0.1}Ti_zO_{4+\delta}$ (z=0.00-0.1, 0.2) to produce a tetragonal of the K_2NiF_4-type structure was investigated. At z=0.00-0.05, the pure single phase of tetragonal K_2NiF_4-type structure was obtained while z≥0.07, $CaTiO_3$ impurity phase was observed. The SEM analysis incicated that grain size of samples decreases with increasing the content of Ti^{4+} ion doping. The oxygen permeation rate and electrical conductivity were decreased whereas the thermal expansion coefficient was increased when the amount of Ti^{4+} ion was added to the materials.

In conclusion, the substitution of Co^{2+} ion in B-site of $La_2NiO_{4+\delta}$ improved the oxygen permeation rate of materials while the substitution of Ca^{2+} ion in A-site improved the electrical conductivity of materials. The additions of Ga^{3+} and Ti^{4+} ion in the structure had no effect on the oxygen permeation rate but reduced the electrical conductivity. From this research, $La_{1.5}Ca_{0.5}Ni_{0.9}Co_{0.1}O_{4+\delta}$ material has the mixed ionic-electronic conducting property for using as a future solid oxide fuel cell (SOFC).

5.2 Suggestion

From experimental results, the future work should be focused on the following:

1. To study the compatibility of $La_{1.5}Ca_{0.5}Ni_{0.9}Co_{0.1}O_{4+\delta}$ cathode materials with the 8%-YSZ electrolyte for SOFC.
2. To investigate the property of $La_{1.5}Ca_{0.5}Ni_{0.9}Co_{0.1}O_{4+\delta}$ cathode on the 8%-YSZ electrolyte for oxygen permeation rate, electrical conductivity and thermal expansion coefficient.

REFERENCES

[1] Singhal, S. C. Advances in solid oxide fuel cell technology. *Solid State Ionics* 135(2000) 305-313.

[2] Minh, N. Q. Ceramic Fuel Cells. *J. Am. Ceramic Society* 76(1993) 563-588.

[3] Kharton, V.V., Viskup, A. P., and Margues, F.M.B. Ionic transport in oxygen-hyperstochimetric phases with K_2NiF_4-type structure. *Solid State Ionics* 143(2001) 337-353.

[4] Bevilacqua, M., Montini, T., Tavagnacco, C., Vicario, G., and Fornasiero, P. Influence of synthesis route on morphology and electrical properties of $LaNi_{0.6}Fe_{0.4}O_3$. *Solid State Ionics* 177(2006) 2957-2965.

[5] Ishihara, T., Tsuruta, Y., and Takita, Y. Fe doped $LaGaO_3$ perovskite oxide as an oxygen separating membrane for CH_4 partial oxidation. *Solid State Ionics* 152-153(2002) 709-714.

[6] Daroukh, M.A., Vashook, V.V., and Rai, I.A. Oxide of the ABO_3 and A_2BO_4-type: Structure stability, electrical conductivity and thermal expansion. *Solid State Ionics* 158(2003) 141-150.

[7] Escudero, M.J., Ayuadero, A., and Daza, L.A. A kinetic study of oxygen reduction reaction on La_2NiO_4 cathode by means of impudence spectroscopy. *Journal of Electroanalytical Chemistry* 611(2007) 107-116.

[8] Mori, M.; Sammes, N.M, and Takeda, Y. Application of $La_{0.6}AE_{0.4}MnO_3$ (AE = Ca and Sr) to electric current collectors on high-temperature solid oxide fuel cell. *Solid State Ionics* 164(2003) 1-15.

[9] Ding, X., Liu, Y., Gao, L., and Guo. L. Effect of cation substitution on thermal expansion and electrical properties of lanthanum chromites. *Journal of Alloys and Compounds* 425(2006) 318-322.

[10] Burriel, R., Castro, M., and Saez-Puche, R. Calorimetric study of the structural and magnetic ordering in R_2NiO_4 (R = La, Pr and Nd). *Pure & Application Chemistry* 67(1995) 1825-1830.

[11] Qing, X., Huang, D., and Zhang, F. Synthesis and electrical conductivity of $La_2NiO_{4+\delta}$ derived from a polyamino carboxylate complex precursor. *Material Letters* 60(2006) 1892-1895.

[12] Riza, F., and Ftikos, Ch. Influence of A- and B-site doping on the properties of the system $La_2CoO_{4+\delta}$. *Journal of the European Ceramic Society* 27 (2007) 571-573.

[13] Lee, K.T. Effect of cation doping on the physical properties and electrochemical performance of $Nd_{0.6}Sr_{0.4}Co_{0.8}M_{0.2}O_{3-\delta}$ (M = Ti, Cr, Mn, Fe, Co and Cu) cathodes. *Solid State Ionics* 178(2007) 995-1000.

[14] Ishihara, T., Nakashima, K., and Matsumoto, H. Defect chemistry and oxygen permeation property of $Pr_2Ni_{0.75}Cu_{0.25}O_4$ oxide doped with Ga. *Solid State Ionics* 179(2008) 1367-1371.

[15] Zhang, L., Chen, X., and Xiang, Y. Characterization of doped $La_{0.7}A_{0.3}Cr_{0.5}Mn_{0.5}O_{3-\delta}$ (A = Ca, Sr, Ba) electrode for Solid Oxide Fuel Cell. *Solid State Ionics* 180(2009) 1076-1082.

[16] Geoffrey, A., Tompset, T., and Sammes, N.M. Ceria–Yttria–Stabilized Zirconia Composite Ceramic systems for Application as Low-Temperature Electrolyte. *Journal of the European Ceramic Society* 80(1997) 3181-3186.

[17] Song, C. Fuel processing for low-temperature and high-temperature fuel cell Challenges, and opportunities for sustainable development in the 21st century. *Catalysis Today 77*(2002) 17-47.

[18] Solid Oxide Fuel Cell [online]. Available from: http://www.mne.eng.psu.ac.th/knowledge/student/fuelcell/sofc.html [2009, November 3]

[19] Singhal, S.C. Advances in solid oxide fuel cell technology. *Solid State Ionics* 135(2000) 305-315.

[20] Stambouli, A.B., and Traversa, E. Solid oxide fuel cell (SOFC) a review of an environmentally clean and efficient source of energy. *Renewable and Sustainable Energy Review* 6(2002) 433-455.

[21] Sammes, N. M., and Cai, Z. Ionic conductivity of ceria/yttria stabilizd zirconia electrolyte materials. *Solid State Ionics* 100(1997) 39-44.

[22] Zhu, B. Advantages of intermediate temperature solid oxide fuel cells for tractionary application. *Journal of Power Sources* 93(2001) 82-86.

[23] Haile, S. M. Fuel cell materials and components. *Acta Materialia* 51(2003) 5981-6000.

[24] Yamamoto, O. Solid oxide fuel cells : fundamental as pacts and prospects. *Elctrochemixal Acta* 45(2000) 2423-2429.

[25] Tsoga, A., Naoumidis, A., and Stevar, D. Total electrical conductivity and defect structure of ZrO_2-CeO_2-Y_2O_3-Gd_2O_3. *Solid State Ionics* 135(2000) 403-409.

[26] Huismans, J.P.P., Berkel, F.P.F, and Christe, G.M. Intermediate temperature SOFC-a promise for 21st century. *Journal of Power Source* 71(1998) 107-110.

[27] Zhang, T.S., Ma, J., and Kolner, J.A. Intermediate-temperature ionic conductivity of ceria-based solid solutions as a function of gadolinia and silica content. *Solid State Science* 6(2004) 565-572.

[28] Ivers - Tiffee, E., Weben, A., and Herbstritt, D. Materials and technologics for SOFC-components. *Journal of the European Ceramic Society* 21(2001) 1805-1811.

[29] Escudero M.J., Aguadero, A., Alonso, J.A., and Daza, L. A kinetic study of oxygen reduction reaction on La_2NiO_4 cathodes. *Electro analytical chemistry* 115(2007) 107-116.

[30] Badwal, S.P.S., and Foger, K. Soild Oxide Electrolyte Fuel Cell Review. *Ceramics International* 22(2001) 257-265.

[31] Rao, C.N.R., Gopalakrishnan, J., and Vidyasagar, K. Superstructure, Ordered Defects and Nonstochiometry in Metal Oxides of Perovskite and elated structure. *Indian Journal of Chemistry* 23A(4)(1984) 265-284.

[32] Li, C., Soh, K.C.K., and Wu, P. Formability of ABO_3 perovskite. *Journal of Alloys and Compounds* 372(2004) 40-48.

[33] Feng, F.M., Jiang, L.Q., Zhu, M., and Zhou, X. Formability of ABO_3 cubic perovskite. *Journal of Physics and Chemistry* (2007)

[34] Chroneos, A., Vovk, R.V., and Goulatio, L.I. Oxygen transport in perovskite and related oxides : A brief review. *Journal of Alloys and Compounds* 494(2010) 190-195.

[35] Ishigaki, T., Toda, K., and Watanabe, T. Melt synthesis of oxide phosphors with K_2NiF_4 structure : $CaLa_{1-x}Eu_xGaO_4$. *Journal Metal Sci* 43(2008) 4749-4752.

[36] Yang, X., Zhu, J., and Wu, T. Study of $La_{2-x}Sr_xCuO_4$ (x = 0.0, 0.5, 1.0) catalyst for NO+CO reaction from the measurement of O_2–TPD, H_2–TPR and cyclic voltammetry. *Journal of Molecular catalysis A. Chemical* 238(2005) 35-40.

[37] Tang, R.I.D., and Manthiram, A. Comparison of the crystal chemistry and electrical properties of $La_{2-x}A_xMO_4$ (M = Ca, Sr, Ba). *Materials Research Bulletin* 35(2000) 411-424.

[38] Ullmann, H., and Trofimanko, N. Composition, Composition, Structure and transport of perovskite-type oxide. *Solid State Ionics* 119(1999) 1-8.

[39] Patel, R., Simon, C., and Weller, M.T. $LnSrScO_4$ (Ln = La, Ce, Pr, Nd and Sm) systems and structure correlations for A_2BO_4 (K_2NiF_4) structure types. *Journal of Soild State Chemistry* 180(2007) 349-359.

[40] Mizusak, J.; Yoshihiro, M., Tamauchi, S., and Fueki, K. Non-stochiometry and defect structure of the perovskite-type oxide $La_{1-x}Sr_xFeO_{3-\delta}$. *Solid State Chemistry* 58(1985) 257-266.

[41] Teraoka, Y., Nobunaga, T., and MYamazoe, N. Effect of cation substitution on the oxygen semipermeability of perovskite-type oxide. *Chemistry Letter* (19998) 503-506.

[42] Sunarson, J., Baumannb, S., Sawac, J.M., and Dinizda Casta, J.C. Mixed ionic–electronic conducting (MIEC) ceramic-based membranes for oxygen separation. *Journal of Membrane Science* 320(2008) 13-41.

[43] Ullman, H., Trofimenko, N., and Ahmad-Khanbu, A. Correlation between thermal expansion and oxide ion transport in mixed conduction perovskite-type oxide for SOFC cathodes. *Solid State Ionics* 138(2000) 79-90.

[44] Thursfield, A., and Metcalfe, I.S. The use of dense mixed ionic and electronic conductivity membranes for chemical production. *J. Mater. Chem* 14(2004) 2475-2485.

[45] Dawson, W.J. Hydrothermal synthesis of advanced ceramic powder. *Advances in Science and Technology* 45(2006) 184-193.

[46] Mori, M., Sammes, N.M., and Suda, E. Application of $La_{0.6}AE_{0.4}MnO_3$ (AE = Ca and Sr) to electric current collectors in high-temperature solid oxide fuel cell. *Solid State Ionics* 164(2003) 1-15.

[47] Thermal expansion [online]. Available from: http://hyperphysics.phy-astr.gsu.edu/Hbase/thermo/thexp.html[2009, December 30]

[48] Liu, S., Tan, X., and Hughes, R. Synthesis of strontium cerates-based perovskite ceramics via water-soluble complex precursor routes. *Ceramics International* 28(2002) 327-335.

[49] Hart, A.M., Peters, B.C., and Machi, J.M. Advanced ceramic appertumties-a review. *Chemical Engineering Progress* 85(1989) 44-52.

[50] Cousin, P., and Ross, R.A. Preparation of mixed oxides : a review. *Materials Science and Engineering* 130(1990) 119-125.

[51] Cushing, B.L., and Kolesnichenko, V.L., O'Connor, C.J. Recent advances in the liquid phase synthesis of inorganic nanoparticles. *Ceramical Reviews* 104(2004) 3893-3897.

[52] Wei, B., L¨u, Z., Huang, X., Liu, M., Li, N., and Su,W. Synthesis, electrical and electrochemical properties of $Ba_{0.5}Sr_{0.5}Zn_{0.2}Fe_{0.8}O_{3-\delta}$ perovskite oxide for IT-SOFC cathode. *Journal of Power Sources* 176(2008) 1-8.

[53] Pechini, M.P., Method of preparing lead and alkaline earth titanates and niobates and coating method using the same to from a capacitor. *US Patent* 3,330,697(1967).

[54] Lenntech, Calcination [Online]. Available from: http://www.lenntect.com/chemistry/calcination.ht [2009, November 10]

[55] Kuczynski, G.C. Trasactions of the American Institute of Mining Metallurgical and Petroleum Engineering. *Journal of Applied Physics* 21(1950) 632-637.

[56] Wu, Z., Zhou, W., and Xu, N. Effect of pH on Synthesis and Properties of Perovskite Oxide via a Citrate Process. *Materials, interfaces, and Electrochemical phenomena* 52(2006) 769-776.

[57] Hayashi, H., Inaba, H., and Tagawa, H. Structure consideration on the ionic conductivity of perovskite – type oxide. *Solid State Ionics* 122(1999) 1-15.

[58] An in-situ four-point probe method for the electrical characterization of beam induced depositions (online). Available from : http://www.nanotechnik.com/fileadmin/public/publications/in-situ_four-point-probe.pdf [2008, May 15]

[59] Taniguchi, S., and Aniya, M.; Huang. Relationship Between Thermal Expansion, Ionic Conduction and Ionicity in Perovskite-type Oxide. *Intergrated Ferroelectrics* 115(2010) 18-24.

[60] Li, S., Sin, W., and Shi, J. Comparison of oxygen permeability and stability of perovskite-type $La_{0.2}A_{0.8}Co_{0.2}Fe_{0.8}O_{3-\delta}$ (A = Sr, Ba, Ca) membranes. *Solid State Ionics* 38(1999) 2963-2972.

[61] Kharton, A.A., Yaremchenko, A.A., Tsipis, E.V., and Frade, J.R. Oxygen transport and electrochemical activity of La_2NiO_4-based cathode materials. *Department of Ceramics and Glass Engineering* 3810-193.

[62] Yu, H.C., and Fung, K.Z. Role of strontium addition on the phase transition of lanthanum copper oxide from K2NiF4 to perovskite structure. *Journal of Alloys and Compounds* 440(2007) 62-68.

[63] Nishiyama, S., Sakaguchi, D., and Hattori, T. Electrical conduction and thermoelectricity of $La_2NiO_{4+\delta}$ and $La_2(Ni, Co)O_{4+\delta}$. *Solid State Communication* 94(1995) 279-282.

[64] Chibiao, L., Zhen, Z., and Xingkai, Y. Catalysis of the rare earth containing mixed oxide La_2CuO_4 in phenol hydroxylation. *Science in China* 40(1997) 512-516.

[65] Zhou, N., Chen, G., and Zhang, H.Z. Synthesis and transport properties of La_2NiO_4. *Physica* B404(2009) 4150-4154.

[66] Takahashi, J., Nakada, H., Satoh, H. and Kamegashira, N. Orthorhombic distortion in $Ca_{2-x}Gd_xMnO_4$. *Journal of Alloy and Compounds* 408-412(2006) 598-602.

[67] Aguadero, A., Alonso, J.A., Escodero, M.J., and Daza, L. In situ high temperature neutron powder diffraction study of $La_2Ni_{0.6}Cu_{0.4}O_{4+\delta}$ in air: Correlation with the electrical behavior. *Journal of Power Sources* 169(2007) 17-24.

[68] Dragon, M.A. Defect Chemistry, Transport Properties and Thermodynamic Stability of Acceptor Doped and Undoped Layered La_2NiO_4. (2006) 23-27.

[69] Kharton, V.V. Tsipis, E.V., Yaremchenko, A.A., and Naumovich, E.N. Oxygen permeability, electronic conductivity and stability of $La_{0.3}Sr_{0.7}CoO_{3-\delta}$ dased perovskite. *Materials Science and Engineering* B134(2006) 80-88

[70] Li, F., and Li, J.F. Effect of Ni substitution on electrical and thermoelectric properties of $LaCoO_3$ ceramics. *Ceramics International* 37(2011) 105-110.

[71] Lou, L., Zhong, H., and Yang, X. Oxidative performance and surface properties of Co-containing mixed oxides having the K_2NiF_4 structure. *J. Serb. Chem. Soc.* 69(2004) 783-790.

[72] Li, S., Jin, W., Huang, P., and Shi, J. Comparison of Oxygen Permeability and Stability of Perovskite Type $La_{0.2}A_{0.8}Co_{0.2}Fe_{0.8}O_{3-\delta}$ (A = Sr, Ba, Ca) Membranes. *Ind. Eng. Chem. Res.* 38(1999) 2962-2972.

[73] Ruck, K., Krabbes, G., and Vogel, I. Structure and electrical properties of $La_{2-x}Ca_xNiO_{4+\delta}$ ($0 \leq x \leq 0.4$) with regard to the oxygen content δ. *Materials Research Bulletin* 34(1999) 1689-1697.

[74] Xu, Q., Huang, D.P., Chen, W., and Wang, B.T. Structure, electrical properties and thermal expansion properties of $Ln_{0.6}Sr_{0.4}Co_{0.2}Fe_{0.8}O_3$ (Ln = La, Pr, Nd, Sm) perovskite-type complex oxide. *Journal of Alloys and Compounds* 429(2007) 34-39.

[75] Munnings, C.N., Skinner, S.J., Amow, G., and Davidson, I.J. Oxygen transport in the $La_2Ni_{1-x}Co_xO_{4+\delta}$ system. *Solid State Ionic* 176(2005) 1895-1901.

[76] Ishihara, T., Miyoshi, S., Furuno, T., Sanguanruang, O., and Matsumoto, H. Mixed conductivity and oxygen permeability of doped Pr_2NiO_4-based oxide. *Solid State Ionics* 177(2006) 3087-3091.

[77] Wei, B., Lu, Z., Huang, X., and Su, W. Crystal structure, thermal expansion and electrical conductivity of perovskite oxide $Ba_{1-x}Sr_{1-x}Co_{0.8}Fe_{0.2}O_{3-\delta}$ ($0.3 \leq x \leq 0.7$). *Journal of the European Society* 26(2006) 2827-2833.

[78] Ruck, K., Krabbes, G., and Vogel, I. Structure and electrical properties of $La_{2-x}Ca_xNiO_{4+\delta}$ ($0 \leq x \leq 0.4$) with regard to the oxygen content. *Materials Research Bulletin* 34(1999) 1689-1697.

[79] Shogo, M., Teturo, F., Oravan, S., and Tatsumi, I. Mixed conductivity and oxygen permeability of doped $Pr_2NiO_{4+\delta}$ based oxides. *Journal of The Electrochemical Society* 154(1)(2007) B57-B62.

[80] Rahmouni, H., Jemai, R., and Khirouni, K. Titanium effect on the transport properties in $La_{0.7}Sr_{0.3}Mn_{1-x}Ti_xO_{3-\delta}$. *Journal of Alloy and Compounds* 497(2010) 1-5.

[81] Kaus, I., Wiik, K., and Aasland, S. Oxygen transport properties in $La_{1-x}Sr_xFe_{1-x}M_xO_{3-\delta}$ (M = Cr, Ti), $0.2 < x < 0.8$, $0.2 < y_{Ti} < 0.5$, $0.1 < y_{Cr} < 0.3$. *Solid State Ionics* 178(2007) 817-826.

[82] Rial, C., Moran, E., and Andersen, N.H. Effect of extra oxygen on the structure and superconductivity of $La_{2-}xCa_xCuO_{4+\delta}$ prepared by chemical oxidation. *Physica C* 297(1998) 277-293.

APPENDICES

APPENDIX A

Tolerance number

Goldschmidt (1926) defined the tolerance limits of the size of ions through a tolerance factor, t as Equation (A.1)

$$t = \frac{(r_A + r_O)}{\sqrt{2}(r_B + r_O)} \quad \text{(A.1)}$$

where r_A, r_B, and r_O are the radii of respective ions. For the substituted perovskite at A and B site, $A_{1-x}A'_xB_{1-y}B'_yO_{3-\delta}$, r_A and r_B were calcuated from the sum of each metal at A site and B site, respectively, time its compostition. The atomic weight, ionic charge, coordination number, and ionic radius of all concerned metals were shown in Table A.1

Table A.1 Ionic charge and ionic radius of concerned metals.

Element	Charge	Ionic radius(Aº)
La	3+	1.17
Ca	2+	1.14
Ni	2+	0.69
Ni	3+	0.64
Ni	4+	0.58
Co	2+	0.75
Co	3+	0.67
Co	4+	0.54
Ga	3+	0.68
Ti	3+	0.81
Ti	4+	0.75
O	2-	1.40

APPENDIX B

Activation Energy (E_a)

Arrhenius plot of LSFNi 4682 is given in Figure B-1. The linear part can be described by the small polaron conduction mechanism, following the formula:

$$\sigma = (A/T)\, e^{(-Ea/RT)}$$

$$\ln(\sigma T) = \ln A\, e^{(-Ea/RT)}$$

$$\ln(\sigma T) = \ln e^{(-Ea/RT)} + \ln A \qquad \text{(B.1)}$$

$$\ln(\sigma T) = (-E_a/R)\,(1000/T) + \ln A$$

y **slope** **x** **intercept y axis**

$$-E_a/K = \text{Slope of the linear}$$

$$E_a = -\text{Slope} \times K$$

A is material constant including the carrier concentration term,

σ = The specific conductivity (S/cm)

E_a = The activation energy (kJ/mol)

T = Temperature (K)

R = The gas constant = 8.314472 J/K.mol

From Equation B.1 Arrhenius plot of ln σT versus 1000/*T* gives a straight line, whose slope and intercept can be used to determine E_a and *A*.

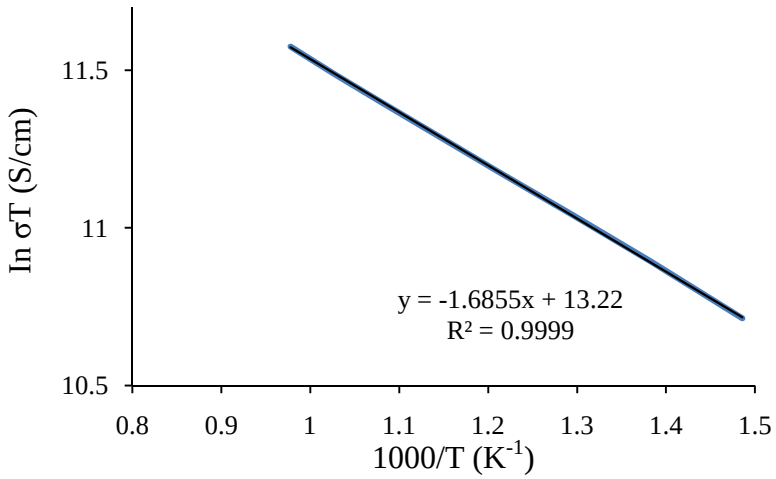

Figure B.1 Arrhenius plot of the electrical conductivity of $La_{1.5}Ca_{0.5}Ni_{0.9}Co_{0.1}O_{4+\delta}$

The activation energy calculated from the slope of the straight line of figure B.1 For example, the activation energy (*E*a) of $La_{1.5}Ca_{0.5}Ni_{0.9}Co_{0.1}O_{4+\delta}$, was calculated as below:

$$y = -1.6855x + 13.22$$

$$\text{Slope} = -1.6855 = -E_a/R$$

Then, $$E_a = -(-1.6855) \times 8.314472 = 14.02 \text{ kJ/mol}$$

VITAE

Miss Chaninart Ratchaoun was born on September 07, 1984 in Chiang Mai, Thailand. She graduated with Bachelor's Degree in Chemistry from Faculty of Science, Maejo University in 2007. Since then, she attended the Master's Degree, Program of Petrochemistry and Polymer Science, Faculty of Science, Chulalongkorn University in 2008 and completed in 2010.

Presentation

26-27 August 2010

Poster presentation "Synthesis and Characterization of Co-doped $La_2NiO_{4+\delta}$ for oxygen permeation" The 2rd International Conference for a Sustainable Greater Mekong Subregion in The Imperial Queen's Park Hotel, Bangkok, Thailand.

Her present address is 29/1 T. Papong A. Doi Saket, Chiang Mai, Thailand, 50220. Tel 085-7053526, E-mail: bamboo45@hotmail.com.